A Universal Wall-Modeling Approach for Large-Eddy Simulations of Complex Turbulent Flows with Heat Transfer

Vom Fachbereich Maschinenbau
an der Technischen Universität Darmstadt
zur
Erlangung des Grades eines Doktor-Ingenieurs (Dr.-Ing.)
genehmigte

Dissertation

vorgelegt von

Yongxiang Li, M.Sc.

aus Poyang Jiangxi, China

Berichterstatter:	Prof. Dr. rer. nat. Andreas Dreizler
Mitberichterstatter:	Prof. Dr. rer. nat. Amsini Sadiki
Mitberichterstatter:	Prof. Dr.-Ing. Suad Jakirlić
Tag der Einreichung:	21.06.2022
Tag der mündlichen Prüfung:	09.09.2022

Darmstadt 2022
D17

Li, Yongxiang: A Universal Wall-Modeling Approach for Large-Eddy Simulations of Complex Turbulent Flows with Heat Transfer
Darmstadt, Technische Universität Darmstadt,
Jahr der Veröffentlichung der Dissertation auf TUprints: 2023
URN: urn:nbn:de:tuda-tuprints-241796
Tag der mündlichen Prüfung: 09.09.2022

Erklärung

Hiermit erkläre ich, dass ich die vorliegende Arbeit, abgesehen von den in ihr ausdrücklich genannten Hilfen, selbstständig verfasst habe.

20.06.2022, 

Datum, Unterschrift

Acknowledgements

This PhD thesis was carried out during my work as a doctoral candidate at the Institute of Energy and Power Plant Technology (EKT), and later at the Institute of Reactive Flows and Diagnostics (RSM) at the Technical University of Darmstadt.

First and foremost, I would like to express my sincere gratitude to Prof. Dr.-Ing. Johannes Janicka, the head of the Institute EKT, and Prof. Dr. rer. nat. Andreas Dreizler, the head of the Institute RSM, for providing me with the opportunity to carry out and complete this PhD project under optimal working conditions. I am also deeply grateful to my supervisor Prof. Dr. rer. nat. Amsini Sadiki, the head of the research group on Modeling and Simulation of Technical Energy Systems at the Institute RSM, for his consistent and excellent guidance, positive outlook on my work, and unwavering support throughout this journey. Additionally, I would like to extend my heartfelt thanks to Prof. Dr.-Ing. Suad Jakirlić for his interest in my thesis and for accepting the role of the external reviewer.

I would like to thank all my friends and colleagues at the Institute EKT, RSM, and STFS, like Pedro Obando, Senda Agrebi, Luis Dressler, Hendrik Nicolai, Dennis Kütermeier, Wibke Leudesdorff, Tao Li, Yaquan Sun, and many others, for their cooperation and companionship, which have been invaluable in completing this work. In particular, I would like to thank Florian Ries and Kaushal Nishad for their friendship, meaningful discussions, suggestions, and the tremendous assistance they provided during this time.

Furthermore, I would like to thank my Bachelor and Master students Theo Gruner, Jan Hamacher, Peng Li, and Luis Felipe Rico Cortes for their time spent here and the significant scientific contributions they made, which greatly influenced this work.

A special thank you goes to my family, especially my dear wife Yongfang. This work would not have been possible without her patience, dedication, motivation, and understanding. I am sincerely grateful to Yongfang for her love and unwavering support during this time. I would also like to express my heartfelt appreciation for the presence of my lovely daughter Qingyou, whose adorable smile and daily activities brought a new level of happiness to my life.

Darmstadt, Juni 2022
Yongxiang Li

To Yongfang and Qingyou

Abstract

Since last few decades, the Large-Eddy Simulation (LES) technique has been widely adapted from academic research to industrial practice with anticipation of LES to be accurate and reliable to predict the unsteady turbulent heat and fluid flows. However, in LES, fine numerical grids scaled by viscous length are indispensable to resolve the turbulent motions in the near-wall dominant flows, which makes LES of wall bounded flow very computational expensive and time-consuming. This shortcoming has limited and impeded the application of LES to realistic industrial flows with solid walls. To circumvent this problem, a widely applied method is to model the flow in the near-wall region, which is expected to provide the essential quantities accurately, e.g. the turbulent quantities in the outer layer, the frictional velocity and the heat flux in an energy system, with significantly reduced computational costs. Despite numerous available wall modeled LES (WMLES) approaches, they are rarely capable to predict the complex heat and fluid flows in a realistic industrial flow application, which is characterized as highly unsteady non-equilibrium wall bounded turbulent flow.

The present work focuses on the development of a reliable and efficient universal wall-stress model for LES that allows to predict unsteady non-equilibrium wall bounded turbulent flows with conjugate heat transfer in industrial flow applications. It is progressively accomplished in four major steps: (1) the development of novel non-equilibrium wall functions for velocity and temperature in the context of turbulent and heated fluid flow; (2) implementation of the novel non-equilibrium wall functions into the framework of OpenFOAM by also taking into consideration of the conjugate heat transfer problem in the context of incompressible heat and fluid flow with constant and variable physical properties for LES; (3) verification and validation of the proposed WFLES approach by means of several generic benchmark test cases relevant to exhaust gas after-treatment systems. Thereby, the reference data-sets are complemented by in-house generated near-wall resolved LES, DNS data and experimental measurement; (4) application of the proposed WFLES to investigate the heat and fluid flow processes in an exhaust gas after-treatment system of a LADA Niva 21214 vehicle under typical driving condition. Thereby, the computed heat and fluid flow phenomena are compared with in-house experimental data.

Important milestones are achieved in this work. In particular, a novel wall functions based wall-modeled LES method is developed as a numerical tool to predict complex turbulent flows with conjugate heat transfer in industrial flow applications. Which is first validated and verified using several typical industrial application relevant generic benchmark test cases, and then applied to predict the turbulent flow with conjugate heat transfer in an exhaust gas after-treatment system under a typical driving operating condition. The accuracy of the developed numerical tool is testified by the good agreement between numerical results and experimental measurement.

This work demonstrates that the proposed wall functions based wall-modeled LES approach is a reliable and flexible numerical tool to predict accurately and economically the complex turbulent flows with conjugate heat transfer in realistic industrial flow applications.

Kurzfassung

In den letzten Jahrzehnten wurde die Grobstruktursimulation (LES) weitestgehend von der akademischen Forschung hin zur industriellen Anwendung adaptiert mit der Erwartung an die LES eine akkurate und zuverlässige Vorhersagen von turbulenten Strömungen mit Wärmetransport zu ermöglichen. Es hat sich jedoch herausgestellt, dass bei der LES feine numerische Gitter, welche mit den viskosen Längenskalen skalieren, für die Auflösung der wandnahen turbulenten Bewegungen erforderlich sind. Das hat zur Folge dass LES von wandnahen Strömungen sehr rechenintensiv und zeitaufwendig sind. Diese Schwächen beschränken und behindern die Anwendung von LES für realistische industrielle Strömungen mit festen Wänden. Eine weitverbreitetet Methode dieses Problem zu umgehen besteht darin, die wandnahe Strömung zu modellieren, was voraussetzt dass die wesentlichen Größen akkurat und mit stark reduzierten Rechenkosten wiedergegeben werden können, wie beispielsweise turbulente Größen in der äußeren Strömungsschicht, Reibwiderstand, und Wärmefluss in einem Energiesystem. Trotz zahlreich verfügbarer Wandmodellierungen für LES (WMLES) sind diese kaum in der Lage komplexe Strömungen mit Wärmetransport in industriellen Strömungsanwendungen, welche durch hoch instationäre, wandnahe Nichtgleichgewichtsströmungen charakterisiert sind, vorherzusagen.

Der Fokus der vorliegenden Arbeit liegt auf der Entwicklung von verlässlichen und universellen Wandfunktionen für LES (WFLES), die Vorhersagen von instationären, wandnahen turbulenten Nichtgleichgewichtsströmungen mit Wärmeübergang in realistischen industriellen Strömungsanwendungen erlauben. Dies beinhaltet: (1) die Entwicklung von neuen Nichtgleichgewichtswandfunktionen für die Geschwindigkeit und Temperatur im Kontext von turbulenten Strömungen mit Wärmetransport; (2) Implementierung der neuen Nichtgleichgewichtswandfunktionen in den Strömungslöser OpenFOAM zur Anwendung von Wärmeübergangsproblemen mittles LES von inkompressiblen Fluidströmungen mit konstanten und variablen physikalischen Eigenschaften; (3) Verifikation und Validierung der vorgeschlagenen WFLES mit Hilfe von mehreren generischen Vergleichtests mit Relevanz für Abgassysteme. Hierbei wurden die Vergleichsdatensätze mit eigenen wandaufgelösten LES, DNS und experimentellen Messungen vervollständigt; (4) Anwendung des vorgeschlagenen WFLES zur Untersuchung von Wärme- und Strömungsprozesse in einem Abgassystem eines Lada Niva 21214 unter realistischen Betriebsbedingungen. Hierbei wurden die berechneten Wärme- und Strömungsphänomene mit eigens erhobenen experimentellen Daten verglichen.

In der vorliegenden Arbeit wurden wesentliche Meilensteine erreicht. Besonders hervorzuheben ist hierbei die Entwicklung eines numerischen Werkzeugs zur Vorhersage von komplexen turbulenten Strömungen mit Wärmeübergang für industrielle Strömungsanwendungen, welches auf einer neuartigen Wandmodellierung für LES mittels Wandfunktionen basiert. Dieses wurde zunächst anhand von mehreren generischen Vergleichsfällen, welche relevant für typische industrielle Anwendung sind, validiert und verifiziert. Anschließend wurde das numerische Werkzeug dazu verwendet um die turbulente Strömung mit Wärmeübergang in einem realistischen Abgassystem unter typischen Fahrtbedingungen vorherzusagen. Die Vorhersagegenauigkeit des entwickelten numerischen Werkzeugs wurde mittels guter Übereinstimmung von Simulation und Experiment bestätigt.

Aus der vorliegenden Arbeit geht klar hervor, dass die vorgeschlagene Wandmodellierung für LES basierend auf Wandfunktionen ein umsetzbares und flexibles numerisches Werkzeug zur akkuraten und wirtschaftlichen Vorherage von komplexen turbulenten Strömungen mit Wärmeübergang für realistischen industriellen Strömungsanwendungen darstellt.

List of Publications

The content of this thesis is partly based on the following journal and conference publications which have been published during the PhD project.

Journal Publications

[**E1**] Ries, F., Li, Y., Rißmann, M., Klingenberg, D., Nishad, K., Böhm, B., Dreizler, A., Janicka, J., Sadiki, A. Database of Near-Wall Turbulent Flow Properties of a Jet Impinging on a Solid Surface under Different Inclination Angles. Fluids, 3(5), **2018**, DOI: 10.3390/fluids3010005

[**E2**] Ries, F., Li, Y., Klingenberg, D., Nishad, K., Janicka, J., Sadiki, A. Near-wall thermal processes in an inclined impinging jet: analysis of heat transport and entropy generation mechanisms. Energies, 6(11), **2018**, DOI: 10.3390/en11061354

[**E3**] Nishad, K., Ries, F., Li, Y., Sadiki, A. Numerical investigation of flow through a valve during charge intake in a DISI -engine using large eddy simulation. Energies, 12(12) **2019**,DOI: 10.3390/en12132620

[**E4**] Ries, F., Li, Y., Nishad, K., Janicka, J., Sadiki, A. Entropy generation analysis and thermodynamic optimization of jet impingement cooling using Large Eddy Simulation. Entropy, 2(21), **2019**, DOI: 10.3390/e21020129

[**E5**] Haussmann, M., Ries, F., Jeppener-Haltenhoff, J. B., Li, Y., Schmidt, M., Welch, C., Illmann, L., Böhm, B., Nirschl, H., Krause, M.J., Sadiki, A. Evaluation of a near-wall-modeled large eddy lattice boltzmann method for the analysis of complex flows relevant to IC engines Computation, 2(8), **2020**, DOI: 10.3390/COMPUTATION8020043

[**E6**] Ries, F., Kütemeier, D., Li, Y., Nishad, K., Sadiki, A. Effect Chain Analysis of Supercritical Fuel Disintegration Processes Using an LES-based Entropy Generation Analysis Combust. Sci. Technol., 11(192), **2020**, DOI: 10.1080/00102202.2020.1770239

[**E7**] Ries, F., Li, Y., Nishad, K., Dressler, L., Ziefuss, M., Mehdizadeh, A., Hasse, C., Sadiki, A. A Wall-Adapted Anisotropic Heat Flux Model for Large Eddy Simulations of Complex Turbulent Thermal Flows Flow, Turbul. Combust.,2(106), **2021**,DOI: 10.1007/s10494-020-00201-6

[**E8**] Li, Y., Ries, F., Leudesdorff, W., Nishad, K., Pati, A., Hasse, C., Janicka, J., Jakirlić, S., Sadiki, A. Non-equilibrium wall functions for large Eddy simulations of complex turbulent flows and heat transfer. Int J Heat Fluid Flow, 88, **2021**, DOI: 10.1016/j.ijheatfluidflow.2020.108758

[**E9**] Li, Y., Ries, F., Nishad, K., Sadiki, A. Predictions of conjugate heat transfer in turbulent channel flow using advanced wall-modeled large eddy simulation techniques Entropy, 6(23), **2021**, DOI: 10.3390/e23060725

[**E10**] Li, Y., Rico Cortes, L.F., Hamel, H., Nishad, K., Biondo, L., Ries, F. Prediction of Heat Transfer and Fluid Flow Effects on Entropy Generation in a Monolithic Catalytic Converter Using Large-Eddy Simulation. Entropy 24, 602, **2022**, DOI:10.3390/e24050602

Conference Publications

[**E11**] Ries, F., Li, Y., Sadiki, A. Entropy production in near-wall turbulent flow inside a generic air-to-air plate heat exchanger. 6th European Conference on Computational Mechanics ECCM6, Glasgow UK, **2018**

[**E12**] Y. Li, F. Ries, K. Nishad, A. Sadiki. Near-wall modeling of LES for non-equilibrium turbulent flows in an inclined impinging jet with moderate Re-number. 6th European Conference on Computational Mechanics ECCM6, Glasgow UK, **2018**

[**E13**] Y. Li, F. Ries, K. Nishad, A. Sadiki. Impact of Atomization Process on the Morphology of a Gasoline Direct Injection Jet (ECN Spray G2) using Large Eddy Simulation including In-Nozzle Flow and Phase Change. ILASS-Asia 2020, Zhenjiang, China, **2020**

[**E14**] Y. Li, F. Ries, K. Nishad, A. Sadiki. Application of large eddy simulation technique to derive correlations of Nusselt numbers for designing exhaust gas systems, The 13th International ERCOFTAC symposium on engineering, turbulence, modelling and measurements, Greece, **2021**

[**E15**] Y. Sun, K. Nishad, Y. Li, L. Dreßler, A. Sadiki. Investigation of Spray in Cross-flow using Automatic Coupled Volume of Fluid and Lagrangian Particle Tracking within Large Eddy Simulation Framework. ILASS-Asia 2022, Madhya Pradesh, Indien, **2022**

List of Master and Bachelor Theses

The following master and bachelor theses were supervised during the PhD project.

Gruner, Theo. Mechanische Energieuntersuchung einer turbulenten, geneigten Aufprallströmung mittels Grobstruktursimulationen, Bachelor Thesis, Technische Universität Darmstadt, **2018**

Hamacher, Jan. A large-eddy simulation based analysis of hot-turbulent flow in an IC-engine exhaust manifold, Master Thesis, Technische Universität Darmstadt, **2019**

Li, Peng. Analysis and modeling of ballistic behavior of pyrotechnical initiators and their impact in airbag inflators applications, Master Thesis, Technische Universität Darmstadt, **2019**

Contents

List of Figures

List of Tables

Nomenclature

Upper case Latin letters		**Units**
$\dot{Q}$	heat power	W
$\mathbf{S}_{ij}^{d}$	traceless symmetric part of the square of the velocity gradient	s^{-2}
$\mathcal{L}$	Characteristic length scale	m
$\mathcal{R}$	Ideal gas constant	J/(mol K)
$\mathcal{U}$	Characteristic velocity	m/s
C_f	skin friction coefficient	–
C_K	Kolmogorov constant	–
C_s	Smagorinsky coefficient	–
C_{OC}	Obukhov-Corrsin constant	–
D_{ij}	rate of deformation tensor	s^{-1}
Gr	Grashof number	–
L	Characteristic length scale	m
Ma	Mach number	–
P	modified pressure	Pa
Pr	Prandtl number	–
Pr_{sgs}	subgrid-scale turbulent Prandtl number	–
Ra	Rayleigh number	–
Re	Reynolds number	–
S	Area	m^2
S_t	Stanton number	–
S_{ij}	Rate of strain	1/s
T	Temperature	K
T^s	solid temperature	K
T_τ	friction temperature	K
U	Characteristic velocity scale	m/s
U	Velocity	m/s
U^+	dimensionless velocity in wall unit	–
U_b	bulk velocity	m/s
V	Volume	m^3
CA	Crank Angle	◦
P	resistance function	–
U_i	Velocity	m/s

Lower case Latin letters		**Units**
τ_w	wall shear stress	Pa
c_p	specific heat	J/kgK
f	frequency	Hz

k	turbulent kinetic energy	m^2/s^2
l_v	valve lift	
l_{mpl}	mean free path length	m
lam	laminar quantities	
p	pressure	m^2/s^2
p_d	mechanical pressure	Pa
q_i	heat flux vector	W/m^2
q_w	wall heat flux	K/m^2
sgs	subgrid scale	
t	time	s
tur	turbulent quantities	
u_τ	friction velocity	m/s
y^+	dimensionless wall distance in wall unit	–

Upper case Greek letters		**Units**
ΔP	pressure drop	Pa
Δt	time-step size	s
$\Delta x, \Delta y, \Delta z$	grid size	m
Φ	physical quantity	–
Π	the rate of production	–

Lower case Greek letters		**Units**
α	thermal diffusivity	m^2/s
α_{sgs}	subgrid-scale thermal diffusivity	m^2/s
δ	channel half height	m
δ_Θ	thermal boundary layer	m
δ_{ij}	konica δ	–
η_K	Kolmogorov length scale	m
η_{OC}	Obukhov-Corrsin length scale	m
γ	blending factor	–
κ	von Kármán constant	–
κ	wave number	m^{-1}
κ_c	cut-off wave number	m^{-1}
λ	thermal conductivity	W/mK
μ	dynamic viscosity	Ns/m^2
ν	molecular viscosity	Ns/m^2
ν_{sgs}	subgrid-scale viscosity	Ns/m^2
ω	phase frequency	rad
ψ	specific value of extensive quantity	–
ρ	mass density	kg/m^3
τ	integral time scale	t
τ_0	time scale of large scale motions	s
τ_K	Kolmogorov time scale	s
τ_{ij}	deviatoric part of σ_{ij}	m^2/s^2
τ_{ij}^{sgs}	subfilter stresses	m^2/s^2
τ_w	wall shear stress	m^2/s^2
θ	temperature variance	K^2
θ^+	dimensionless temperature in wall unit	–

φ	flux per unit area through boundary	–

Abbreviations

BD	Blended Differencing
BEV	Battery Electric Vehicle
CA	Crank Angle
CD	Central Differencing
CFD	Computational Fluid Dynamics
CFL	Courant-Friedrichs-Lewy
CHT	Conjugate Heat Transfer
CV	Vontrol Volume
DDES	Delayed Detached-Eddy Simulation
DES	Detached-Eddy Simulation
DNS	Direct Numerical Simulation
EGAS	Exhaust gas after-treatmeat system
FEM	Finite Element Method
FVM	Finite Volume Method
ICE	Internal Combustion Engine
IDDES	Imporved Delayed Detached-Eddy Simulation
Kn	Knudsen
LBM	Lattice Boltzmann Method
LES	Large-Eddy Simulation
LLM	log-layer mismatch
NASA	National Aeronautics and Space Administration
OpenFOAM	OPEN source Field Operation And Manipulation
PDE	Partial Differential Equation
PISO	Pressure-Implicit with Splitting of Operators
Pr	Prandt
RANS	Reynolds-Averaged Navier-Stokes
Re	Reynold
RMS	Root Mean Square
SCR	Selective Catalytic Reduction
SIMPLE	Semi-Implicit Method for Pressure Linked Equations
UD	Upwind Differencing
VANS	Volume-Averaged Navier-Stokes
VLES	Very Large-Eddy Simulation
WALE	Wall-Adapting Linear Eddy-viscosity
WFLES	Wall Modeled Large-Eddy Simulation with Wall Function
WMLES	Wall Modeled Large-Eddy Simulation
WRLES	Wall Resolved Large-Eddy Simulation

Chapter 1

Introduction

For many engineering applications, such as cooling of turbine blades, fuel combustion in internal combustion engines (ICE) or coupled thermal and fluid flow dynamics inside exhaust gas after-treatment systems (EGAS), an accurate prediction of turbulent fluid flow with heat transfer is of profound importance in order to perform process control and design optimization task. In spite of decades of research, it is still not possible to predict the evolution of turbulent flows with heat transfer analytically. Instead, engineers and researchers employ usually numerical simulations that allow to produce approximate solutions of the turbulent flow with heat transfer at some pre-determined locations in space and time. This method is known as Computational Fluid Dynamics (CFD).

With regard to the CFD investigation of turbulent flows, the most accurate numerical approach is the direct numerical simulation (DNS), which is known to be exceedingly time-consuming and computationally expensive, since the entire spectrum of turbulent length and time scales need to be resolved with extremely fine spatial and temporal resolutions. Therefore, DNS is rarely employed to predict turbulent flow with complex geometry or under complex operating condition, which unfortunately are the case in the most engineering applications. In contrast, rather to resolve all turbulent structures spatially and temporally, in the Reynolds-Averaged Navier-Stokes (RANS) equations based approaches the turbulent motions are represented in a time-averaged manner, which leads to fully modeled, time-averaged solutions of the governing equations. Thus, in comparison to DNS, RANS based simulations demand significantly lower computing resources. Thereby, it allows to analyse many realistic engineering flows at high Reynolds number. However, it is a well-known fact that the RANS approach often lacks in accuracy and is not reliable in the case of turbulent flows with large unsteady characters and turbulent flows including complex heat transfer phenomena. Alternatively, since last few decades the Large-Eddy Simulation (LES) technique has gain good popularity to analyse turbulent flows with heat transfer, which allows more accurate predictions of turbulent heat and fluid flows than RANS, while requires significantly less computational effort as compared to DNS.

In LES, the large-scale turbulent motions are resolved spatially and temporally, whereas the influences of the smaller scales are modeled by subgrid scale (SGS) models. Therefore, LES is anticipated to be accurate and reliable. However, as is generally known that LES experiences shortcomings in dealing with near-wall dominated flows, similar to RANS, unless very fine resolutions are employed in the vicinity of walls [137]. This leads to very computationally expensive LES investigations of wall bounded flows and impedes its applicability in realistic industrial flow applications with solid walls. To address this issue, a common practice in CFD is to employ wall models (known as Wall-Modeled LES, WMLES) to model the near-wall region. These models, such as wall functions, help

reduce computational costs significantly, particularly for heat and fluid flows with high Prandtl and Reynolds numbers. As a result, LES-based investigations become feasible for realistic industrial flow applications.

Although significant progresses have been made in the application of WMLES in recent decades, several issues still remain unresolved. These include the development of suitable wall functions for WMLES, assessing the performance of WMLES with wall functions (WFLES) in realistic engineering flow applications, and more. This motivates the present work that deals essentially with formulation of a reliable WFLES. To demonstrate the applicability and reliability of the proposed WFLES approach, a benchmark test case involving the EGAS of a Lada Niva 21214 vehicle is utilized in this thesis. The following sections provide a brief overview of the current state of research in the fields of EGAS, conjugate heat transfer (CHT) problems, and WMLES. Additionally, the research objectives of this work and the outline of the thesis are presented, as well.

1.1 State of research

The current state of research in the area of exhaust gas after-treatment systems and in regarding conjugate heat transfer problems as well as wall-modeled LES are summarized in this section.

Exhaust gas after-treatment systems

Modern automobiles powered by conventional ICEs have to subjugate two major challenges: firstly, to comply the increasingly stringent emission legislation, and secondly, to have the lowest possible carbon footprint by operating in a manner of best fuel efficiency. These challenges are being addressed either by replacing the existing power-train in battery electric vehicles (BEVs) or by operating internal combustion engine vehicles (ICEVs) with the so called carbon neutral fuels, such as: bio-fuels or low carbon fuels like hydrogen, natural gas, liquid petroleum gas and methanol; synthetic fuels, E-fuels, etc. Moreover, the complete replacement of traditional power-trains ICEVs by BEVs is not foreseeable in near future rather multiple power-trains will coexist [209], with more and more focus on usage of carbon neutral fuels on exiting power-trains [9, 39, 112, 193]. Thereby, it is still imperative to enhance the in-cylinder technology, also for new fuels, together with the deployment of advanced EGAS. This way, a definite incentive is associated with the development of advanced EGAS to meet the prescribed existing and future emission norms. With regard to the numerical modeling and design optimization of EGAS, CFD is becoming a popular tool, since it can provide a comprehensive and macroscopic understanding of the coupled thermal and fluid flow dynamics inside the EGAS. Additionally, it has potential to reduce the overall designing cost and product life-cycle. However, development of CFD based numerical models of such a complex system itself is a challenging task, which requires careful consideration of numerical models at individual component level.

Focusing on the heat transfer in EGAS, many studies have been carried out in the context of the CFD. In the work of Konstantinidis et al. [93], the transient heat transfer phenomena in automotive exhaust systems was summarized. A one-dimensional transient model was developed to compute the transient temperature response of the full exhaust system, and was validated using experimental data. Subsequently, this model was applied by Kandylas et al. in [79] to optimize exhaust systems. Shayler et al. [161] treated the catalytic converter as elemental slices in series, and developed a one-dimensional model for designing and optimizing EGAS under quasi-steady and transient conditions. Various

one-dimensional models were proposed for different applications. For instance, Kapparos et al. [80] carried out sensitivity analysis of a one-dimensional model in an automotive diesel exhaust system. Fu et al. [55] analyzed the convective heat transfer under steady-state and transient conditions using a one-dimensional model under various operating conditions, e.g. inlet mass flow rate and temperature, the pipe geometry as well as flow regime.

One-dimensional models, as mentioned above, are proven to be capable of characterizing heat transfer in a spatially averaged sense, with very low computational cost. However, they are complemented by more accurate three-dimensional studies, which can accurately represent the influence of turbulent flow on heat transfer. Fortunato et al. [54] investigated the thermal behavior in the exhaust system of an automobile with diesel engine, in which the temperature at different positions were measured and used to validate and calibrate the one-dimensional simulation of the EGAS and the three-dimensional simulation of the car underbody. It is worth mentioning that in this study the heat transfer inside EGAS was investigated with one-dimensional model. Similar studies under steady and pulsating conditions were carried out by the group of Xiao [196, 197]. Besides that, Durat et al. [48] found an optimal position of a close-coupled catalytic converter though experimental studies and three-dimensional simulations of the turbulent heat and fluid flow in an EGAS of a spark-ignition engine. In the work of [51], the exhaust gas was measured under different operating conditions, and three-dimensional simulations were carried out using a RANS model.

Apart from focusing on the complete EGAS, the functional components of the EGAS have been investigated separately and deeply in many other studies, as well. For example, the catalytic converter that is a crucial part of an EGAS, in which the harmful species in the exhaust gas are converted or reduced into less-toxic pollutants. In general, as pointed out by Deutschmann et al. in [41], modern catalytic converters are comprised of ceramic or metal monoliths with honeycomb structures. These monoliths have channel densities ranging from 64 to 124 cells per square centimeter. The catalytic substance is distributed on the surface of these channels in a porous form. Thereby, a large interface between exhaust gas and the catalytic substance is ensured by such a structure and an enhanced chemical reaction can be expected for effective reduction of pollutants. Thereby, such a structure ensures a large interface between the exhaust gas and the catalytic substance, which promotes productive chemical reactions. This design facilitates the effective reduction of pollutants in the exhaust gas. In the past few decades, the catalytic converter has been widely investigated at atomic level to understand the influence of various catalytic substances (i.e. Pt, Pd, Rh, etc) on oxidation and/-or reduction efficiency of EGAS [26, 125], in understanding of the complex and relevant chemical reaction kinetics [22, 190], in analyzing the process parameters on EGAS performance [130] or in designing the waste heat recovery system to utilize the thermal energy of the exhaust gas [96]. Focusing on the monolith of the catalytic converter, many studies have been carried out using Volume-Averaging Navier-Stokes (VANS) methodology together with RANS models, in which the monolith is treated as a continuous porous medium, while the flow is modeled in a time-averaging manner [22, 64, 140]. So that a macroscopic view of the flow in the catalytic converter can be provided with low computational cost and simulation time. However, these RANS approach based studies experience serious drawback while dealing with transient evolution of velocity, pressure and temperature fields with their respective fluctuations. As pointed out recently in the work of Cornejo's group [29], a better understanding of the coupled heat and fluid flow phenomena in the catalytic converter can be achieved only by resolving the heat and fluid flow structures spatially and temporally. The simulations were carried

out with different channel shapes, to study the influences of the channel shapes on the pressure drop across the monolith. Additionally, the influence of upstream turbulence on the pressure drop in the catalytic converter were analyzed, as well, which is based on the LES study of a single monolith channel [28].

Mufflers are integrated into EGAS to reduce the acoustic emission, however, they can also lead to back pressure in the EGAS, which consequently influences the performance of the engine [199] and the component ratios in the exhaust gas [117], which has motivated many researcher to optimize the muffler design. Mohiuddin et al. found in [118] that it is undesirable to decrease the back pressure with quieter EGAS. Wagh et al. [192] optimized a muffler to reduce the overall noise without significant increase in the back pressure using three-dimensional CFD. Lota et al. [110] investigated the back pressure in a muffler under assumption of steady state flow using three-dimensional finite-element method (FEM) based RANS model and compared the numerical results with experimental measurement. Kanai and Katsuyama [78] developed a LES based method to predict the flow-induced noise in the muffler and in the exhaust pipe. In their work, the smallest grid size was several ten times greater than Kolmogorov length scale and the solution procedure was optimized for stationary flow to reduce the computational costs.

Studies of other functional components in EGAS were also carried out with three-dimensional numerical simulations and experimental measurements, and reported in the literature, for instance, Meda et al. [114] proposed a FEM based approach for the development of manifolds in EGAS. More recently, various numerical studies of the selective catalytic reduction (SCR) system were published in the literature, e.g., Zöchbauer et al. [212] simulated the flow in a SCR system using LES and RANS; Zheng et al. [210] investigated the NO and SO_2 oxidation in a SCR system using RANS model. Moreover, many other studies of the spray in the SCR were carried out as well, for instance, the spray and its interaction with the exhaust gas was characterized in [182]. Nishad et al. [127] have analyzed the spray break-up and multi-component evaporation of urea–water-solution jets in a SCR system using LES coupled with liquid Lagrangian tracking method.

In studies of EGAS, three-dimensional numerical predictions are becoming increasingly necessary to obtain an accurate representation of the entire EGAS and to conduct detailed investigations of individual EGAS components. The traditionally applied RANS approaches show their drawbacks in dealing with transient evolution of velocity, pressure, species and temperature and their fluctuations. Thus prompting more and more applications of LES based numerical investigations to analyze the EGAS related configurations. However, even the global total available computational power is increasing exponentially, LES is rarely applied to analyze the fluid and thermal dynamics in EGAS. In particular, due to the lack of an appropriate LES approach, which is able to predict the turbulent heat and fluid flow in EGAS accurately and economically. Moreover, to achieve a comprehensive understanding of an EGAS, it is essential to investigate the coupled heat transfer phenomena between the solid and fluid regions, which constitute a CHT problem.

Conjugate heat transfer problem

In many energy systems, such as ICEs, gas turbines, heat ex-changers, catalytic converter monolith channels in after-treatment devices, conjugate heat transfer features a thermal energy transfer process that involves the interaction of conduction within a solid body and convection from the solid surface by fluid motion [42]. The fluid motions and thermal dynamics in the fluid region are governed by the Navier-Stokes equations, while the heat transfer in the solid region is described by the classic heat equation. Such a problem that

consists of two or more sub-domains with phenomena ruled by different sets of differential equations and for which the solution procedure is conjugated among the sub–domains, represents a typical conjugate heat transfer (CHT) problem [42].

The CHT problem has been studied since the time of Newton [42]. At that time this problem was solely analyzed by means of experiment to evaluate the heat transfer coefficient. Nowadays, thanks to the rapid ongoing growth in mathematics and computational science in the last few decades, it is now possible to solve the equations describing the CHT problem analytically or numerically. Since the end of 1960s a large number of CHT problems were studied analytically. For instance, at early time the researchers found out analytical expressions to describe the heat transfer in some simple configuration, e.g. in [167] an analytical expression was given for the CHT between a plate and a fluid. Later on, the heat flux on a non-isothermal streamlined body was analyzed, and a general solution was formulated for the one– or two–dimensional steady–state CHT problem. However, this solution is limited to linear problems (see [42]). Applications of this analytical solution are provided in more details in [43, 44, 44, 45, 59]. Moreover, unsteady CHT problems in several specific configurations have been considered and solved analytically as well, e.g. a sudden change of ambient temperature in thermal entrance region of parallel duct [179], parallel plats channels [25,65,177,178,200] and in circular pipes [81,102,109,145,187,201].

Nevertheless, an analytical solution is rarely available for problem with complex geometry or under complex operation conditions, which leads to the alternative solution approach for the CHT problem, namely the numerical method. Instead of finding out an exact solution for the CHT problem, an approximate solution is supplied by numerical simulations. A numerical solution procedure is normally independent on the geometries or operating conditions, thus, almost all CHT problems can be solved by numerical simulations. Since the middle of 1970s, the numerical method has been applied to solve CHT problem, e.g. [24]. Subsequently, a great number of numerical simulations have been carried out for different devices and technological processes. Regarding CHT problems, the researchers focused on different issues, for instance, Demirdzic and Muzaferija [40] developed a numerical method to calculate additionally solid body stresses caused by deformations, Alekseev and Navon [4] estimated the temperature uncertainty of CHT problems. Moreover, the numerical methods have been also applied to analyze the CHT in energy systems, e.g. Sondak and Dorney [168], Kassab et al. [82] and Croce [34] have investigated the CHT in turbo-machinery while using RANS–based approach to model the fluid motions in fluid region. However, RANS approaches have been proven to be less accurate for the prediction of unsteady turbulent flows in such an energy system, in which the heat transfer processes are determined by the unsteady turbulent motions.

A more accurate prediction of the thermal processes in the fluid regions can be achieved by a scale resolved method, e.g., the most accurate numerical method, DNS, in which all turbulent motions are resolved spatially and temporally. As the supercomputer performance growths exponentially in the last decades, DNS has been applied to resolve the turbulent heat and fluid flow in several generic configurations [52,122,151,154,185,186,195]. Despite the accuracy of DNS, the extremely high computational cost limits the application of DNS to a realistic industrial energy system. An alternative method, which is able to predict the unsteady turbulent motions accurately, is the LES technique, which has been proven in many literature to be an accurate approach to predict turbulent fluid flow motions and thermal processes, e.g. [127, 128, 152, 153]. LES were therefore applied to investigate the fluid motions and heat transfer in CHT problems from generic flow configurations, such as flow over a matrix of surface mounted cubes [211] or heated cavity flows [27], to complex industrial applications, e.g., cooling of gas turbine blades [47].

However, in the classic wall–resolved LES (WRLES) technology, it is essential to resolve the thin momentum and thermal boundary layers in the vicinity of the solid surface by numerical grids with very fine spatial resolutions, resulting in high computational effort, in particular, for turbulent heat and fluid flow with high Prandtl (Pr) or Reynolds (Re) numbers. Therefore, to address this issue, it is a common practice in LES to employ a near-wall modeling approach that allows for modeling the fluid and thermal behaviors in the near-wall region with much coarser resolutions, thereby significantly reducing the computing resources required by the simulation. The LES with wall modeling approach is described in detail in the next paragraphs.

Wall-modeled Large-eddy Simulation

In the last few decades, the LES technique has become increasingly attractive for supporting numerical investigations of systems with turbulent heat and fluid flow applications. This increased interest is mainly due to the availability of more powerful computing resources. However, similar to approaches based on RANS equations, it is well-known that LES encounters difficulties in accurately capturing near-wall dominated flows, unless very fine grids are employed to resolve the turbulent motions close to the wall [137], which are characterized by the viscous length scale, $\delta_\nu = \nu/u_\tau$, where ν is the fluid kinematic viscosity and u_τ is the friction velocity. This makes LES of wall-bounded flows computationally very costly and impedes its application for realistic industrial flows with solid walls, for instance, CHT problems. To overcome this challenge, a widely applied alternative method in CFD, known as Wall-Modeled LES (WMLES), is to model the flow in the near-wall region using, e.g., Wall Functions. The WMLES is expected to provides the essential quantities accurately, e.g., the turbulent quantities in the outer layer (away from the wall) and the frictional velocity (at the wall). The former one is obviously indispensable in the WMLES, while, the latter one determines the prediction of some key quantities, such as heat flux, boundary layer separation, drag prediction, etc., is therefore a crucial quantity to be predicted by WMLES. In particular, a WMLES approach must be able to predict the turbulent quantities and the frictional velocity accurately with low computational cost and simulating time. In the case of WMLES, the computational cost is determined by the calculation of outer layer, which is proportional to $Re^{0.6}$, while the one of a classic Wall-resolved LES (WRLES) is proportional to $Re^{2.4}$ [137]. Therefore, the computational cost is reduced significantly with WMLES, especially in the case of turbulent flows with high Re–number or Pr–number.

Numerous near-wall modeling approaches have been reported in the literature, in which turbulent motions in outer layer are resolved by means of LES, whereas turbulent quantities in the inner layer are either modeled by means of RANS or predicted according to the modeled wall-stress [18, 83]. The former one is also known as hybrid RANS–LES model, in which the applied model switches from LES to RANS through changing the length scale, e.g. in the case of Detached-eddy simulation (DES) [173], or merges the subgrid scale (SGS for LES) viscosity with the turbulent eddy viscosity (for RANS) through a blending function, e.g. Very Large-Eddy Simulation (VLES) [20, 95, 173]. In the latter one, the so-called wall-stress modeling, the entire domain is calculated using a LES model, whereas the wall-shear stress τ_w or the friction velocity u_τ is modeled by the employed wall modeling methods, e.g. using wall functions, virtual wall boundary conditions, dynamic slip wall modeling or control-based strategies to approximate wall boundary conditions.

The DES approach, a typical hybrid RANS–LES approach, has been introduced by Spalart et al. [171] originally to simulate massively separated flows. Lately, it has been

applied widely and successfully as a WMLES approach. A log-layer mismatch (LLM) and a related $5\% - 15\%$ error in the prediction of wall-shear stress have been reported in the studies of equilibrium flows like turbulent channel flows using DES approaches (see [12, 86, 126, 138, 183, 184]). As pointed out by Piomelli in [137], the LLM is caused by the disparity of scales between the LES region and RANS region. Thereby, RANS is formulated in a time-averaged way, which is unable to represent high frequent fluctuations, even if near the RANS–LES interface. The absence of a mechanisms, by which the modeled turbulent energy in RANS is transferred into the resolved energy of LES, leads to a enlarged mean velocity quantity near the interface. This implies that the turbulent energy from RANS region is represented by the mean velocity field in the LES region rather than by velocity fluctuations. Regrading the lack of resolved eddies near the RANS–LES interface, several modifications have been introduced to reduce or remove the LLM, e.g. adding artificial fluctuations in the interface region [86] or calculations of the separated flow over a contoured ramp [144]. The most successful DES approaches were suggested by Shur et al. in [164], known as Delayed Detached–eddy simulation (DDES), and Travin et al. in [188], prominent as Improved Delayed Detached–eddy simulation (IDDES). Thereby, a special blending function is employed to reduce significantly the viscosity in the interface region, which enables a reliable prediction of velocity fields without LLM.

In the case of wall-stress modeling, instead of directly resolving the thin momentum boundary layer at the wall, the wall-shear stress is modeled using the quantities from outer layer. This can be achieved through, e.g., the application of wall functions or by adopting a zonal approach. The WMLES with wall functions essentially, denotes WFLES, is an extension of the approach commonly used in RANS simulations with wall functions. It was initially introduced by Deardorff in 1970 for simulating a turbulent channel flow at high $Re-$number [36]. In Deardorff's work, it is assumed that the velocity at the first off-wall cell centre satisfies the logarithmic law. The velocity is determined by solving a time-independent partial differential equation (PDE) estimated based on the logarithmic law. The obtained velocity is applied subsequently as boundary condition for the LES calculation, allowing for the modeling of the near-wall region without explicitly resolving its fine-scale turbulence. Alternative to solve logarithmic law for velocity, wall functions can also be satisfied by calculate u_τ algebraically with known velocity from LES calculation [99]. Thereby, instead of modifying velocity at the first off-wall cell centre, the SGS viscosity at the wall is modified according to friction velocity u_τ or wall-shear-stress τ_w that can be evaluated from the applied wall function and the known velocity at the first off-wall cell centre [60].

WMLES with classic wall functions have been applied successfully to predict the equilibrium turbulent flows like turbulent channel or pipe flows or turbulent boundary layer flows, in which a constant-stress layer exists near the wall. However, WMLES with classic wall functions is not capable to predict the turbulent flow in realistic industrial applications with complex configuration or under complex operating condition. On one side the classic wall function is not available in the buffer layer and thus discontinuous from the wall to logarithmic layer; on the other side, the flow in such an industrial application comply hardly the equilibrium assumption. Regarding the former one, unified expressions of the classic wall function were proposed, e.g. by Spalding in [172], by Musker in [121], etc. Pertaining to the latter one, several wall functions were proposed for generalized wall flows in the last decades. For instance, Shih et al. [163] proposed a pressure gradient based velocity wall function, which calculates the effects of pressure gradient and is imposed to the Spalding wall function. The superimposed wall function is applied to describe a generalized mean wall flow. In the approach proposed by Craft et al. [32, 33], the so called

"analytical wall functions", the near-wall region is divided into a viscous dominated and a fully turbulent part. Thereby, analytical expression is formulated for each part based on a simple prescribed distribution of turbulent viscosity, and non-equilibrium effects like pressure gradients and buoyancy effects are retained in the analytical wall function formulation. Based on this, Suga et al. [180] proposed a two-segment piecewise linear formulation of the SGS eddy viscosity inside the wall–adjacent cell, which allows to use the analytical wall function approach in the framework of LES. A similar approach, the "compound wall treatment", proposed by Popovac and Hanjalic [143], a simpler formulation of the eddy viscosity along with smooth blending functions is adopted to derive analytical expressions for the velocity and temperature that are valid over the whole range of y^+. Additionally, Popovac and Hanjalic in [143] incorporate a correction factor that accounts for local non-equilibrium heat and fluid flow effects. Recently, Dzanic and Oefelein [49] proposed a similar non-equilibrium wall function for the momentum boundary layer by including a forcing term in their formulation that accounts for the effects of convection and pressure gradients. It is worth mentioning that these wall functions can be applied to both LES and RANS. Examples of LES and RANS studies of realistic industrial applications using the wall function approaches can be found in e.g. [5, 8, 49, 98, 202, 208], and elsewhere. Notably, an associated temperature wall function can be easily derived from the velocity wall function by using Reynolds analogy. Nevertheless, limitations are also visible in the reported wall functions, such as discontinuous from wall to logarithmic layer, incapable in dealing with the non-equilibrium flows, lack of transient effects and so on. Regarding this limitations, a novel non-equilibrium wall function formulation, which is applicable to complex turbulent flows with heat transfer, has been proposed by the present author in [104], which is described in detailed in Chapter 3 of this thesis. The LLM was also observed in the simulation with WFLES approaches. However, as pointed out by Larsson et al. in [99], instead of a positive LLM for almost all hybride LES–RANS approaches, the LLM in WFLES can be either positive or negative, depending on the applied code, the numerical setup and the LES itself. A converged results with zero LLM can be accomplished through a grid sensitivity study [84]. Last but not least, in WFLES the inner layer is bridged by a cell with a wall function, no additional PDE or ODE is solved, the computational cost of WFLES is therefore exclusively less than all other WMLES approaches, especially in the case with high Pr–number and Re–number.

An alternative approach to modeling the wall-shear stress involves solving a simplified set of RANS-based turbulent boundary-layer equations. This is done in an auxiliary mesh region that is positioned between the outer mesh and the solid surface within the fluid region. The auxiliary mesh has a fine spatial resolution in the wall-normal direction. In this approach, the RANS-based turbulent boundary-layer equations are specifically tailored to capture the near-wall behavior of the flow variables. By solving these simplified equations in the auxiliary mesh region, the wall-shear stress can be determined without the need for resolving the fine-scale turbulence near the solid surface. Then, the wall-shear stress predicted by RANS simulation employed as a wall boundary condition for the LES calculation on the overlapped outer mesh [106, 137], thus this method is also known as zonal approach or two-layer model. Thereby, pressure gradient and convection effects are considered from the solution of the RANS-based turbulent boundary-layer equations. Consequently, two-layer models are also able to capture to some extent the non-equilibrium effects. Various two-layer models have been reported recently in the literature, e.g. in [84], where Kawai and Larsson analyzed the behavior of turbulence length scales near the wall and improved the mixing length formula for RANS region through modifying the von Kármán constant κ as a function of the wall distance. Whereas, Park and Moin [132]

suggested to adjust the von Kármán constant dynamically. The LLM can be avoided through these ways. Nevertheless, an other challenging, namely the generation of two separate numerical grids, has limited the application of the two-layer model to complex geometries.

1.2 Research objectives

As mentioned in the previous section, LES has shown the capability to accurately predict turbulent fluid flow with heat transfer in complex engineering applications such as EGAS. However, a WRLES could be highly computationally expensive and time-consuming to predict the turbulent heat and fluid flow in such an industrial application with complex geomerty and operating conditions.

Therefore, the main objective of this thesis is to develop a reliable and efficient WFLES based numerical tool for accurately predicting the turbulent flow with heat transfer in realistic industrial applications. For the purpose stated above, the specific objectives of the present work are as follows:

- Develop unified velocity and temperature wall functions for general turbulent heat and fluid flows
- Develop a reliable and efficient WFLES based numerical tool to predict wall-bounded turbulent heat and fluid flows with variable density, and implement this numerical tool into the standard framework of OpenFOAM.
- Verify and validate the implemented numerical methods using various generic EGAS relevant configurations
- Calibrate and validate the developed numerical tool using measured data of an EGAS

In order to demonstrate the applicability and reliability of the proposed WFLES approach, an EGAS of a Lada Niva 21214 vehicle is selected as a benchmark test case.

1.3 Thesis outline

The remaining thesis consists of six chapters, which are organized as follows:

Chapter 2 briefly reviews balance laws of thermo-fluid mechanics, properties of turbulent heat and fluid flow, the theory of thermal and momentum boundary layers and the mathematical description of conjugate heat transfer problems.

In Chapter 3, the focus is on reviewing WRLES and WMLES approaches with different LES models and near-wall treatments. Subsequently, a novel non-equilibrium wall function approach for LES is proposed to predict complex turbulent heat and fluid flow efficiently and accurately.

The discretization procedure, solution procedure, and implementation of the novel wall functions for turbulent flow with conjugated heat transfer within the framework of OpenFOAM are described in Chapter 4.

In Chapter 5, the proposed WFLES approach is evaluated for heat and fluid flow scenarios that are relevant to EGAS or other technical energy systems.

In Chapter 6, the proposed WFLES approach is applied to predict the turbulent flow with conjugate heat transfer in a benchmark test configuration, specifically the EGAS of a Lada Niva 21214 vehicle, under a typical driving condition. The obtained numerical results are then compared with experimental data to assess the accuracy and reliability of the proposed WFLES approach.

In Chapter 7, the major findings of the present work are summarized and an outlook for potential further research is provided.

Chapter 2

Principles of thermo-fluid dynamics

This chapter briefly reviews balance laws of thermo-fluid mechanics, physical properties of turbulent heat and fluid flow, the theory of thermal and momentum boundary layers, and the mathematical formulation of conjugate heat transfer. In the present work, it is assumed that the continuum hypothesis holds true, which means that we operate at length and time scales sufficiently large that the atomistic picture can be averaged out [94]. This leads to a fully continuum picture where measurable quantities such as fluid velocity and density can be described using the macroscopic balance laws of thermo-continuum mechanics. The Knudsen number (Kn) helps to determine whether the continuum hypothesis is valid for modeling a fluid mechanical system or not. It is defined as the ratio between the mean free path length l_{mpl} to a representative physical length scale L [174], reads:

$$\mathrm{Kn} = l_{mpl}/L. \tag{2.1}$$

For $\mathrm{Kn} \ll 1$, the continuum picture is valid, and the macroscopic balance laws of thermo-continuum mechanics can be used to describe the fluid flow system. In the case of $\mathrm{Kn} \gtrsim 1$, a description based on statistical mechanics is capable to model adequately the characteristics of such fluid flow systems. In this work only fluid flow systems with $\mathrm{Kn} \ll 1$ are considered where the continuum hypothesis is always satisfied. Furthermore, for the sake of simplicity, right-handed Cartesian coordinate system is employed throughout the text and the summation convention applies to repeated subscripts. Further information and explanations of the principles of material theory can be found in e.g. [6, 76, 90, 94, 113, 120].

2.1 Balance laws

In the macroscopic description of thermo-fluid systems, any extensive quantity Φ of a system with the volume V can be defined as

$$\Phi = \int_V \psi dV, \tag{2.2}$$

in which yields $\psi = \rho\phi$ with the specific value ϕ and the mass density ρ [76]. The general form of the macroscopic balance equation for the quantity ψ reads as follows: [120]

$$\frac{D}{Dt}\int_V \psi dV = \int_S \varphi_i n_i dS + \int_V Z dV + \int_V \Pi dV. \tag{2.3}$$

Here D/Dt represents the substantial derivative, φ_i the flux per unit area through the boundary S, Z is the supply of ψ and Π denotes the rate of production (>0) or destruction

(<0) per unit volume of Φ. n_i is the unit vector outwards normal to boundary S. The flux φ_i has one order higher tensorial rank than ψ (e.g. φ_i is a vector if ψ is a scalar), while Z and Π have the same tensorial rank as ψ [76]. Eq. 2.3 must be true for any volume element, which leads to the local form of the general balance equation, expressed as [70]

$$\frac{\partial \psi}{\partial t} + \frac{\partial}{\partial x_i}\left(\psi U_i\right) = \frac{\partial \varphi_i}{\partial x_i} + Z + \Pi, \tag{2.4}$$

with the fluid velocity U_i. When discontinuities exist inside the material body (e.g. in the form of a singular surface S^*), a so-called jump condition can be derived, which reads [76]

$$[\![\psi\left(U_i - v_i\right) n_i]\!] - [\![\varphi_i n_i]\!] = 0. \tag{2.5}$$

Here, the brackets $[\![.]\!]$ denote the jump of ψ across the discontinuity and v_i is the speed of the displacement. The fluxes and supply terms in Eq. 2.3 and Eq. 2.4 corresponding to the properties of mass, momentum, internal energy and entropy are summarized in Tab. 2.1. Additionally, the fluxes and supply terms of the heat equation are included in this work, as they are essential for describing the heat transport in the solid domain when dealing with conjugate heat transfer problems.

Table 2.1: Fluxes and supply terms in balance laws of thermo-fluid mechanics. Here, ρ is the mass density, U_i the fluid velocity, e the internal energy, s the entropy density, σ_{ij} the Cauchy stress tensor, q_i the heat flux vector, T the temperature, f_i a body force per unit mass, r a heat source, $L_{ij} = \frac{\partial U_i}{\partial x_j}$ the velocity gradient tensor, p the pressure and τ_{ij} the deviatoric part of σ_{ij}.

	ψ	φ_i	Z	Π
mass	ρ	–	–	–
momentum	ρU_i	σ_{ij}	ρf_i	–
energy	ρe	q_j	ρr	$\sigma_{ij} L_{ij}$
entropy	ρs	q_j/T	–	$\frac{1}{T}\tau_{ij} L_{ij} - \frac{1}{T^2} q_i \frac{\partial T}{\partial x_i}$
heat equation	T	q_j	–	–

The balance laws of thermo-fluid mechanics are general and applicable to any continuous material and flow system [150]. These laws provide a fundamental framework for describing the conservation of mass, momentum, and energy in fluid systems, regardless of the specific characteristics or properties of the system. Therefore, a set of additional constitutive relations are required to characterize the thermo-mechanical behavior of a given material, as well as to close the balance equations. In the case of Navier-Stokes-Fourier fluids, which is employed in the present work, the Cauchy stress tensor σ_{ij} depends solely linearly on the deformation D_{ij}, while the heat flux q_i depends linearly on $\frac{\partial T}{\partial x_i}$. Thus, the constitutive equations for σ_{ij} and q_i can be simplified as

$$\sigma_{ij} = -p\delta_{ij} + 2\mu D_{ij} \tag{2.6}$$

and

$$q_i = -\lambda \frac{\partial T}{\partial x_i}, \tag{2.7}$$

where p is the pressure, λ the thermal conductivity and μ the dynamic viscosity.

In the present work, the kinetic behaviour of the involved gas is described using the ideal gas law. It is written explicitly for pressure in terms of the intensive properties ρ

and T, as follows:

$$p = \frac{\rho R T}{M} \tag{2.8}$$

with the molecular weight M of the evolved gas and the universal gas constant $R = 8.3144598$ J/(molK). Notably, it is assumed that molecules occupy no volume and exert no inter-molecular forces. Furthermore, assuming thermodynamic equilibrium, the caloric equations of state of an ideal gas depend only on T. It follows that

$$e \equiv e|_{eq}^{IG} = f(T), \qquad s \equiv s|_{eq}^{IG} = f(T), \tag{2.9}$$

where $(\cdot)|_{eq}$ denotes equilibrium and $(\cdot)|^{IG}$ ideal gas.

2.2 Turbulent heat and fluid flows

In thermo-fluid dynamics, turbulence is a fluid motion characterized by chaotic changes in temperature and flow velocity. This is in contrast to a laminar flow, which occurs when a fluid flows in parallel layers, with no disruption between those layers [15]. A fluid flow is whether turbulent or not, can be distinguished with help of a dimensionless quantity: the Reynolds number, which measures the relative importance of inertial forces to viscous forces within a fluid flow. It is defined for a flow with the characteristic velocity U and the characteristic length scale L as [7]

$$Re = \frac{\rho U L}{\mu}. \tag{2.10}$$

In general, laminar flow is observed when the Reynolds number is lower than a certain critical Reynolds number (Re_{crit}, e.g. $Re_{crit} = 2300$ for pipe flow with Newtonian fluid), however, if $Re \gg Re_{crit}$ the flow is considered as turbulent.

Many energy systems such as ICEs, EGASs or general cooling/heating applications are characterized by turbulent fluid flow with heat transfer. One example of such a turbulent flow with heat transport is illustrated in Figure 2.1, that shows planar images of the dimensionless magnitude velocity (a) and temperature (b) fields of a turbulent channel flow at a Reynolds number of $Re = 14124$. Thereby, a wide range of length and time scales can be observed and it is obvious that these turbulent motions are unsteady, irregular, seemingly random and chaotic [142].

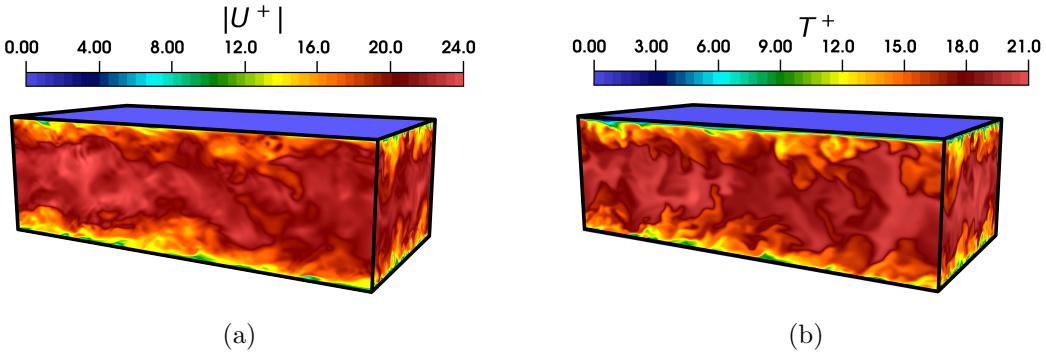

(a) (b)

Figure 2.1: Turbulent channel flow at Reynolds number of $Re = 14124$ ($Re_\tau = 395$). Snapshots of the dimensionless magnitude velocity ($U^+ = |U|/u_\tau$) (a) and temperature ($T^+ = (T_w - T)/T_\tau$) (b) fields.

As implied by the above discussion, turbulent heat and fluid flows are locally quasi-stochastic, inherently three dimensional, unsteady, vortical and dissipative. Thereby, the turbulent flows exhibit a wide distribution of length and time scales which interact with each other. Based on the concept of the energy cascade introduced by Richardson [149], turbulence is considered to be composed of coherent turbulent motions of different size. The generated large scale motions (e.g. by separation) break up and transfer their energy to slightly smaller ones. These large scale motions have dimensions of the order of the flow domain $l_0 = \mathcal{O}(\mathcal{L})$ and their energy predominantly originates from the mean flow. These smaller scales undergo a similar break-up process. Within these break up processes, energy is transferred to successively smaller and smaller scales until the molecular viscosity or thermal diffusivity are effective in dissipating the energy [142], respectively, and no smaller vortices can be further formed. Based on Kolmogorov's similarity theory and his hypothesis of local isotropy [91, 92], the directional tendencies along with all information about the geometry of large scale motions get lost in this chaotic scale-reduction process, leading to universal, homogeneous, isotropic small scales. Important in this context is that energy enters the energy cascade at largest scales, while dissipation takes place at the end of the scale-reduction process.

In the case of turbulent fluid flow, the smallest length, velocity and time scales are of the order of the Kolmogorov scales, which defined as

$$\eta_K \equiv \left(\frac{\nu^3}{\epsilon_k}\right)^{1/4}, \qquad u_K \equiv (\nu\epsilon_k)^{1/4}, \qquad \tau_K \equiv \left(\frac{\nu}{\epsilon_k}\right)^{1/2}, \tag{2.11}$$

that depend only on the dissipation rate of turbulent kinetic energy ϵ_k and the viscosity ν. By assuming a scaling of $\epsilon_k \sim u_0^3/l_0$ it follows that the ratio between these smallest scales and the largest turbulent motions are proportional to the Reynolds number as

$$\frac{\eta_K}{l_0} \sim Re^{-3/4}, \qquad \frac{u_K}{u_0} \sim Re^{-1/4}, \qquad \frac{\tau_k}{\tau_0} \sim Re^{-1/2}, \tag{2.12}$$

which shows that with higher Reynolds numbers, smallest scales become very small compared to largest scales.

Regarding the turbulent temperature field, dimensional analysis yields $\eta_T \propto (\alpha\tau)^{1/2}$ for the smallest length scales, where α is the thermal diffusivity and τ the characteristic time scale, which differs for low and high Prandtl numbers [156]. For $Pr \leq 1$, smallest length scales are dictated by both, thermal diffusivity α and by viscous dissipation. These are the Obukhov-Corrsin length scales [30, 129], given as:

$$\eta_{OC} \equiv \left(\frac{\alpha^3}{\epsilon_k}\right)^{1/4} = Pr^{-3/4}\eta_K, \tag{2.13}$$

with dimensions equal or larger than the Kolmogorov scales. For $Pr > 1$, viscous diffusion overwhelms thermal diffusion and the smallest temperature length scales are referred as Bachelor length scales [16], reads:

$$\eta_B \equiv \left(\frac{\alpha^2\nu}{\epsilon_k}\right)^{1/4} = Pr^{-1/2}\eta_K, \tag{2.14}$$

which are by a factor of $Pr^{-1/2}$ smaller than the Kolmogorov length scales. Obviously, smallest temperature scales are less universal than those of the velocity field and can be significantly smaller for $Pr \gg 1$. How the turbulent kinetic energy and the temperature

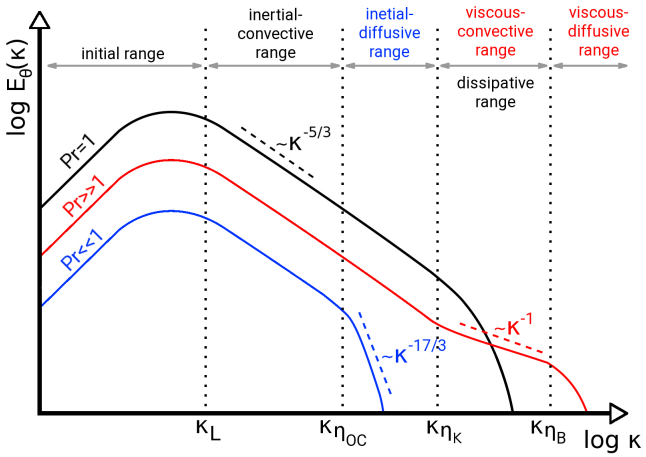

Figure 2.2: Temperature variance spectra of turbulent heat transport for different Prandtl numbers [150]. Notice that the turbulent kinetic energy spectrum equals the temperature variance spectrum for $Pr \equiv 1$.

variance are distributed among these turbulent scales of different sizes is illustrate in Figure 2.2, which shows the wave number spectrum of temperature variance for different Pr numbers [150].

For the case with $Pr \equiv 1$, where the temperature variance spectrum equals the turbulent kinetic energy spectrum, the spectrum can be divided into different characteristic subranges, namely, the *energy-containing*, the *inertial* and the *dissipative range*. Thereby, turbulent kinetic energy is predominantly distributed at large scales that originate from the mean flow. In contrast, at highest wave numbers, diffusive effects are dominant and smallest scales are dissipated into heat. In between, there is the inertial range, where according to Kolmogorov's second similarity hypothesis, the spectra has a universal form. A similar physics can be obtained for the temperature variance spectra for $Pr \leq 1$. In contrast, the energy transfer phenomena becomes more complicated when $Pr \gg 1$. Thereby, heat conduction has no noticeable influence on small scale temperature fluctuations, while velocity scales are damped by viscous dissipation. A second inertial range appears, the so-called *viscous-convective range*, which is located at high wave numbers within the range of $\kappa_{\eta_K} \ll \kappa \ll \kappa_{\eta_B}$. Besides the different shapes of the temperature variance spectra for different Prandtl numbers, small temperature scales are also influenced by the interaction between the velocity gradient and the scalar fluctuations, which leads to anisotropic thermal diffusion even at smallest temperature scales [150].

2.3 Thermal and momentum boundary layers

In thermo-fluid mechanics, a boundary layer is a region of comparatively small thickness in the immediate vicinity of a bounding surface within which the viscous forces are comparable to the inertial forces and within which the relative speed between the body and the fluid decreases rapidly to zero [46]. Boundary layer flows can be divided into thermal and momentum boundary layers, that are either laminar or turbulent. The laminar boundary layer is a very smooth flow, while in turbulent boundary layers the temperature and velocity fields vary significantly and irregularly in both position and time.

Regarding laminar heat and fluid flow conditions, the description of the near-wall boundary layer flow can be derived directly from the Navier-Stokes equation. Prominent

examples are the Stokes boundary layer flow that is created by an oscillating solid surface, the Blasius boundary layer that forms on a semi-infinite plate which is held parallel to a constant unidirectional flow, or the Ekman boundary layer when a fluid rotates and viscous forces are balanced by the Coriolis effect. Further examples of laminar boundary flows including their mathematical description can be found in [158].

The treatment of turbulent boundary layers is far more difficult and cannot be calculated analytically from the Navier-Stokes equations. Therefore, predominantly asymptotic solutions are derived to describe the near-wall thermo-fluid dynamics. In this respect, the most well-known formulation to describe the near wall velocity is the classical wall function proposed by von Kármán [191]. In this velocity wall function, the momentum boundary layer is divided into a viscous and an inertial sublayer. Assuming a simple wall-attached equilibrium flow at sufficiently high Reynolds number, it is possible to derive analytically asymptotic solutions for the mean velocity within both sublayers as [191]

$$u^+ = \begin{cases} y^+ & y^+ \leq 5, \\ \frac{1}{\kappa} \log\left(B y^+\right) & y^+ \geq 30, \end{cases} \tag{2.15}$$

where $u^+ = U/u_\tau$ and $y^+ = y u_\tau / \nu$ are the dimensionless mean velocity and wall distance, respectively, u_τ the friction velocity, ν the kinematic viscosity, $\kappa \approx 0.41$ the von Kármán constant and $B \approx 9.8$ an integration constant. The region between the viscous sublayer and the inertial sublayer ($5 \leq y^+ \leq 30$), where viscous and turbulent stresses are of the same order, is called as buffer layer. No theoretical asymptotic solution can be derived for this transition region and it is therefore not correctly represented by means of the classical wall function. Therefore, in order to address this issue, many researchers employed blending functions [77, 143] or simple models for the turbulent stress in the buffer layer combined with a proper matching procedure [23, 38, 107, 121, 131, 148, 163, 172] to derive "unified" expressions for the mean velocity profile, which are valid over the whole range of dimensionless wall distance y^+.

The thermal equivalent to Eq.2.15 can be derived by assuming the Reynolds analogy between momentum and energy transfer. With this consideration, the classical temperature wall function formulations for the thermal conduction and the inertial sublayers at sufficiently high Reynolds numbers and small molecular Prandtl numbers ($Pr \leq 1$) read [37, 147]

$$T^+ = \begin{cases} Pr\ y^+ & y^+ \leq 5, \\ Pr_t \left(\frac{1}{\kappa} \log\left(B y^+\right) + P \right), & y^+ \geq 30, \end{cases} \tag{2.16}$$

where $T^+ = (T_w - T)/T_\tau$ is the dimensionless temperature, $T_\tau = |q_w| / (\rho c_p u_\tau)$ the friction temperature, T_w the wall temperature, q_w the wall heat flux, ρ the mass density and c_p the specific heat capacity. Pr and Pr_t denote the molecular and turbulent Prandtl numbers, respectively, while P is an additional resistance function that accounts for the influence of different Pr numbers on the near wall temperature profile in the inertial sublayer (various functions for P can be found in e.g. [74, 77, 101, 111]). Similar to the near wall velocity, no theoretical asymptotic solution is known for the transition region ($5 \leq y^+ \leq 30$). Therefore, in analogy to the near wall velocity profile, temperature wall function formulations have been suggested in the literature, e.g. [77, 143, 146, 166], that are valid over the whole range of dimensionless wall distance y^+.

Notwithstanding the above, it is well known that classical and almost all existing unified wall functions are inadequate to describe complex heat and fluid flow situations because

most formulations are based on simple equilibrium flow assumptions [137]. However, recently some proposals were made in the literature to improve and generalize existing wall treatments, most of them based on numerical methods. For instance, Shih et al. [163] used a hybrid velocity scale u_c, which consists of the skin friction velocity and the pressure gradient velocity, for scaling a general boundary layer flow. By means of this, they constructed a unified velocity wall function that accounts for adverse and favorable pressure gradients. In another approach, the so called "analytical wall functions" by Craft et al. [32, 33], the near-wall region is divided into a viscous dominated and a fully turbulent part. Thereby, analytical expression is formulated for each part based on a simple prescribed distribution of turbulent viscosity, and non-equilibrium effects like pressure gradients and buoyancy are retained in the analytical wall function formulation. Based on this, Suga et al. [180] proposed a two-segment piecewise linear formulation of the subgrid scale eddy viscosity inside the wall-adjacent cell, which allows to use the analytical wall function approach in the framework of LES. A similar approach, the "compound wall treatment" were proposed by Popovac and Hanjalic [143]. In contrast to the analytical wall functions, they adopted a simpler formulation of the eddy viscosity along with smooth blending functions in order to derive analytical expressions for the velocity and temperature that are valid over the whole range of y^+. Additionally, they incorporate a correction factor that accounts for local non-equilibrium heat and fluid flow effects. Recently, Dzanic and Oefelein [49] proposed a similar non-equilibrium wall function for the momentum boundary layer by including a forcing term in their formulation that accounts for the effects of convection and pressure gradients. Several well-known velocity wall functions from literature are listed in Tab. 2.2. Note that the nomenclature refer to the original literature. Novel non-equilibrium wall function formulation that are applicable for complex turbulent flows with heat transfer has been proposed by the present author in [104], which is described with more detail in Chapter 3 of the present thesis.

Table 2.2: Several well-known velocity wall functions (nomenclature refers to the original literature.)

Classic wall function [191]	$u^+ = \begin{cases} y^+ & y^+ \leq 5 \\ \frac{1}{\kappa}\log(By^+) & y^+ \geq 30 \end{cases}$
Musker wall function [121]	$u^+ = 5.424\tan^{-1}\left(\frac{2y^+ - 8.15}{16.7}\right) + \lg\left(\frac{(y^+ + 10.6)^{9.6}}{(y^+ - 8.15y + 86)^2} - 3.52\right)$
Spalding wall function [172]	$y^+ = u^+ + \Big(\exp(\kappa u^+) - 1 - \kappa u^+ - \frac{1}{2}(\kappa u^+)^2 - \frac{1}{6}(\kappa u^+)^3\Big)$
Shih wall function [163]	$y_\tau^+ = U_1^+ + \Big(\exp(\kappa U_1^+) - 1 - \kappa U_1^+ - \frac{1}{2}(\kappa U_1^+)^2 - \frac{1}{6}(\kappa U_1^+)^3\Big)$ $(y_p^+)^2 = U_2^+ + \exp(-3.2)\Big(\exp(U_2^+/5) - 1 - U_2^+/5\Big)$
"Analytical wall functions" by Craft et al. [32, 33]	$u^* = \begin{cases} \frac{C_U}{2\mu}y^{*2} + \frac{A_U}{\mu}y^* + B_U & y^* \leq y_\nu^* \\ \frac{C_U}{\alpha\mu}y^* + \left(\frac{A'_U}{\alpha\mu} - \frac{C_U}{\alpha^2\mu(1_\alpha y_\nu^*)}\right) & \\ \quad \times \ln\left(1 + \alpha(y^* - y_v^*)\right) + B'_U & y^* \geq y_\nu^* \end{cases}$
"Unified" classic wall function with Kader blending [77, 143]	$u^+ = y^+\exp\left(-\frac{0.01y^{+4}}{1+5y^+}\right) + \left(\frac{1}{\kappa}\ln(By^+)\right)\exp\left(-\frac{1+5y^+}{0.01y^{+4}}\right)$
Compound wall function by Popovac and Hanjalic [143]	$u^+ = y^+\exp\big(-\frac{0.01y^{+4}}{1+5y^+}\big) + \big(\frac{1}{\kappa}\ln(Ey^+)\big)\exp\big(-\frac{1+5y^+}{0.01y^{+4}}\big)$

2.4 Conjugate heat transfer

Conjugate heat transfer can be found in many engineering applications, such as internal combustion engines, cooling of electronic components, exhaust gas after-treatment devices or general-purpose cooling and heating systems. It features a thermal energy transfer process that involves the interaction of conduction within a solid body and convection from the solid surface by fluid motion [72, 105]. The mathematical solutions of the governing equations are considered separately for the solid and the fluid domains that are coupled at the solid–fluid interface. It therefore requires a coupling of the conduction in the solid part and the convection in the fluid region.

In the case, where the structural fields of the solid wall such as structural stresses, deformation etc. and chemical reactions are not considered, the conjugate heat transfer problem can be divided into three main regions, namely a non-isothermal fluid flow region, a transient heat conduction through the solid and a thermal solid/fluid interface. The heat and fluid flow in the fluid region can be described by means of the balance laws for mass, momentum and energy (see Section 2.1). In the solid region, the velocity is zero in all the balance equations and only the energy equation has to be solved, which further simplifies in the case of Fourier heat transport to the classical heat equation:

$$\frac{\partial T^s}{\partial t} = \frac{\partial}{\partial x_i}\left(\alpha^s \frac{\partial T^s}{\partial x_i}\right). \tag{2.17}$$

Here, T^s represents the solid temperature and α^s the thermal diffusivity of the solid. Finally, the solid and fluid regions are coupled via a thermal interface, on which the temperature and the heat flux of both phases have to be equal, that leads to the following constraints at the solid/fluid interface:

$$T^s = T^f \qquad \rho^f c_p^f \alpha^f \frac{dT^f}{dn} = \lambda^s \frac{dT^s}{dn}, \tag{2.18}$$

where ρ^f is the fluid density, c_p^f the specific heat capacity of the fluid, $\lambda^s = \rho^s c_p^s \alpha^s$ the thermal conductivity of the solid and n represents the direction normal to the solid surface.

Chapter 3

Development of LES modeling of turbulent heat transfer

Accurate predictions of turbulent flows with heat transfer are of profound importance in the design of many engineering applications, e.g. internal combustion engines, cooling/heating devices or exhaust gas after-treatment systems. However, in spite of decades of research, it is still not possible to predict the evolution of turbulent flows analytically. Therefore, CFD is usually applied by engineers and researchers to solve the equations governing turbulent flows with heat transfer.

With regard to the CFD investigation of turbulent flows, the most accurate numerical approach is the so-called direct numerical simulation (DNS) that requires sufficiently fine spatial and temporal resolutions to fully resolve the entire spectrum of turbulent length and time scales, respectively. The associated computational cost of DNS is therefore extremely high, in particular for real life turbulent flows with high Reynolds numbers. Thus, DNS is mostly limited to academic studies, e.g. to get a deeper insight of turbulence mechanisms or well proven data for validation or verification purpose. In contrast to DNS, approaches that are based on the solution of the RANS equations require a significantly lower computational cost, which allow to analyse many realistic engineering flows at high Reynolds numbers. In RANS, turbulent motions are represented in a time-averaged manner, which leads to fully modeled, time-averaged solutions of the governing equations. However, it is well-known that the RANS approaches are often lack of accuracy and not reliable in the case of turbulent flows with large unsteady characters as well as in the case of turbulent flows including complex heat transfer phenomena. As a result, many researchers apply LES technique, which is proven to be more accurate than RANS while requiring significantly less computational effort than DNS, to analyse the turbulent flows with heat transfer.

In LES, the large-scale turbulent motions are resolved directly by the numerical grid, while the effects of the smaller scales are modeled using subgrid-scale models. Therefore, LES is anticipated to be accurate and reliable. However, similar to RANS, it is a well known fact that LES experiences shortcomings in dealing with near-wall dominated flows unless very fine grids are used in the vicinity of the wall [137]. This makes LES for simulating wall-bounded flows computationally very expensive and impedes its application in realistic industrial flows that involve solid walls. To circumvent this problem, a common practice in CFD is to model the near-wall region, e.g. by means of wall functions [32, 58, 137]. Thereby, the thin momentum and thermal boundary layers at the wall are bridged with a single cell while suitable assumptions are made for the near-wall velocity and temperature profiles in order to obtain the required wall shear stresses and wall heat fluxes, respectively. By bypassing the thin boundary layer, the computational cost of

LES can be significantly reduced, making LES feasible for simulating high Reynolds and Prandtl number flows and enabling its application to realistic industrial flow scenarios.

In this chapter, first, the existing classical LES-modeling approaches of turbulent flow with heat transfer are discussed, in which some well-known LES models and the near-wall treatments in LES and their predictive capabilities are briefly reviewed. Subsequently, a novel non-equilibrium wall function approach for LES of complex turbulent heat and fluid flow is proposed, and its validity is demonstrated through comparison with available reference data.

3.1 Existing modeling approaches for LES

Numerous LES approaches and subgrid-scale (SGS) models can be found in the literature. This section presents the basic concept of LES with implicit filtering and discusses several classical subgrid-scale models that are relevant to the present work. Comprehensive information on the theory and application of LES can be found in references such as [88, 142, 156].

3.1.1 Concept of LES

In LES, the large energy containing turbulent motions, which are characterized as low-frequency and essentially anisotropic, are resolved directly in space and time, while the effects of the smaller, high-frequency scales, which tend to be universal, homogeneous and isotropic, are approximated by a subgrid-scale turbulence model. A schematic view of this concept of scale separation is depicted in Fig 3.1.

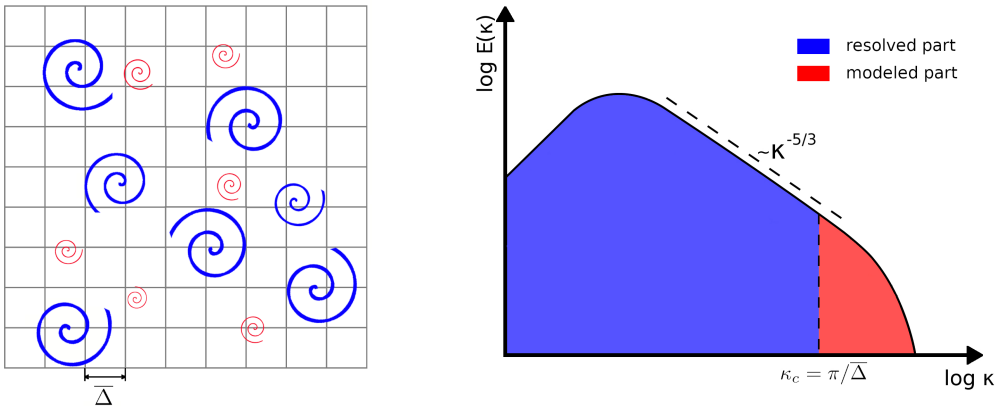

(a) (b)

Figure 3.1: Schematic view of the simplest scale separation operator

Fig. 3.1 (a) shows the resolved motions (in blue), which are larger than the cutoff length (filter-width) $\overline{\Delta}$ and therefore captured by the numerical grid, while the unresolved scales (in red) are smaller than $\overline{\Delta}$ and thus can not be resolved by the numerical grid. This scale separation is also illustrated in Fourier space by means of the energy spectrum of the turbulent motions (see Fig. 3.1 (b)). Thereby, the total energy is decomposed into a resolved part and a subgrid part, which are separated by the cutoff wave number $\kappa_c = \pi/\overline{\Delta}$.

The turbulent scales are separated mathematically by applying a low-pass convolution filter operator to a given quantity $\psi(\mathbf{x})$ which contains all scales of motions. The filtered

quantity, i.e. the quantity of large scale, is defined formally as [141]:

$$\overline{\psi}(\mathbf{x}) = \int_{-\infty}^{\infty} G(\mathbf{r}, \mathbf{x})\psi(\mathbf{x} - \mathbf{r})d\mathbf{r} =: G * \psi, \tag{3.1}$$

where $G(\mathbf{r}, \mathbf{x})$ is the convolution of filter kernel, for example in LES practice the most widely used box filter, Gaussian filter and sharp spectral filter [150]. The residual part of $\psi(\mathbf{x})$, i.e. the quantity of subgrid scale, denoted by $\psi'(\mathbf{x})$, is given by:

$$\psi'(\mathbf{x}) = \psi(\mathbf{x}) - \overline{\psi}(\mathbf{x}) = (1 - G) * \psi. \tag{3.2}$$

Usually, a Favre-filtering is used to simplify the set of LES equations for turbulent heat and flow with variable density, which is defined as

$$\widetilde{\psi} = \frac{\overline{\rho\psi}}{\overline{\rho}}. \tag{3.3}$$

The turbulent quantity ψ is decomposed into a Favre-filtered part and a residual part as

$$\psi = \widetilde{\psi} + \psi'', \tag{3.4}$$

with ψ'' denotes the fluctuation with respect to Favre-filtering.

By applying the filter operators mentioned above to the balance laws of an incompressible Newtonian fluid with variable physical properties and Fourier heat flux (see table 2.1), the LES transport equations of mass, momentum and enthalpy can be simplified as [150, 156]:

$$\frac{\partial\overline{\rho}}{\partial t} = -\frac{\partial}{\partial x_i}\left(\overline{\rho}\widetilde{U}_i\right), \tag{3.5}$$

$$\frac{\partial\overline{\rho}\widetilde{U}_i}{\partial t} = -\frac{\partial}{\partial x_j}\left(\overline{\rho}\widetilde{U}_i\widetilde{U}_j\right) - \frac{\partial\overline{p}}{\partial x_i} + \frac{\partial}{\partial x_j}\left(\overline{\tau}_{ij} - \overline{\rho}\tau_{ij}^{sgs}\right) + \overline{\rho}g_i, \tag{3.6}$$

$$\frac{\partial\overline{\rho}\widetilde{h}}{\partial t} = -\frac{\partial}{\partial x_j}\left(\overline{\rho}\widetilde{U}_j\widetilde{h}\right) + \frac{\partial}{\partial x_i}\left(\frac{\overline{\lambda}}{\overline{c}_p}\frac{\partial\widetilde{h}}{\partial x_i} - \overline{\rho}q_i^{sgs}\right), \tag{3.7}$$

where the subgrid parts, $\tau_{ij}^{sgs} = \left(\widetilde{U_iU_j} - \widetilde{U}_i\widetilde{U_j}\right)$ in the momentum equation and $q_i^{sgs} = \left(\widetilde{U_ih} - \widetilde{U}_i\widetilde{h}\right)$ in the energy equation, are closed by subgrid scale models for the momentum transport and for heat transport, respectively. Note that, usually, the isotropic part of the unknown subgrid-scale stress tensor τ_{ij}^{sgs} is superimposed to the modified filtered pressure, which leads to:

$$\overline{P} = \overline{p} + \frac{1}{3}\overline{\rho}\tau_{kk}^{sgs} \tag{3.8}$$

with

$$\tau_{\langle ij\rangle}^{sgs} = \tau_{ij}^{sgs} - \frac{1}{3}\tau_{kk}^{sgs}\delta_{ij}. \tag{3.9}$$

In LES practice, algebraic eddy viscosity or differential subgrid-scale models are most often applied to close the filtered momentum equation, while for subgrid-scale heat transport, both isotropic and anisotropic subgrid scale heat flux models are commonly used to close the filtered energy equation (see e.g. [150]). The following subsections provide a brief discussion of the most commonly used models.

3.1.2 Subgrid–scale models for momentum transport

Under the assumption that the behavior of the subgrid scales is analogous to the Brownian motion superimposed on the motion of the resolved scales [156], the subgrid model for $\tau^{sgs}_{\langle ij \rangle}$ is expressed as a function of subgrid viscosity ν_{sgs} using the Boussinesq approximation:

$$\tau^{sgs}_{\langle ij \rangle} = -2\nu_{sgs}\left(\widetilde{D}_{ij} - \frac{1}{3}\widetilde{D}_{kk}\delta_{ij}\right), \tag{3.10}$$

where $\widetilde{D}_{ij} = \frac{1}{2}\left(\frac{\partial \widetilde{U}_i}{\partial x_j} + \frac{\partial \widetilde{U}_j}{\partial x_i}\right)$ is the resolved part of the rate of deformation tensor. Several well-known algebraic eddy viscosity models relevant to the present work are formulated in the following.

Smagorinsky model
The most well-known subgrid-scale viscosity model is the Smagorinsky model [165]. It is formulated as

$$\nu_{sgs} = (C_S\Delta)^2\,|\widetilde{D}_{ij}|, \tag{3.11}$$

where $C_S = 0.17$ is the Smagorinsky coefficient and $|\widetilde{D}_{ij}|$ the characterized time scale related operator that is defined as:

$$|\widetilde{D}_{ij}| = \sqrt{2\widetilde{D}_{ij}\widetilde{D}_{ij}}. \tag{3.12}$$

The Smagorinsky model mentioned above does not match the asymptotic behavior in the near-wall region, i.e. $\nu_{sgs} \propto y^3$. Therefore, as suggested in [139], the Smagorinsky model is modified by applying the van Driest wall damping function for the prediction of wall-bounded turbulent flow. The cutoff length Δ is thereby modified as

$$\Delta_{vDm} = min\left[\Delta, \frac{\kappa y}{C_\Delta}\left(1 - e^{\left(-A^+/y^+\right)^3}\right)^{1/2}\right]. \tag{3.13}$$

Alternatively, the asymptotic behavior in the near-wall region can be represented by means of the Germano dynamic procedure [56], which results in the well-known dynamic Smagorinsky model.

Wall-Adapting Linear Eddy-viscosity model
One of the most widely used zero-equation LES model is the wall-adapting linear eddy-viscosity (WALE) model, proposed by Nicoud in [123], in which the subgrid-scale eddy viscosity is defined as follows:

$$\nu_{sgs} = (C_W\Delta)^2\,\frac{\left(\mathbf{S}^d_{ij}\mathbf{S}^d_{ij}\right)^{3/2}}{\left(\overline{D}_{ij}\overline{D}_{ij}\right)^{5/2} + \left(\mathbf{S}^d_{ij}\mathbf{S}^d_{ij}\right)^{5/4}} \tag{3.14}$$

with $C_W = 0.5$. $\mathbf{S}^d_{ij}$ is the traceless symmetric part of the square of the velocity gradient tensor:

$$\mathbf{S}^d_{ij} = \frac{1}{2}\left(\overline{L}^2_{ij} + \overline{L}^2_{ji}\right) - \frac{1}{3}\delta_{ij}\overline{L}^2_{kk}, \tag{3.15}$$

with the velocity gradient tensor $L_{ij} = \partial U_i/\partial x_j$ and its square $\overline{L}^2_{ij} = \overline{L}_{ik}\overline{L}_{kj}$. In the WALE model, the correct asymptotic behavior ($\nu_{sgs} = O(y^3)$) is fulfilled directly without additional damping functions or dynamic procedure.

Sigma model
Another wall-adapting model is the so-called Sigma model (σ-model) [124], which is based on the singular values of the resolved velocity gradient tensor and given as

$$\nu_{sgs} = (C_\sigma \Delta)^2 \frac{\sigma_3 (\sigma_1 - \sigma_2)(\sigma_2 - \sigma_3)}{\sigma_1^2}, \tag{3.16}$$

with the model coefficient $C_\sigma = 1.5$ and σ_i the i^{th} singular value of the resolved velocity gradient tensor $\overline{L}_{ij}$. Since $\sigma_1 \geq \sigma_2 \geq \sigma_3 \geq 0$, the modeled ν_{sgs} is always non-negative. Similar to the WALE model, the expected asymptotic behavior $\nu_{sgs} = O(y^3)$ is automatically achieved in the near-wall region. In the σ-model ν_{sgs} vanishes in the case of pure shear or solid rotation flows and pure axisymmetric of isotropic contraction/expansion.

In addition to the algebraic eddy viscosity models mentioned above, differential subgrid-scale models are also reported in literature, e.g. in [115, 150, 203], where history and non-equilibrium effects in the unresolved scales are considered as well.

3.1.3 Subgrid–scale models for heat transport

In the case of temperature variance spectra, as shown in Fig. 2.2, three different regimes can be seen depending on the value of the molecular Prandtl number Pr. As a result, the modeling of the subgrid-scale heat flux depends significantly on the value of Pr. However, as pointed out by Ries in his PhD thesis [150], using an isotropic thermal diffusivity model with a constant Pr_{sgs} number is a good compromise between accuracy and model complexity in the case of $Pr \approx 1$, which matches the case of the present work, an isotropic subgrid-scale heat flux model is therefore selected to close the energy equation. Moreover, it is important to note that the subgrid-scale heat flux is modeled based on the resolved enthalpy rather than temperature.

Isotropic thermal diffusivity model with constant Pr_{sgs} number
Regarding the linear eddy-diffusivity hypothesis, the subgrid-scale heat flux vector q_i^{sgs} is proportional to the corresponding filtered enthalpy gradient, formulated as:

$$q_i^{sgs} = \left(\widetilde{U_i h} - \widetilde{U}_i \widetilde{h}\right) = -\alpha^{sgs} \frac{\partial \widetilde{h}}{\partial x_i}, \tag{3.17}$$

where the proportional factor α_{sgs} is the subgrid-scale heat diffusivity to be modeled. According to the Reynolds analogy and under the concept of subgrid-scale turbulent Prandtl number Pr_{sgs}, the α_{sgs} is modeled as:

$$\alpha_{sgs} = \frac{\nu_{sgs}}{Pr_{sgs}} \tag{3.18}$$

with $Pr_{sgs} = 0.42$, as suggested in [159]. Notably, depending on the specific configuration the value of Pr_{sgs} may vary in an interval of $[0.1, 1]$ [156]. Other subgrid-scale heat flux models based on different assumptions are also available and reported in literature, e.g. using the dynamic procedure [108, 119], approaches based on the Kolmogorov scaling [194] or anisotropic thermal diffusivity models [35, 69, 135, 152, 205].

3.1.4 LES with near-wall resolution

As described in Sec. 2.3, the turbulent motions in the vicinity of the wall differ significantly from the isotropic homogeneous turbulent flow, thus a special treatment of turbulent motions in the near wall region is required in the context of large-eddy simulation. One possible way to deal with this issue is to apply the LES with near-wall resolution approach.

As already pointed out, in the vicinity of solid walls, turbulent motions are usually not isotropic. Thus, the classical concept of LES fails in the near-wall region and sufficiently high spatial and temporal resolutions are required leading to the so-called near-wall resolved LES (WRLES). In this context, it is recommended, e.g. see [13, 136, 156, 206, 207], that the spatial resolution in spanwise direction is to be $\Delta x^+ \leq 30$, in wall normal direction $\Delta y^+ < 2$ and in streamwise direction $\Delta z^+ \simeq 100$. The required spatial resolution in the streamwise and spanwise directions in practice depends on various factors, such as the configuration being simulated, the chosen LES model and the level of turbulent quantities to be resolved. However, in general, it is suggested that the first grid point in the wall-normal direction should be placed within the zone of $y^+ \leq 1$. In practice, the spatial resolution of a specified case should be evaluated by means of a grid sensitivity study.

In the near-wall region the dominant shear-stress component is τ_{yz} (y wall normal direction and z streamwise direction) that the temporal averaged τ_{yz} is proportional to y^3: $\langle \tau_{yz} \rangle \propto y^3$. This asymptotic behavior holds true for both resolved part and subgrid scale part. All LES models mentioned in Sec. 3.1.2 are able to represent the former part of the shear-stress in the vicinity of the wall with sufficiently high resolutions, while the latter part, which is determined by the asymptotic behavior of the subgrid scale viscosity ν_{sgs}, might be predicted differently. For instance, the Smagorinsky model, in which $\nu_{sgs} \propto \Delta^2$, is usually modified by means of a van Drist damping function (see [139]). Therefore, to simulate a wall-bounded turbulent flow, ν_{sgs} modeled by a LES-model has to vanish in the near wall region proportional to y^3, which is achieved by the LES-model itself or by using a damping function.

In context of this work, the Pr number is near to one, which implies that the near-wall behavior of the enthalpy (or temperature) field is similar to the flow field. Therefore, it is reasonable to apply the linear eddy diffusivity model with constant Pr_{sgs} to model the unresolved enthalpy (temperature) field.

3.1.5 LES with near-wall modeling

In WRLES, very fine spatial and temporal resolutions are required to resolve the turbulent motions in the thin boundary layer in the vicinity of solid walls. Thereby, the computational cost could be very high, especially in the prediction of complex turbulent flows with high Reynolds numbers. In order to overcome this issue, it is common practice in LES to use a near-wall modeling approach to reduce the required computational effort of the numerical simulation. In general, such near-wall modeling strategies can be divided in the context of LES into approaches based on wall functions (WFLES), two-layer RANS–LES (zonal LES) and hybrid RANS–LES methods [137].

LES with classical wall functions

Regarding WFLES, the momentum and thermal boundary layers are not explicitly resolved using a very fine numerical grid near the wall. Instead, they are bridged with a single cell while suitable assumptions are made for the near-wall velocity and temperature profiles [104]. Thereby, in the case of classical wall functions, a linear variation of the near-wall

velocity is assumed very close to the wall and a semi-logarithmic variation away from it (e.g., [121, 172, 191]). Based on Reynolds analogy assumptions, similar variation is also found for the near-wall temperature profile (e.g., [38, 74, 77, 148]).

A selection of wall functions commonly used in CFD simulations are briefly described in the following, namely, the velocity/temperature wall function of Launder and Spalding [101], the unified velocity wall function of Spalding [172], the generalized velocity wall function of Shih et al. [163] and the unified temperature wall function of Kader [77].

Standard velocity/temperature wall functions of Launder and Spalding [101]
The most widely applied wall function approach in CFD is based on the work of Launder and Spalding [101]. In the case of the velocity, the logarithmic law of the mean velocity is applied when $y^+ > 11.225$, whereas the linear solution of the viscous sublayer is used in the case of the mesh is such that $y^+ \leq 11.225$ at the wall-adjacent cells. This leads to:

$$u^+ = \begin{cases} y^+ & y^+ \leq 11.225, \\ \frac{1}{\kappa} \log\left(B y^+\right) & y^+ > 11.225, \end{cases} \tag{3.19}$$

where $u^+ = U/u_\tau$ and $y^+ = y u_\tau / \nu$ are the dimensionless mean velocity and wall distance, respectively. u_τ is the friction velocity, ν the kinematic viscosity, $\kappa \approx 0.4187$ the von Kármán constant and $B = 9.793$ an empirical constant. By means of equation 3.19, the required wall shear stress can be obtained using an iterative procedure.

In analogy to the standard velocity wall function, the composite form of the standard temperature wall function reads

$$T^+ = \begin{cases} Pr\ y^+ & y^+ \leq 11.225, \\ Pr_t \left(\frac{1}{\kappa} \log\left(B y^+\right) + P\right), & y^+ > 11.225, \end{cases} \tag{3.20}$$

where $T^+ = (T_w - T)/(T_\tau)$ is the dimensionless temperature, $T_\tau = |q_w|/(\rho c_p u_\tau)$ the friction temperature, T_w the wall temperture, q_w the wall heat flux, ρ the mass density, c_p the specific heat capacity, Pr the molecular Prandtl number and Pr_t the turbulent Prandtl number. P is an additional resistance function that accounts for the influence of different Pr numbers. Various resistance functions were proposed in the literature (see e.g. [74, 77, 101, 111]). During the evaluation of this wall function in the present work the resistance function of Kader [77] is applied that reads

$$P = \left(3.85 Pr^{1/3} - 1.3\right)^2 + 2.12 \ln(Pr). \tag{3.21}$$

This empirical relation is applicable for $Pr \in (6 \times 10^{-3},\ 4.0 \times 10^4)$.

Unified velocity wall function of Spalding [172]
Based on the classical wall function formulation of von Kármán [191], Spalding [172] proposed a single formula that is valid over the entire boundary layer (viscous sublayer, buffer layer, inertia sublayer). This unified wall function formulations reads:

$$y^+ = U^+ + 0.1108 \left(\exp\left(\kappa U^+\right) - 1.0 - \kappa U^+ - \frac{\left(\kappa U^+\right)^2}{2!} - \frac{\left(\kappa U^+\right)^3}{3!} - \frac{\left(\kappa U^+\right)^4}{4!} \right), \tag{3.22}$$

whereby the required wall shear stress can be solved iteratively with known velocity and wall distance at first wall-adjacent cell.

Generalized velocity wall function of Shih et al. [163]
A generalized velocity wall function formulation that accounts for adverse and favorable pressure gradients was proposed by Shih et al. [163]. In this wall function, the velocity is decomposed into two parts:

$$U = U_1 + U_2, \tag{3.23}$$

where U_1 is related to the streamwise pressure gradient dp_w/dz, while U_2 depends only on the wall shear stress τ_w. U_1 can be calculated from the streamwise pressure gradient as

$$\left(y_p^+\right)^2 = U_1^+ + 0.0408\left[exp\left(U_1^+/5\right) - 1 - U_1^+/5\right], \tag{3.24}$$

where $y_p^+ = yu_p/\nu$, $U_1^+ = 2U_1/u_p$ and $u_p = \left[(\nu/\rho)\left|dp_w/dz\right|\right]^{1/3}$. While U_2 is calculated from equation 3.23 as $U_2 = U - U_1$ and the required wall shear stress is solved iteratively from the unified velocity wall function of Spalding, i.e. replacing U in Eq. (3.22) by U_2:

$$y_\tau^+ = U_2^+ + 0.1108\left(\exp\left(\kappa U_2^+\right) - 1.0 - \kappa U_2^+ - \frac{\left(\kappa U_2^+\right)^2}{2!} - \frac{\left(\kappa U_2^+\right)^3}{3!} - \frac{\left(\kappa U_2^+\right)^4}{4!}\right), \tag{3.25}$$

where $y_\tau^+ = yu_\tau/\nu$ and $U_2^+ = U_2/u_\tau$.

Unified temperature wall function by Kader [77]
An approximation for equilibrium thermal boundary layers that is valid over the whole range of dimensionless wall distance y^+ was suggested by Kader [77], which reads

$$T^+ = Pry^+\exp(-\Gamma) + \left[2.12\ln(y^+) + P\right]\exp(-1/\Gamma), \tag{3.26}$$

where P is a resistance function given by Eq. (3.21) with the blending coefficient Γ:

$$\Gamma = \frac{0.01\left(Pry^+\right)^4}{1 + 5Pr^3y^+}. \tag{3.27}$$

Two-layer RANS-LES approach

In the case of two-layer RANS-LES approach, also known as the zonal LES approach, an auxiliary numerical grid with a fine spatial resolution is embedded between the matching location of the outer mesh for LES calculation and the solid wall within the fluid region. A simplified set of RANS-based turbulent boundary-layer equations are solved at the embedded mesh region. By means of this, the required wall shear stress is calculated and employed as a wall boundary condition for the LES calculation on the overlapped outer mesh [106, 137]. Thereby, pressure gradient and convection effects are taken into account from the solution of the RANS-based turbulent boundary-layer equations. Consequently, two-layer models are also able to capture, to some extent, non-equilibrium heat and fluid flow effects. Nevertheless, it was observed in many numerical studies [14, 84, 132] that two-layer models tend to over-predict the wall shear stress. In addition to this, the generation of two separate numerical grids could be very challenging, in particular for complex geometries.

The inner-layer can be modeled using different RANS models, for instance, in the work by the present author [106] and co-authors, the Spalart-Allmaras [169] model has

been applied onto the embedded mesh. The Spalart-Allmaras RANS model reads [169]:

$$\frac{\partial \widetilde{\nu}}{\partial t} + \frac{\partial}{\partial x_i}\left(\overline{U}_i \widetilde{\nu}\right) = C_{b1}\widetilde{S}\widetilde{\nu} + \frac{1}{\sigma_{\nu_t}}\left[\frac{\partial}{\partial x_j}\left(\left(\nu + \widetilde{\nu}\right)\frac{\partial \widetilde{\nu}}{\partial x_j}\right) + C_{b2}\frac{\partial \widetilde{\nu}}{\partial x_j}\frac{\partial \widetilde{\nu}}{\partial x_j}\right] - C_{w1} f_w \left(\frac{\widetilde{\nu}}{\widetilde{d}}\right)^2, \tag{3.28}$$

where the turbulent viscosity is calculated by

$$\nu_t = \widetilde{\nu} f_{\nu 1}, \qquad f_{\nu 1} = \frac{\chi^3}{\chi^3 + C_{\nu 1}^3}, \qquad \chi := \frac{\widetilde{\nu}}{\nu}. \tag{3.29}$$

The coefficients in the Spalart–Allmaras RANS model are defined as

$$\widetilde{S} = \sqrt{2\overline{\Omega}_{ij}\overline{\Omega}_{ij}} + \frac{\widetilde{\nu}}{\kappa^2 \widetilde{d}^2} f_{\nu 2}, \qquad f_{\nu 2} = 1 - \frac{\chi}{1 + \chi f_{\nu 1}},$$
$$f_w = g\left[\frac{1 + C_{\omega 3}^6}{g^6 + C_{\omega 3}^6}\right]^{1/6}, \qquad g = r + C_{\omega 2}\left(r^6 - r\right), \qquad r := \frac{\widetilde{\nu}}{\widetilde{S}\kappa^2 \widetilde{d}^2}, \tag{3.30}$$

where $\overline{\Omega}_{ij} = 1/2\left(\partial \overline{U}_i/\partial x_j - \partial \overline{U}_j/\partial x_i\right)$ is the rotation tensor and $\widetilde{d}$ a characteristic length scale defined as the distance to the wall. The model constants are listed in the following

$$\sigma_{\nu_t} = 2/3, \quad C_{b1} = 0.1355, \quad C_{b2} = 0.622, \quad C_{\omega 1} = C_{b1}/\kappa^2 + (1 + C_{b1})/\sigma_{\nu_t},$$
$$C_{\omega 2} = 0.3, \quad C_{\omega 3} = 2, \quad C_{\nu 1} = 7.1, \quad \kappa = 0.41.$$

Note that in contrast to the original Spalart–Allmaras RANS model, the trip term in Eq. 3.28 is not considered in the present model formulation. Thereby, at the outer layer, the WALE model [123] mentioned above has been employed to model the sub-grid scale structures for the LES calculation.

In the zonal LES approach, the resolved velocity and the pressure gradient from the LES calculation at the matching position serve as boundary conditions for the inner-layer RANS simulation. Whereas, the wall stress from the RANS is returned as wall boundary condition for the LES calculation. Regarding the treatment of the thermal boundary layer, the turbulent thermal diffusivity α_t can be calculated in the zonal LES approach based on Reynolds analogy assumptions as $\alpha_t = \nu_t / Pr_t$.

Improved Delayed Detached Eddy Simulation [164]

In hybrid RANS–LES modeling approaches, a RANS model is applied in the vicinity of the solid surface, while LES equations with a subgrid-scale model are solved away from the wall. In this framework, different strategies can be used for the transition from a RANS behavior to a LES behavior, based on criteria updated during the computation [21]. For instance, the turbulent length scale can be changed from a RANS mixing length scale to a grid size-related length scale, or a blending function can be used to merge the RANS and subgrid-scale eddy viscosity [137]. In contrast to wall-resolved LES of conjugate heat transfer, where the grid has to be refined isotropically in all three directions in the vicinity of the solid surface in the fluid region, hybrid RANS–LES requires only grid refinement in the wall-normal direction, leading to a significant reduction in the computational cost [62]. Prominent examples of hybrid RANS–LES models are Detached–Eddy Simulations (DES)

[171], Delayed Detached–Eddy Simulations (DDES) [170], Improved Delayed Detached–Eddy Simulation (IDDES) [164], Very Large–Eddy Simulation (VLES) [173] or Scale–Adaptive Simulations (SAS) [116].

Similar to [164], in the work [106] of the present author, the Spalart–Allmaras eddy viscosity transport equation (see Eq. (3.28)) has been used in the IDDES approach in order to calculate the eddy viscosity. Thereby, in contrast to the classical Spalart-Allmaras RANS model, a hybrid turbulent length-scale formulation, that blends between a RANS and a LES length scale, has been used for the approximation of $\widetilde{d}$ as [61]:

$$\widetilde{d} = \widetilde{f}_d(1 + \widetilde{f}_e)l_{RANS} + (1 - \widetilde{f}_d)l_{DES}. \tag{3.31}$$

Here, l_{RANS} is a RANS-based turbulent length scale and l_{DES} a length scale that depends on the grid width. The RANS-based turbulent length scale equals to the distance to the wall $l_{RANS} = d$. The grid-based length scale is calculated as $l_{DES} = \Psi C_{DES}\Delta$, where Ψ is the low Reynolds number correction function (see [164]), $\Delta = (\Delta_x\Delta_y\Delta_z)^{1/3}$ the grid filter and $C_{DES} = 0.65$ a model constant. The blending function $\widetilde{f}_d$ in Equation (3.31) is defined in such a way that l_{RANS} is predominantly used in regions with low mesh resolution and l_{DES} in regions where the grid resolution is sufficient for LES. The elevation function f_e aims at preventing an excessive reduction in the Reynolds stresses in the vicinity of the RANS–LES interface [61]. A detailed description of the IDDES model and the blending functions can be found in [61, 164].

Similar to the zonal LES approach, the turbulent thermal diffusivity α_t can be calculated in IDDES based on Reynolds analogy assumptions as $\alpha_t = \nu_t/Pr_t$.

3.2 A novel wall-modeling approach for LES

In this section, a novel non-equilibrium wall function approach for LES predition of complex turbulent heat and fluid flow, including non-equilibrium velocity and temperature wall functions, is presented. It builds upon the methodology of Popovac and Hanjalic [143] to derive the generalized wall functions. Based on the assumption of a non-equilibrium correction function the local non-equilibrium heat and fluid flow effects are considered in this approach. In contrast to the "compound wall treatment" of Popovac and Hanjalic [143], no ad-hoc blending of the wall-limiting and fully turbulent properties is required in the present approach. Instead, single analytic expression for velocity and temperature that are continuously valid over the whole boundary layer are formulated, which are further consistent with the second law of thermodynamics. In addition, based on legitimate physical reasons, different assumptions for the variation of the non-equilibrium correction function and a revisited formulation for the turbulent Prandtl number as a function of the molecular Prandtl number are incorporated.

3.2.1 Velocity wall function

Following the description in [143], the two-dimensional momentum equation for the wall-tangential direction in boundary layer flows can be written in non-rotating reference frame in Euler representation as:

$$\frac{\partial}{\partial y}\left((\mu + \mu_t)\frac{\partial U}{\partial y}\right) = \frac{\partial \rho U}{\partial t} + \frac{\partial}{\partial x}(\rho UU) + \frac{\partial}{\partial y}(\rho VU) + \frac{\partial p}{\partial x} + \rho f_x, \tag{3.32}$$

where t is the time, x the flow direction, y the wall-normal direction, U and V are the velocity components in x and y directions, respectively, p is the pressure, μ the dynamic

viscosity, μ_t the turbulent viscosity, and f_x represents additional source term contributions (e.g. gravity). Notably, the flow direction x do not present a fixed direction like the wall normal direction, instead of that it represents a time dependent flow direction. Moreover, the right-hand side of Eq. 3.32 represents local non-equilibrium effects due to time rate change, convection, pressure gradients and additional source terms.

As pointed out by Popovac in [143], the term $\partial p/\partial x$ is fairly independent of y and can be taken as constant, which holds true for many additional volume forces f_x. In contrast, time rate change and convection terms are zero at solid walls while away from walls not necessarily to be zero. Thus, a better approximation in this case is to assume a linear dependency in respect to y. With these assumptions, Eq. 3.32 is integrated from the solid wall up to a distance y as

$$\left[(\mu+\mu_t)\frac{\partial U}{\partial y}\right]_y - \tau_w = \underbrace{\left[\frac{1}{2}\left(\frac{\partial \rho U}{\partial t}+\frac{\partial}{\partial x}(\rho UU)+\frac{\partial}{\partial y}(\rho VU)\right)+\frac{\partial p}{\partial x}+\rho f_x\right]_y}_{C_U} y. \tag{3.33}$$

Here $\tau_w = [(\mu+\mu_t)\,dU/dy]_{y=0}$ is the wall shear stress and all local non-equilibrium effects are combined into C_U. Then, inserting $U^+ = U/u_\tau$, $y^+ = \rho y u_\tau/\mu$, $C_U^+ = \mu C_u/\rho^2 u_\tau^3$ into Eq. 3.33 leads to the following expression for the dimensionless velocity gradient

$$\frac{dU^+}{dy^+} = \left(C_U^+ y^+ + \frac{\tau_w}{\rho u_\tau^2}\right)\frac{\mu}{\mu+\mu_t}, \tag{3.34}$$

in which an expression for the turbulent viscosity μ_t is required to close this equation with considering that $\mu_t/\mu \sim {y^+}^3$ very close to the wall [148] and $\mu_t/\mu = \kappa y^+$ away from the wall [100]. Furthermore, it is generally advantageous to choose a formulation for μ_t that is continuously valid over the entire momentum boundary layer in order to derive a single expression for the dimensionless near wall velocity profile. In the present work, the compact and continuous form for μ_t suggested by Musker [121] is utilized that fulfills both limiting regions. It reads

$$\mu_t = \frac{\mu C_0 \kappa {y^+}^3}{\kappa + C_0 {y^+}^2}, \tag{3.35}$$

where $C_0 = 9.6e\text{-}4$ is an universal proportionality constant valid for sufficient high Reynolds numbers [121] and $\kappa \approx 0.41$ the von Kármán constant. The validity of Eq. 3.35 is assessed for turbulent channel flow by the author in [104].

Finally, putting Eq. 3.35 into Eq. 3.34 and integrating again from the wall up to the distance y^+ leads to the single analytic expression of the novel unified velocity wall function as

$$\begin{aligned}
U^+ &= \frac{C_U^+}{\kappa}y^+ + \left(\frac{\tau_w}{\rho u_\tau^2} - \frac{C_U^+}{\kappa}\right)U_I^+ + \frac{\kappa C_U^+}{3a_U\kappa C_0 - 2C_0}\left(U_{II}^+ + 3\sqrt{\frac{a_U\kappa-1}{3a_U\kappa+1}}U_{III}^+\right),\\
U_I^+ &= \frac{1}{\kappa}\log\left(\frac{y^+ + a_U}{a_U}\right) - \frac{R^2}{a_U^2+4\gamma a_U}\left((4\gamma - a_U)U_{II}^+ + \frac{\gamma}{\beta}(4\gamma - 5a_U)U_{III}^+\right),\\
U_{II}^+ &= \log\left(\frac{a_U}{R}\frac{\sqrt{(y^+-\gamma)^2+\beta^2}}{y^+ + a_U}\right),\\
U_{III}^+ &= \arctan\left(\frac{y^+}{\beta} - \frac{\gamma}{\beta}\right) + \arctan\left(\frac{\gamma}{\beta}\right)
\end{aligned} \tag{3.36}$$

with $\Omega_U = \left(108\kappa^3 + 8C_0 + 12(81\kappa^6 + 12C_0\kappa^3)^{1/2}\right)^{1/3} = 2.294$, $a_U = \Omega_U / \left(6\kappa {C_0}^{1/3}\right) + 2{C_0}^{1/3}/(3\kappa\Omega_U) + 1/(3\kappa) = 10.337$, $\gamma = (-1/\kappa + a_U)/2 = 3.949$, $\beta = (2a_U\gamma - \gamma^2)^{1/2} = 8.127$ and $R = (\gamma^2 + \beta^2)^{1/2} = 9.036$.

3.2.2 Temperature wall function

In analogy to the velocity boundary layer, the energy equation for turbulent heat transfer across a thermal boundary layer can be written in non-rotating reference frame in Euler representation as:

$$\frac{\partial}{\partial y}\left((\alpha + \alpha_t)\frac{\partial T}{\partial y}\right) = \frac{\partial \rho c_p T}{\partial t} + \frac{\partial}{\partial x}(\rho U c_p T) + \frac{\partial}{\partial x}(\rho V c_p T) + \rho\omega, \tag{3.37}$$

where α and α_t denote the molecular and turbulent thermal conductivity, respectively, T the temperature, c_p the specific heat capacity, and ω an additional source term contribution (e.g. radiation, viscous heating or chemical reactions).

Assuming again that additional volume source terms ω are independent on y and that time rate change and convection terms have a linear dependency of y, allows to integrate Eq. 3.37 from the solid wall up to a distance y as

$$\left[(\alpha + \alpha_t)\frac{\partial T}{\partial y}\right]_y + q_w = \underbrace{\left[\frac{1}{2}\left(\frac{\partial \rho c_p T}{\partial t} + \frac{\partial}{\partial x}(\rho U c_p T) + \frac{\partial}{\partial x}(\rho V c_p T)\right) + \rho\omega\right]_y}_{C_T} y, \tag{3.38}$$

where $q_w = -\left[(\alpha + \alpha_t)\, dT/dy\right]_{y=0}$. Thereby, all local non-equilibrium effects are combined into C_T. Then, inserting $T^+ = (T_w - T)/T_\tau$, $T_\tau = q_w/(\rho c_p u_\tau)$, $y^+ = \rho y u_\tau/\mu$, $C_T^+ = \mu C_T/(\rho^2 u_\tau^2 c_p T_\tau)$ into Eq. 3.38 leads to the following expression for the dimensionless temperature gradient

$$\frac{dT^+}{dy^+} = \left(C_T^+ y^+ - \frac{q_w}{\rho c_p u_\tau T_\tau}\right)\frac{\alpha Pr}{\alpha + \alpha_t}, \tag{3.39}$$

where Pr is the molecular Prandtl number. Here, an expression for the turbulent thermal diffusivity is required to close Eq. 3.39. Thereby, based on the Reynold's analogy between momentum and energy transfer, it is assumed that the turbulent thermal conductivity behaves similar to the turbulent eddy viscosity in the near wall region. Based on this analogy with Eq. 3.35 it follows

$$\alpha_t = \frac{\alpha C_0 \kappa {y^+}^3}{\kappa + C_0 {y^+}^2}\frac{Pr}{Pr_t}. \tag{3.40}$$

A comparison of Eq. 3.40 with DNS data of turbulent heated channel flow can be found in [104]. Inserting Eq. 3.40 into Eq. 3.39 and integrating from the wall up to the distance y^+ leads to the single analytic expression for the novel unified temperature wall function as

$$\begin{aligned} T^+ =& \frac{C_T^+ \,\mathrm{Pr}_t}{\kappa} y^+ - \left(\frac{q_w}{\rho c_p u_\tau T_\tau} + \frac{C_T^+ \,\mathrm{Pr}_t}{\kappa \,\mathrm{Pr}}\right) T_I^+ \\ &+ \frac{\mathrm{Pr}\,\kappa C_T^+}{3\,\mathrm{Pr}\, a_T \kappa - 2\,\mathrm{Pr}_t}\left(T_{II}^+ + 3\sqrt{\frac{Pr a_T \kappa - Pr_t}{3\,\mathrm{Pr}\, a_T \kappa + \mathrm{Pr}_t}} T_{III}^+\right), \end{aligned} \tag{3.41}$$

$$
\begin{aligned}
T_I^+ =& \frac{\mathrm{Pr}_t}{\kappa}\log\left(\frac{y^+ + a_T}{a_T}\right) - \frac{\mathrm{Pr}\, R_T^2}{a_T^2 + 4\phi_T a_T}\left((4\phi_T - a_T)T_{II}^+ + \frac{\phi_T}{\psi_T}(4\phi_T - 5a_T)T_{III}^+\right),\\
T_{II}^+ =& \log\left(\frac{a_T}{R_T}\frac{\sqrt{(y^+ - \phi_T)^2 + \psi_T^2}}{y + a_T}\right),\\
T_{III}^+ =& \arctan\left(\frac{y^+}{\psi_T} - \frac{\phi_T}{\psi_T}\right) + \arctan\left(\frac{\phi_T}{\psi_T}\right),
\end{aligned}
\tag{3.42}
$$

with $k = Pr\kappa/Pr_t$, $\Omega_T = \left(108Pr_t k^3 + 8C_0 Pr + 12\sqrt{81Pr_t^2 k^6 + 12C_0 PrPr_t k^3}\right)^{1/3}$,
$a_T = \Omega_T/\left(6k(C_0 Pr)^{1/3}\right) + 2(C_0 Pr)^{1/3}/(3k\Omega_T) + 1/(3k)$, $\phi_T = (-1/k + a_T)/2$,
$\psi_T = \sqrt{2a_T\phi_T - \phi_T^2}$ and $R_T = \sqrt{\phi_T^2 + \psi_T^2}$.

Additionally, in order to model varying turbulent Prandtl numbers effects, the following empirical relation is used

$$
Pr_t = 0.85 + \frac{0.012}{Pr}, \tag{3.43}
$$

which is a reformulation of the relation provided in [75] for molecular Prandtl numbers in the range of $0.01 \leq Pr \leq 100$ estimated on the basis of the most reliable and recent DNS data-sets from the literature. A comparison of Eq. 3.43 with DNS data available in the literature is depicted in Fig. 3.2. Thereby, the turbulent Prandtl numbers in the reference DNS data are determined in the log-law region.

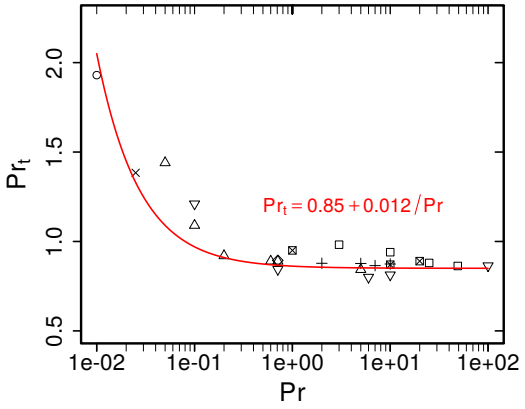

Figure 3.2: Turbulent Prandtl number as a function of molecular Prandtl number. ○ DNS of turbulent heated channel flow at $Re_\tau = 590$ [185]; △, +, ×, ◇ DNS of turbulent heated channel flow at $Re_\tau = 180, 395, 640, 1020$ [2, 3, 85]; ▽ DNS of turbulent heated channel flow at $Re_\tau = 395$ [175]; ⊠ DNS of turbulent heated pipe flow at $Re_\tau = 360$ [176]; ▽ DNS of passive scalar transport in turbulent channel flow at $Re_\tau = 180$ [175]; —: best fit of reference data.

In summary, the proposed novel non-equilibrium wall functions (Eq. 3.36 and Eq. 3.42) are continuously valid over the whole range of y^+, including transient and local non-equilibrium effects. They are also easily extendable to calculate additional source term contributions and are applicable for a wide range of molecular Prandtl numbers. By

choosing the interpolation formula of μ_t and α_t, the formulations are further consistent with the second law of thermodynamics as it is shown by the author in [104].

Chapter 4

Numerical treatment

The balance equations presented in Sec. 2.1 represent a system of partial differential equations (PDE) with time- and space-fractional derivatives, which can be hardly solved analytically. Alternatively, they are generally solved numerically. The most widely applied numerical method in CFD is the Finite Volume Method (FVM), which, due to its good performance in maintaining the conservation of the basic flow quantities (e.g. mass, momentum and energy), is employed in the present work. In the context of FVM, the solution domain and the integral formulation of the PDE are firstly discretized through a discretization procedure. Thereby, the integral formulation of the PDE is satisfied on each discrete region that is subsequently transformed into a corresponding algebraic equation. The algebraic equation is then formulated into a global algebraic equation system. Finally, the numerical solution of the original PDE is obtained by solving the algebraic equation system. In this chapter, the discretization procedure of the general balance equation is briefly summarized in Sec. 4.1. It is followed by the solution procedure for turbulent flow with conjugate heat transfer in Sec. 4.2. Finally, since the present work focuses on WFLES, the near-wall treatment is addressed in Sec. 4.3 as well. Moreover, the simulations in this work are conducted using OpenFOAM. Notably, the description in this chapter mainly focuses on the numerical treatment employed within the OpenFOAM framework, which is discussed in detail in [60, 73].

4.1 Discretization procedure

The discretization procedure in the context of FVM consists of two main steps: the discretization of the solution domain and the discretization of the PDE [67]. Firstly, the solution domain, which includes the space and time interval, is divided into a finite number of discrete regions known as control volumes (CV) or cells for the spatial discretization, and time steps for the temporal discretization. Subsequently, the integral formulation of the balance equations (see Sec. 2.1) is discretized and applied to the discrete regions.

The general balance equation is a parabolic equation in time, which can be solved numerically by marching in time from a initial condition. Therefore, the time discretization is accomplished by splitting the time interval into a finite number of successive time-steps. The size of time-steps can be evaluated, for instance, in OpenFOAM according to the Courant-Friedrichs-Lewy condition [31, 73, 150]. In line with Taylor series expansion, the first-order temporal derivative of ϕ is approximated as:

$$\frac{\partial \phi}{\partial t} \approx \frac{\phi^{n+1} - \phi^{n}}{\Delta t}, \tag{4.1}$$

which has a first-order accuracy in time. A second-order approximation reads:

$$\frac{\partial \phi}{\partial t} \approx \frac{\frac{3}{2}\phi^{n+1} - 2\phi^{n} + \frac{1}{2}\phi^{n-1}}{\Delta t}, \tag{4.2}$$

where $\phi^{n-1} = \phi(t - \Delta t)$, $\phi^{n} = \phi(t)$ and $\phi^{n+1} = \phi(t + \Delta t)$.

In the finite volume framework of OpenFOAM, the spatial solution domain is generally a three-dimensional space, which is completely filled by CVs without overlapping in the discretization procedure [73]. Here, a CV can be a general polyhedron, thus, allows a variable number of neighbours that facilitates the discretization of complex solution domains or a local refinement. A typical OpenFOAM control volume is depicted in Fig. 4.1, where

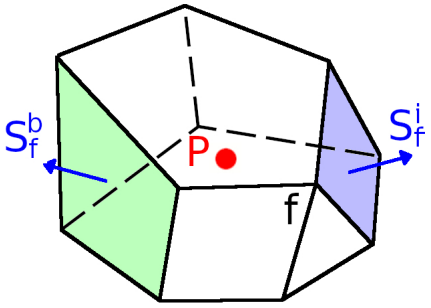

Figure 4.1: Schematic illustration of a typical OpenFOAM control volume.

P represents the centroid of the cell that is bounded by several flat faces f. A flat face can be either a interface (in blue in Fig. 4.1) of two neighbouring cells or a boundary face (in green in Fig. 4.1). In OpenFOAM, the so-called collocated or non-staggered variable arrangement is employed, in which all cell-averaged solution variables, e.g. velocity, pressure and temperature, are stored at the cell centroid of a CV. However, the value of variables on a interface is always necessary, e.g. to calculate the fluxes. Therefore, a face value, which is located at the face centre, is evaluated by interpolation using neighbouring cell values. In addition, a face area vector S_f is defined with a magnitude of the face area and normal to the associate flat face f. In the case of interface, S_f point outwards from the cell with the lower label (S_f^i in Fig. 4.1, assuming cell P has a lower label), while in the case of boundary faces, S_f points outwards from the computational domain (S_f^b in Fig. 4.1). The integration of ϕ over the CV P is approximated using the midpoint rule, which is second-order accurate, reads:

$$\int_{V_P} \phi \, \mathrm{d}V_P \approx \phi_P \int_{V_P} \mathrm{d}V_P = \phi_P V_P. \tag{4.3}$$

Similarly, the approximation of the integration over the cell surfaces is expressed as:

$$\int_S \varphi_i n_i \, \mathrm{d}S = \sum_f \left(\int_f \varphi_i n_i \mathrm{d}S \right) \approx \sum_f \varphi_{fi} S_{fi}, \tag{4.4}$$

where $(\cdot)_P$ denotes the cell-averaged value located at the cell centroid, and $(\cdot)_{fi}$ the value of ψ_i component at the cell-face center of face f.

In the context of FVM, the integral formulation of the general balance equation is satisfied on each CV, which leads to the local expression of the integral formulation [73,

150]:

$$\underbrace{\frac{\partial}{\partial t}\int_{V_P}\rho\phi\ \mathrm{d}V_P}_{\text{time derivative}}+\underbrace{\int_V \rho U_i\frac{\partial\phi}{\partial x_i}\ \mathrm{d}V}_{\text{convection}}-\underbrace{\int_V \frac{\partial}{\partial x_i}\left(\rho\Gamma\frac{\partial\phi}{\partial x_i}\right)\mathrm{d}V}_{\text{diffusion}}=\underbrace{\int_{V_P}\Sigma\mathrm{d}V_P}_{\text{sources}} \tag{4.5}$$

where ϕ is either a vector (e.g. for velocity) or scalar (e.g. for temperature), Γ the diffusion coefficient and $\Sigma = Z + \Pi$ summation of all sources (see also Table 2.1). It consists of a time derivative term, a convection term, a diffusion term, which includes a second derivative of ϕ in space, and a source term. These terms needs to be further disctetized spatially and temporally to transform the integral formulation of the PDE completely into a corresponding algebraic equation system.

Applying the Gauss' Theorem and the Eq. (4.4) to the convection term leads to a spatial discretization as [73]:

$$\begin{aligned}\int_V \rho U_i\frac{\partial\phi}{\partial x_i}\ \mathrm{d}V &= \int_S \rho U_i\phi n_i \mathrm{d}S\\ &\approx \sum_f F_f\phi_f,\end{aligned} \tag{4.6}$$

where, in the present work, the mass flux $F_f = (\rho U_i)_f S_{fi}$ through the interface f is determined by linear interpolation using neighbouring cell values. The unknown face value ϕ_f is approximated by means of a blended differencing scheme (BDS), which is a linear combination of central differencing scheme (CDS) and upwind differencing scheme (UDS):

$$\phi_f^{BDS} = \phi_f^{UDS} + \gamma\left(\phi_f^{CDS} - \phi_f^{UDS}\right). \tag{4.7}$$

Herein, the CDS has a second-order accuracy, in which ϕ_f is interpolated linearly from the cell values of both neighbouring cells, cell P and cell N, and reads [73]:

$$\phi_f^{CDS} = \frac{\overline{fP}}{\overline{PN}}\phi_P + \left(1 - \frac{\overline{fP}}{\overline{PN}}\right)\phi_N, \tag{4.8}$$

with $\overline{fP}$ the distance between face f and the cell centroid P, $\overline{PN}$ the distance between the cell centroids P and N. In the first-order UDS, ϕ_f is approximated according to the flow direction, namely is expressed as

$$\phi_f^{UDS} = \begin{cases}\phi_P \text{ if } F_f \geq 0\\ \phi_N \text{ if } F_f < 0\end{cases}. \tag{4.9}$$

Moreover, the blending factor γ, $0 \leq \gamma \leq 1$, can be either a constant parameter or adopted dynamically according to the local flow conditions. In the present work, the so-called "*filteredLinear3V*" flux-limited BDS of OpenFOAM is applied to calculate the face value ϕ_i, e.g. for velocity. However, a Minmod flux-limited BDS (see [155]) is employed to approximate the scalar quantities on the face centre, e.g. for temperature. A detailed description of the blending factor γ of these BDS is provided in [150]. If f is a boundary face, F_f and ϕ_f in Eq. 4.6 are specified by the boundary conditions.

In the similar way of the disctretization of the convection term, the diffusion term is approximated using the the Gauss' Theorem and the Eq. 4.4, yields:

$$\begin{aligned}\int_V \frac{\partial}{\partial x_i}\left(\rho\Gamma\frac{\partial\phi}{\partial x_i}\right)\mathrm{d}V &= \int_S \rho\Gamma_\phi\frac{\partial\phi}{\partial x_i}n_i\ \mathrm{d}S\\ &\approx \sum_f (\rho\Gamma)_f\left(\frac{\partial\phi}{\partial x_i}\right)_f S_{fi},\end{aligned} \tag{4.10}$$

in which the first-order derivative of ϕ is interpolated from the cell values of neighbouring cells. However, a non-orthogonal correction is required for a non-orthogonal mesh, therefore, the general expression is given by [73]:

$$\left(\frac{\partial \phi}{\partial x_i}\right)_f S_{fi} = \underbrace{|\Delta_{fi}| \frac{\phi_N - \phi_P}{|d_i|}}_{\text{orthogonal}} + \underbrace{k_{fi} \left(\frac{\partial \phi}{\partial x_i}\right)_f}_{\text{non-orthogonal}}, \tag{4.11}$$

where $|\cdot|$ represents the magnitude of a vector, d_i the vector points from P to N, and the surface gradient in the non-orthogonal part is approximated by CDS using the gradient of ϕ at adjacent cell centroids, expressed as:

$$\left(\frac{\partial \phi}{\partial x_i}\right)_f = \frac{\overline{fN}}{\overline{PN}} \left(\frac{\partial \phi}{\partial x_i}\right)_P + \left(1 - \frac{\overline{fN}}{\overline{PN}}\right) \left(\frac{\partial \phi}{\partial x_i}\right)_N. \tag{4.12}$$

Moreover, Δ_{fi} and k_{fi} are component vectors of S_{fi} with $S_{fi} = \Delta_{fi} + k_{fi}$. Δ_{fi} is computed based on the "over-relaxed" correction approach (see [73]) as

$$\Delta_{fi} = \frac{d_i}{d_j S_{fj}} |S_{fk}|^2, \tag{4.13}$$

k_{fi} vanishes in the case of orthogonal meshes. In the case of f being a boundary face, the gradient of ϕ is calculated with the specified value of ϕ on the boundary face.

Generally the source term Σ in equation 4.5 could be a (non-linear) function of the dependent variable ϕ. Thus, in the FVM framework of OpenFOAM, the source term is linearized in a general form:

$$\Sigma_P(\phi) = \Sigma_P^u + \Sigma_P^p \phi_P, \tag{4.14}$$

where Σ_P^u and Σ_P^p can be function of ϕ_P [134]. From equation 4.3, the source terms in Eq. 4.5 is calculated as

$$\int_{V_P} \Sigma_P(\phi)\, dV_P = \Sigma_P^u V_P + \Sigma_P^p V_P \phi_P, \tag{4.15}$$

which consists of an explicit and an implicit part. As suggested by Jasak in [73], the source term should be computed as "implicitly" as possible. A second-order representation of the non-linearities is achieved by the iterative solution procedure [73, 150], which holds also true for the linearized convection term in momentum equation.

By applying the above mentioned spatial discretization, e.g. Eq 4.3, 4.6, 4.10 and 4.15, to the general balance equation 4.5 leads to:

$$\begin{aligned}\left(\frac{\partial \rho_P \phi_P}{\partial t}\right)_P &= \frac{1}{V_P}\left[-\sum_f F_f \phi_f + \sum_f (\rho\Gamma)_f \left(\frac{\partial \phi}{\partial x_i}\right)_f S_{fi} + \Sigma_P^u V_P + \Sigma_P^p V_P \phi_P\right] \\ &= R(\phi),\end{aligned} \tag{4.16}$$

which is given in the so-called semi-discretized form. In the present work, the second-order implicit backward-differencing method is employed to discretize the time derivative. The l.h.s of Eq. 4.16 is discretized by the Eq. 4.2, in which ϕ^{n-1} and ϕ^n are known from previous time steps, the unknown ϕ^{n+1} will be solved from the corresponding system of algebraic equations. If ϕ^{n-1} is not available, Eq. 4.1, the first order Euler implicit scheme, is applied. ϕ in r.h.s. of Eq. 4.16 is computed implicitly by using value of variables at $n+1$ time-level, namely $R(\phi) = R(\phi^{n+1})$.

Applying the above mentioned spatial and temporal discretization to the integral formulation of generalized balance equation 4.5 on the cell P results in an local algebraic equation:

$$a_P \phi_P^{n+1} + \sum_N a_N \phi_N^{n+1} = S_p. \tag{4.17}$$

A global algebraic equation system is established subsequently by assembling local algebraic equations for all CVs

$$[A][\phi] = [S], \tag{4.18}$$

where $[A]$ and $[S]$ depend on ϕ of previous time-level. Therefore, an initial value of $\phi = \phi^0$ is indispensable for the solution of this equation system. In the context of OpenFOAM, Eq. 4.18 can be solved by a direct or iterative method with various speedup techniques, a detailed description of these methods refer to [67, 73, 157]. This discretization procedure is valid for the general transport equations, thus, both the balance equations for fluid flow and the heat equation for the solid region, which represents a simplified energy balance equation, are discretized using the above mentioned discretization procedure.

4.2 Solution procedure

This section discusses the solution procedure for the turbulent incompressible Navier–Stokes–Fourier fluid flow with variable physical properties and conjugate heat transfer, for which the balance equations are formulated in Chap. 2. The continuity equation, momentum equation and energy equation (see Section 2.1) are solved for the fluid region, while the heat transfer in the solid region is governed by the heat equation (Eq. 2.17). The discretization procedure described above is applied to the complete solution domain and all PDEs to be solved. Rest of this section focuses mainly on the treatment of nonlinear convective term in momentum equation and pressure–velocity coupling in this PDE system as well as the interaction between fluid and solid regions.

According to the described discretization procedure in the above section, the momentum equation is expressed in a semi-discretized form as follows:

$$a_P \left(\widetilde{U}_i\right)_P = H_i - \left(\frac{\partial \overline{p}}{\partial x_i}\right)_P, \tag{4.19}$$

where a_P is the coefficient of $\left(\widetilde{U}_i\right)_P$ in the global algebraic equation system, H_i represents all contributions apart from the l.h.s. and the pressure gradient, e.g. source terms and contributions of neighbouring cells. In the framework of OpenFOAM, the pressure is solved from the Poisson equation, which is obtained by substituting the continuity equation into the momentum equation. The semi-discretized form of the Poisson pressure equation in OpenFOAM is given as follows:

$$\sum_f S_{fi} \cdot \left[\left(\rho a_P^{-1}\right)_f \left(\frac{\partial \overline{p}}{\partial x_i}\right)_f\right] = \frac{\partial \rho}{\partial t} + \sum_f S_{fi} \cdot \left(\rho a_P^{-1} H_i\right)_f. \tag{4.20}$$

The velocity is explicitly expressed as dependent on the pressure gradient:

$$\left(\widetilde{U}_i\right)_P = a_P^{-1} H_i + a_P^{-1} \left(\frac{\partial \overline{p}}{\partial x_i}\right)_P, \tag{4.21}$$

and the conservative face flux is given as:

$$F_f = S_{fi}\left[\cdot\left(\rho a_P^{-1} H_i\right)_f - \left(\rho a_P^{-1}\right)_f \left(\frac{\partial \overline{p}}{\partial x_i}\right)_f\right]. \tag{4.22}$$

The non-linear convective term is linearized and the associating operators, a_P and H_i, are computed based on velocity field obtained from previous iteration or initial condition. The pressure–velocity coupling is represented by linear dependence of velocity on pressure or vice-versa in Eq. 4.19 and Eq. 4.20. In the FVM framework of OpenFOAM, the pressure–velocity coupling is treated using a segregated approach, specifically the merged PISO-SIMPLE algorithm (see [71,133]). The energy equation for fluid region and the heat equation for solid region exchange the interaction on interface, e.g. temperature and heat flux, at each time-step. The energy equation for the fluid region and the heat equation for the solid region exchange the boundary conditions, such as temperature and heat flux, at each time-step.

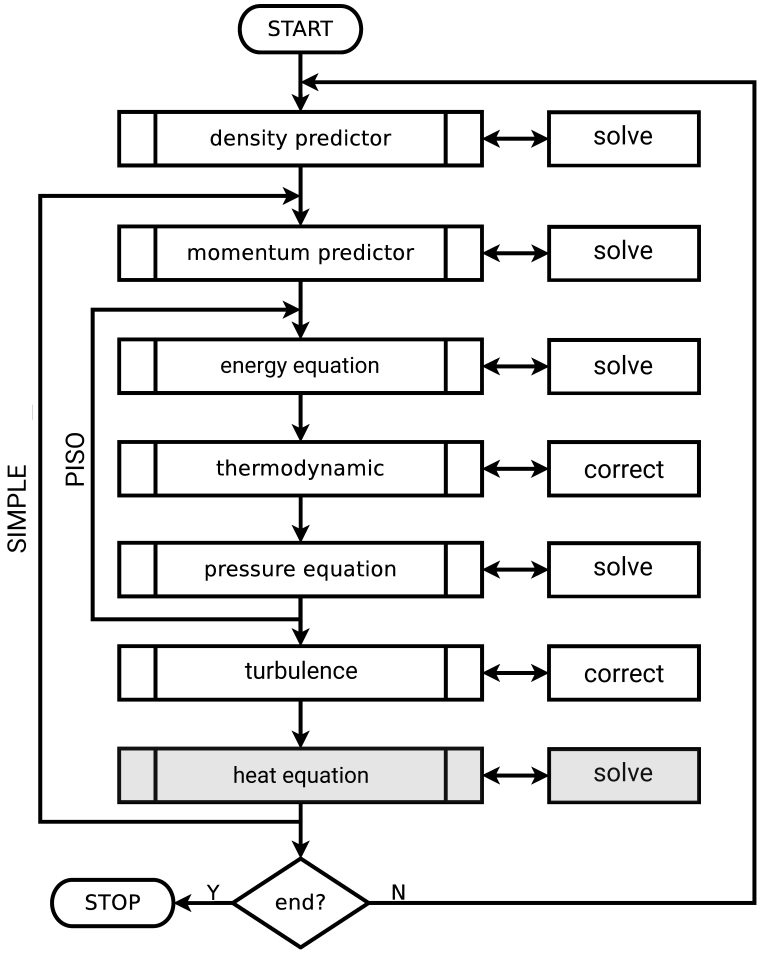

Figure 4.2: Flowchart of the solution procedure for turbulent flow with conjugate heat transfer (operations for solid regions are presented in gray).

The solution procedure for turbulent flow with conjugate heat transfer is schematically described in Fig. 4.2, in which the operations for solid regions are presented in gray, and summarized as follows:

1. Start the simulation with specified initial conditions for all fields in both fluid and solid regions.

2. Start the calculation for a new time-step, set up required field values based on values from previous time-step or initial conditions.

3. Solve the continuity equation and update the density field within the density predictor process.

4. Assemble and solve the discretized momentum equation, Eq. (4.19), using values from previous steps. Update velocity field, and refresh the operator H_i and mass flux with updated velocity field.

5. Assemble and solve enthalpy equation for fluid region using the mass flux from step 4 and the boundary values from solid regions. Update temperature field for fluid region according to the obtained enthalpy field.

6. Correct the thermodynamic and transport properties based on the temperature field obtained in step 5.

7. Assemble and solve the pressure equation, Eq. 4.20. Update the velocity field using Eq. 4.21 and the mass flux using Eq. 4.22. Repeat step 5 – step 7 (PISO-loop) until the tolerance for pressure–velocity system is reached.

8. Correct turbulent quantities.

9. Solve the energy equation in solid region with boundary values of fluid regions (obtained in step 5). Repeat step 4 – step 9 (SIMPLE-loop) until all solution tolerances are reached.

10. If the final time is not reached, goes to step 2. Otherwise, stop the simulation.

It is important to note that in the present work, a small time-step size and an iterative solution procedure (SIMPLE algorithm) are employed. This helps mitigate the lagging effect of non-linearity, and it is expected to have a negligible impact on the overall results, as reported in [73]. Furthermore, in the PISO-loop H_i and a_P keep their values, while the pressure gradient updated in each iteration, which means, the non-linear coupling is treated as less important than the pressure-velocity coupling. In addition, the interaction between the fluid region and the solid region is updated in the SIMPLE-loop, while within PISO-loop the temperature and heat flux on the interface are treated as constant.

Moreover, it is assumed in this work that the velocity in the computational domain is smaller than $0.3Ma$, where Ma represents the Mach number. While, physical properties of the flow, such as density, can vary significantly depending on the local temperature. That aligns with the low-Mach theory, and as a result, a low-Mach theory-based solver has been implemented within the OpenFOAM framework for conducting the simulations in the present work. Thereby, it allows an accurate prediction of turbulent heat and fluid flow with strongly variable physical properties. Noting that, wave transmissive boundary conditions are not necessary for the low- Mach approach, which on one side improves the numerical stability, on the other side reduces the complexity of the simulation [150].

4.3 Near-wall treatment

The algebraic equation system, given by Eq. 4.18, is modified to account for the specific boundary conditions imposed on the system. These boundary conditions can be expressed mathematically using different approaches such as Dirichlet conditions, Neumann conditions, periodic boundary conditions, or a combination of these. In the present work, particular emphasis is placed on the near-wall treatment, where a combination of Dirichlet conditions (e.g., no-slip velocity) and Neumann conditions (e.g., constant heat flux) are typically employed. The coefficient matrix $[A]$ in Eq. 4.18 is adjusted to incorporate the specific boundary conditions used in the simulation. A detailed description of this modification can be found in references such as [150] and [73]. The standard treatment of wall boundary conditions is applicable when the heat and fluid flow near the wall are resolved, such as in the case of WRLES or IDDES. However, when using a wall-modeled approach with a wall-shear stress model, such as employing a wall function or a two-layer model, an additional procedure is needed to modify the turbulent quantities. This auxiliary procedure is specific to WFLES and involves adjustments to the turbulent quantities according to the chosen wall model. The detailed steps of the auxiliary procedure for WFLES are summarized below.

At first, in order to clarify the nomenclature used, figure 4.3 depicts a control volume that comprises a part of a solid wall boundary b. Thereby, P is the cell centroid, y the nearest distance from P to the wall, $\overrightarrow{\eta}$ the wall normal direction and $\overrightarrow{\zeta}$ the flow direction.

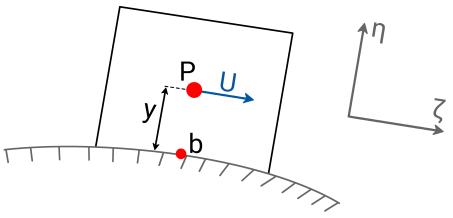

Figure 4.3: Control volume that comprises a part of a solid boundary. b: solid boundary, P: cell centroid, y wall distance, η: wall normal direction, ζ: flow direction, U: velocity component in flow direction.

The flow direction $\overrightarrow{\zeta}$ is calculated using the velocity vector at the cell centroid P as

$$\overrightarrow{\zeta} = \frac{\overrightarrow{U} - |\overrightarrow{U}|\overrightarrow{\eta}}{\left|\overrightarrow{U} - |\overrightarrow{U}|\overrightarrow{\eta}\right|}, \tag{4.23}$$

where the wall normal direction $\overrightarrow{\eta}$ is directly available form the numerical grid. Then, the velocity vector $\overrightarrow{U}$ is divided into a component in flow direction $U = \left|\overrightarrow{U} \cdot \overrightarrow{\zeta}\right|$ and a component in wall normal direction $V = \left|\overrightarrow{U} \cdot \overrightarrow{\eta}\right|$. By means of this, the coefficient C_U at the cell centroid P can be calculated as

$$C_U = \left[\frac{1}{2}\left(\frac{\partial \rho U}{\partial t} + \frac{\partial}{\partial \zeta}\left(\rho U U\right) + \frac{\partial}{\partial \eta}\left(\rho V U\right)\right) + \frac{\partial p}{\partial \zeta} + \rho f_\zeta\right]_P, \tag{4.24}$$

where the divergence and the pressure gradient terms are approximated using interpolated values from the neighbor cells, while the temporal term is approximated using a first order Euler scheme. It is worth mentioning that all quantities in the r.h.s of Eq. 4.24 are solved

from the main solution procedure, thus C_U is directly computed numerically from known values.

Next, the friction velocity u_τ is computed using the proposed non-equilibrium wall function formulation (see equation 3.33). Because of the dependencies in equation 3.33, an iterative procedure (e.g. Newton-Raphson or regula falsi methods) is required to determine u_τ by finding the root of

$$F = \frac{U}{u_\tau} - f(y, C_U, u_\tau) = 0, \tag{4.25}$$

where f is the r.h.s of Eq. 3.33. Thereby, results from the previous time step are used to initialize the iterative procedure. Notice that it is possible under some circumstances that no root can be found for equation 4.25. In such cases C_U is set to zero and the equilibrium value for u_τ is used.

Finally, u_τ is utilized to calculate the turbulent viscosity as

$$\mu_t = max\left(\rho u_\tau^2 \frac{y}{U} - \mu, 0\right), \tag{4.26}$$

which is applied as boundary condition for the sub-grid scale viscosity μ_{sgs} at the boundary face b. The numerical procedure is computed for each off-wall control volume and for each time step.

In WF-LES with velocity wall function, wall functions are applied to evaluate the wall shear stress, and determinate the boundary value for the subgrid-scale viscosity μ_{sgs}, namely specify a Dirichlet boundary for μ_{sgs} at the wall. Thus, in the implementation μ_{sgs} at the wall is modified accordingly, while other fields, like velocity or pressure, are not corrected explicitly. As a consequence of using a wall function approach, the velocity values at the first off-wall cell centers may be less accurate. Whereas, the wall shear stress, which is modeled by the wall function, can still provide reasonable agreement with reference values. Similarly, the heat flux or temperature on the wall can be computed using the temperature wall function, then the α_{sgs} or T at the wall are modified according to the desired heat flux or temperature.

Chapter 5

Evaluation of the novel WFLES approach

In this chapter, the proposed wall function approach for wall-modeled LES is evaluated for heat and fluid flow phenomena that can be found in several technical energy systems, in particular ICE or EGAS. The selected test cases consist of: (a) turbulent jet impinging on a 45°-inclined heated plate, (b) turbulent conjugate heat transfer in a channel, (c) turbulent pulsating heated channel flow, (d) heat and fluid flow in a industrial three way catalytic converter, (e) strongly heated air flow in a tube and (f) turbulent backward-facing step flow with heated walls. The relevant illustration of the selected test cases and the locations where such heat and fluid flow situations are prevalent in an EGAS are shown in Fig. 5.1. The relevant short description of each test case and the LES results obtained with the noval and classical wall functions are provided in the following sections with a special focus on a comparison of heat and fluid flow quantities relevant for industrial/engineering applications. Notice that most of the test cases and analysis were already published by the author in [104, 105], except the heat and fluid flow in a realistic three way catalytic converter test case.

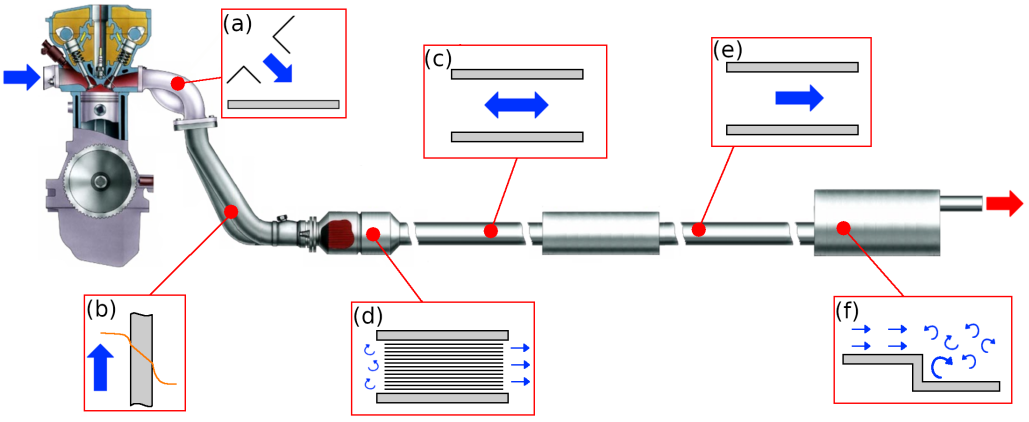

Figure 5.1: Illustration of an ICE with EGAS. Representation of characteristic fluid flow and heat transfer situations (pulsating heated boundary layer flow (c, Sec. 5.1), impingement cooling/heating (a, Sec. 5.2), recirculation/reattachment flow (f, Sec. 5.3), turbulent conjugated heat transfer (b, Sec. 5.4), strongly heated boundary layer flow (e, Sec. 5.5), heat and fluid flow in monolithic catalytic converter(d, Sec. 5.6)).

5.1 Turbulent pulsating flow

In ICE, the fluid flows are essentially driven by the reciprocating motion of the piston, which is in turn responsible for the pulsating heat and fluid flow in the subsequent EGAS. Thereby, heat and momentum transport phenomena are strongly interlinked with each other and usually vary periodically in time. In order to demonstrate the benefits of the proposed wall function approach under such time-dependent operating conditions, a pulsating heated channel flow at $Re_\tau = 350$ and $Pr = 0.71$ with heated/cooled walls is studied as first benchmark test case. The computational domain employed is depicted in Fig. 5.2, where δ denotes half the height of the channel and $N_{1,2,3}$ are the numbers of grid points in $x-$, $y-$ and $z-$ directions. For comparison of the fluid flow properties, the isothermal DNS data of Scotti and Piomelli [160] are utilized. Additionally, a non-isothermal WRLES was carried out in order to first compare predicted thermal characteristics with DNS and then to generate data which are not available in the DNS study of Scotti [160].

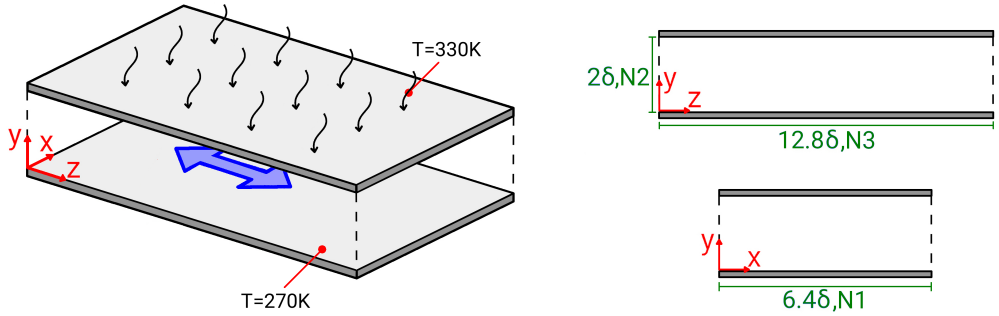

Figure 5.2: Computational domain for the LES study of the pulsating heated channel flow at $Re_\tau = 350$ and $Pr = 0.71$. N1, N2, N3 represent the number of grid points in $x-$, $y-$, and $z-$direction. δ represents half height of the channel.

Following the procedure described in [160], the flow is driven by a time varying external pressure field given as

$$P(z,t) = \Delta P_0 \left(1 + 200 sin\left(\frac{u_\tau^2 \omega^+}{\nu} t\right)\right) \frac{z}{L_z}, \tag{5.1}$$

where $\Delta P_0 = u_\tau^2 L_z/\delta$, $\omega^+ = \omega\nu/u_\tau^2 = 0.04$, $L_z = 12.8\delta$ and z is the stream-wise direction. For the non-isothermal simulations, the upper channel wall is heated up by a constant temperature of $T_w = 330K$, while the lower wall is cooled with a wall temperature of $T_w = 270K$. This leads to a mixed mean temperature of $T = 300K$ of the fluid. The numerical grid of the WRLES consists of $(N_1 \times N_2 \times N_3) = (192 \times 96 \times 192) = 3,538,944$ control volumes and has a non-dimensional maximal wall distance of $y^+_{max} = 0.5$. The numerical grid applied in the WFLES study consists of $(N_1 \times N_2 \times N_3) = (144 \times 48 \times 144) = 995,328$ control volumes with a non-dimensional maximal wall distance of $y^+_{max} = 14$. Notice that the control volumes are evenly distributed along the wall-normal direction with $\Delta y^+ = 28$.

Fig. 5.3 (a) presents LES predictions of the phase-averaged skin friction coefficient $C_f = 2\tau_w/(\rho U_b^2)$ as a function of phase angle ωt. Here, τ_w is the wall shear stress and U_b the bulk velocity. The phase-averaged Nusselt number $Nu = |q_w|\delta/(\alpha(T_w - T_\delta))$ is depicted in Fig. 5.3 (b), where T_w is the wall temperature, T_δ the temperature at $y = \delta$ and q_w the wall heat flux which is defined as $q_w = (\alpha + \alpha_T)[\partial T/\partial y]_{y=0}$. Note that the Nu-number are not available from DNS. All results are phase-averaged over 50 cycles and

additionally spatially averaged over both walls for each phase angle. In both figures, LES results of the proposed non-equilibrium wall function, the generalized formulation of Shih et al. [163], the unified wall function of Spalding [172] and the formulation of Kader [77] are presented and compared.

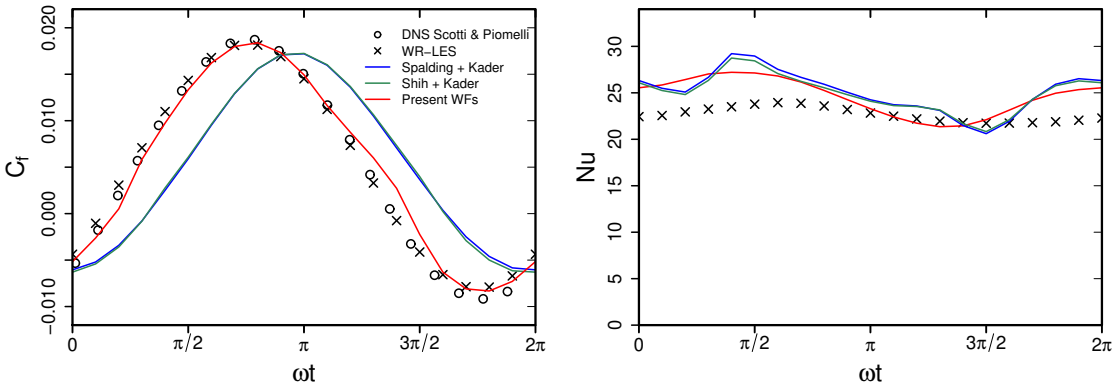

(a) (b)

Figure 5.3: Phase-averaged skin friction coefficient (a), and Nusselt number as a function of phase angle ωt (b). Comparison of different wall function formulations with DNS data of Scotti and Piomelli [160] (a) and results of a non-isothermal WRLES (b).

The comparison of the obtained skin friction coefficient C_f for the applied various wall function approaches is shown in Fig. 5.3 (a), it appears that peak values predicted by conventional wall function formulations are out-of-phase. In contrast, only the proposed non-equilibrium wall function approach is able to predict the peak value of C_f and it phase correctly. This can be attributed to the transient effects that are included into the new formulation. In terms of Nu as it is depicted in Fig. 5.3 (b), all wall function formulations slightly overestimate the Nusselt number. Nevertheless, it can be clearly seen in Fig. 5.3 (a) and (b) that predictions of the proposed wall function formulation agree well with the reference data and are significantly better than existing wall functions from the literature. This holds true for both fluid flow and thermal properties in such a flow that exhibits clearly non-equilibrium effects.

5.2 Impingement heat transfer

The second test case deals with a turbulent square jet flow that impinges on a 45°-inclined solid surface. It mimics several canonical mixing and fluid flow situations that is also relevant to ICE and EGAS, including thermo-viscous boundary layer flows, impinging cooling/heating and wall-jets. A schematic of the test case investigated in the LES study is provided in Fig. 5.4. The heat transport and fluid flow within this configuration were investigated numerically in [153] by using a WRLES technique which is taken as a reference. Furthermore, experimental and DNS studies of this configuration at a lower Reynolds number and different inclination angles were provided by the author with co-authors in [151, 154].

In this test configuration, a turbulent jet of dry air ($T_{in} = 290K$, $p = 1atm$) emanates from a square nozzle ($D = 40mm$) and impinges on a heated flat plate. The heated wall has a constant wall temperature of $T_w = 330K$, a jet-to-plate spacing of $H/D = 1$ and an inclination angle of $\alpha = 45°$. The Reynolds number of the flow based on the bulk velocity

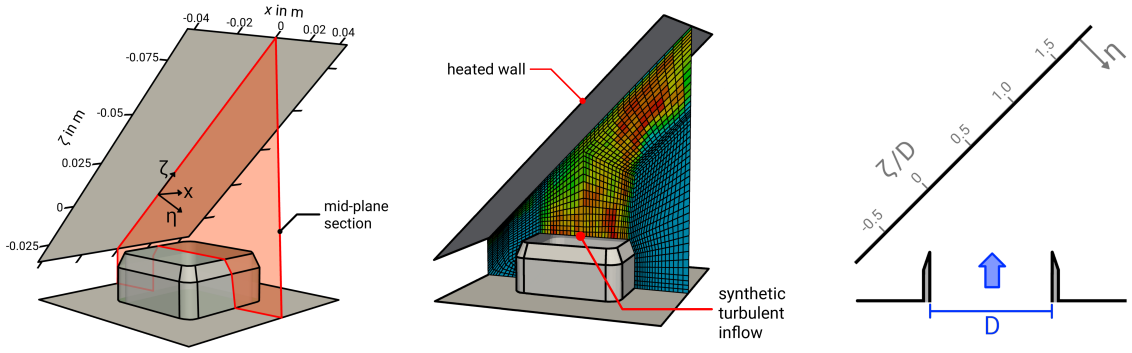

Figure 5.4: Computational domain, mid-plane section, and description of the impinging jet configuration, [153].

and nozzle diameter is $Re_b = 20,000$.

The numerical grid used in the present LES study consists of 809,206 control volumes and has a dimensionless wall distance of $y^+ \approx 10$. Thereby, the first four near-wall cells are evenly distributed in wall-normal direction with $\Delta y^+ \approx 20$. The amount of control volumes applied is significantly lower compared to the 4.8 million control volumes applied in the reference WRLES [153]. In accordance with the WRLES, the axial velocity at the inlet is set to the bulk velocity and synthetic velocity fluctuations are superimposed based on the digital filter approach proposed by Klein et al. [89]. The temperature at the inflow is set to a constant value of $T_{in} = 290K$. At the outlet, zero Neumann condition is used for the temperature and an inlet/outlet condition for the velocity. At the walls, no-slip boundary condition is specified for the velocity and the zero Neumann condition for the temperature, except at the heated wall where the temperature is set to a constant value of $T_w = 330K$.

Fig. 5.5 presents the distribution of (a) the wall shear stress and (b) the local Nusselt number along the ζ-axis at $x = \eta = 0$ in comparison with the results of the WRLES [153]. Thereby, the local Nusselt number is defined as $Nu = h_t D/\alpha$, where h_t denotes the local heat transfer coefficient and α the thermal conductivity of the fluid. The WMLES results were achieved by using the proposed unified wall function, the generalized formulation of Shih et al. [163], the unified wall function of Spalding [172] and the formulation of Kader [77].

It can be seen in Fig. 5.5 that values of τ_w and Nu are high at $\zeta/D = -0.15$ and decrease rapidly away from this location. Moreover, it was observed in [153] that the flow direction changes suddenly at $\zeta/D = -0.15$ and that the fluid is subject to a strong acceleration in wall-parallel direction in this region. Both, sudden change of the flow direction and fluid acceleration induces significant non-equilibrium contributions in the boundary layer flow. In this context it is clearly visible that the generalized formulation of Shih et al. [163] and in particular the novel non-equilibrium LES wall function approach are able to reproduce this physical behavior correctly, while LES results obtained by means of the unified wall function of Spalding [172] and that of Kader [77] significantly underestimate the peak value of τ_w and overestimate the maximum of Nu. Far away from $\zeta/D = -0.15$, results of all wall function formulations are quite similar, which suggests that non-equilibrium effects are negligible in this region.

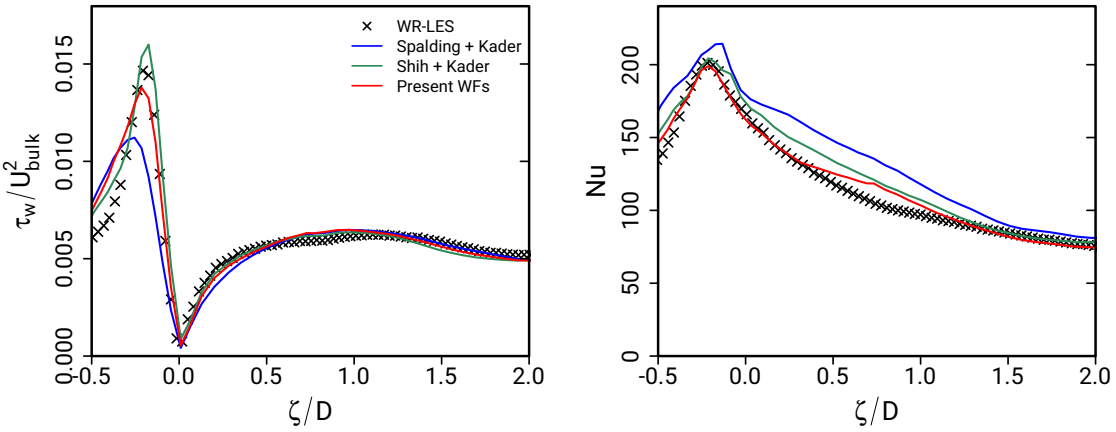

(a) (b)

Figure 5.5: LES results of local wall shear stress (a) and Nusselt number (b) along the wall-parallel direction. Comparison of the proposed wall function with reference WRLES [153] and other classical wall function approaches [77, 163, 172].

5.3 Recirculating flow with heat transfer

The next benchmark test case consists of a backward-facing step flow with a constant heated surface behind a sudden expansion. This test case features several complex flow situations such as recirculation and flow separation that are relevant to ICEs and EGAS. The backward-facing step flow with heated walls was investigated experimentally by Vogel and Eaton [189]. Numerical studies based on WRLES technique can be found in e.g. [87, 97, 204]. A representation of the computational domain for the present LES study is depicted in Fig. 5.6.

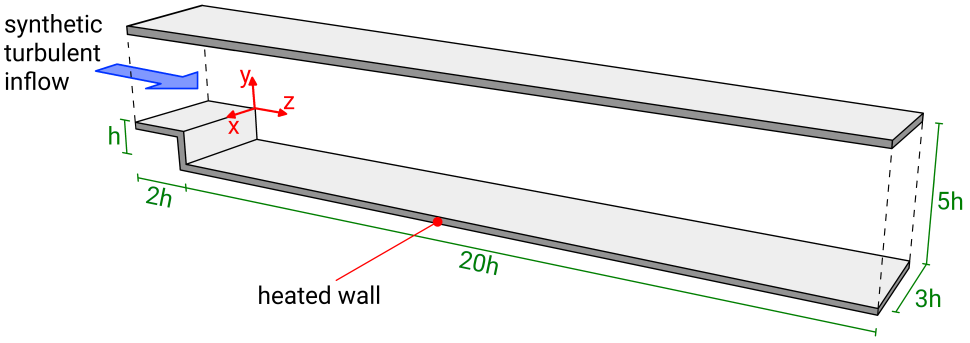

Figure 5.6: Computational domain of the backward-facing step flow with heated walls including the dimensions and boundary conditions.

In the test case, a turbulent stream of dry air ($T = 298K$, $Pr = 0.71$) flows through a wind tunnel, expands suddenly after $2h$ and is subsequently heated up at the lower wall behind the expansion with a constant heat flux of $q_w = 270W/m^2$. The backward-facing step flow investigated in this study has a channel expansion ratio of 1.25 and a Reynolds number of $Re = 28,000$ (based on the free-stream velocity and step height h).

The numerical grid applied consists of 1,804,800 control volumes and has a non-dimensionless wall distance of $y^+ \approx 10$. Thereby, the grid is evenly distributed in wall-normal direction at the heated wall up to $y^+ \approx 100$ with $\Delta y^+ \sim 20$. Regarding the inflow,

a realistic inflow turbulence is generated using the digital filter approach proposed by Klein et al. [89]. The fluctuations are superimposed on a mean boundary layer flow profile with a boundary layer thickness of $\delta_{99} = 1.07h$.

Fig. 5.7 depicts the distributions of (a) the skin friction coefficient $C_f = \tau_w/(0.5\rho U_\infty)$ and (b) the Stanton number $St = q_w/(U_\infty \rho c_p(T - T_w))$ along the axial direction at the heated lower wall behind the expansion. Here, U_∞ is the free-stream velocity, c_p the specific heat capacity of the fluid, ρ the fluid density, τ_w the wall shear stress and T_w the wall temperature. For comparison purpose, results of a WRLES with a finer grid resolution of 4,378,272 control volumes are also presented (denoted here as WR-LES).

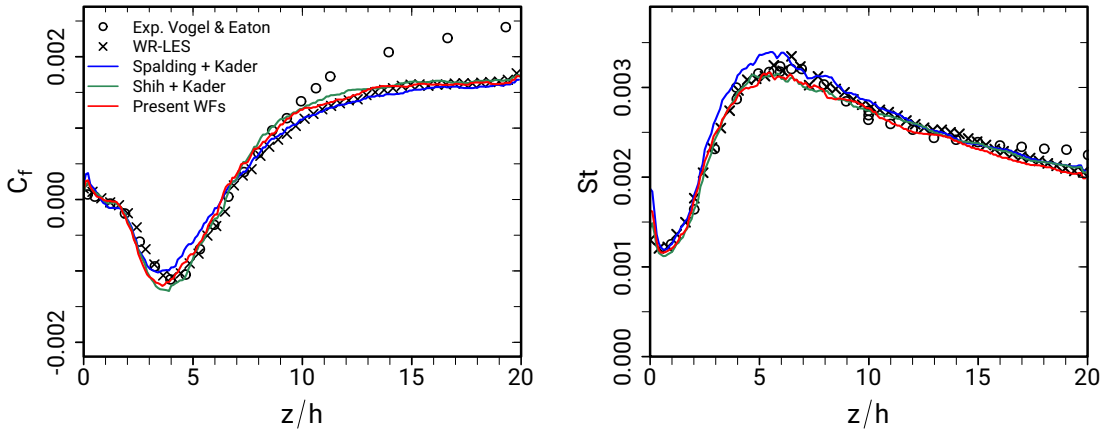

(a) (b)

Figure 5.7: Skin friction coefficient C_f (a) and Stanton number St (b) at the heated wall as a function of axial position.

As it can be observed in Fig. 5.7. there is excellent agreement between the WMLES predictions and the WRLES results and also reasonably good agreement with the experimental data. This holds true for both, C_f and Nu. Furthermore, it is visible that LES results obtained by using the different wall function formulations are very close to each other. This suggests that non-equilibrium effects play a minor role in this test case, at least for the selected numerical setup and for predictions of C_f and Nu.

5.4 Turbulent conjugate heat transfer

Most practical energy systems are bounded by solid walls, e.g. ICEs, EGAS, gas turbines, etc.. Thereby, the fluid region is coupled thermally with the solid region. This places particular demands on the LES approach especially on the wall function. To further evaluate the approach of WFLES, a turbulent heated channel flow case with conjugate heat transfer, in line with the numerical study of Flageul et al. [53], was selected. For this purpose, these regions (solid, fluid and fluid–solid interface) are considered as depicited in Fig. 5.8. The heated channel flow was simulated for a fluid with a molecular Prandtl number of $Pr = \nu/\alpha^f = 0.71$ and at $\mathrm{Re}_\tau = 1020$. A fluid-to-solid thermal diffusivity ratio of $G_1 = \alpha^f/\alpha^s = 1$ and a solid-to-fluid thermal conductivity ratio of $G_2 = \lambda^s/\lambda^f = 1$ were selected, leading to a thermal activity ratio of $K = 1/G_2\sqrt{G_1} = 1$ [53]. These values of $G_1 = G_2 = K = 1$ were selected in accordance with the reference DNS of [53] and represent the case of a coupled scalar with the same thermal properties in the fluid and solid region. A sketch of the computational domain used for this simulations is shown

in Fig. 5.8, where x, y and z are the span-wise, wall-normal and stream-wise directions, respectively.

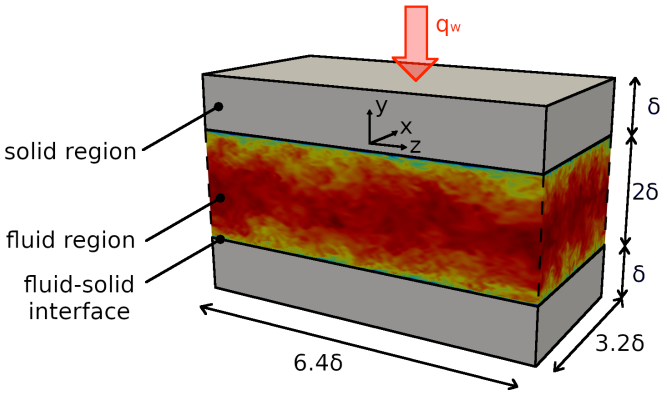

Figure 5.8: Channel flow configuration with conjugate heat transfer. Solid domains on top and bottom. Fluid region is located in the middle coupled via an interface with the solid domains.

The entire computational domain has a dimension of $L \times W \times H = 6.4\delta \times 3.2\delta \times 4\delta$, where δ is the channel half-height. Thereby, similar to [53], the fluid domain is bounded at $-\delta < y < \delta$ and the solid domains are located at $y > \delta$ and $y < -\delta$, respectively. Both solid domains have an height of δ, which ensures that the boundary condition used at the outer wall has no significant impact on the statistics at the fluid–solid interface [53]. Periodic boundary conditions were applied to the velocity and temperature in stream-wise and span-wise directions. At the solid surface, a no-slip condition was employed for the velocity and a coupled thermal boundary condition was used for the temperature (see Eq. (2.18)). The pressure and temperature gradients that drive the heat and fluid flow in the fluid region are adjusted dynamically to maintain a constant mass flux and mean mixed temperature. Therefore, the pressure and temperature were split into a periodic and a non-periodic part. Source terms for the non-periodic part, $\overline{f}_x^U$ and $\overline{f}^{T_f}$, were added to the momentum and temperature equation, respectively (see [85]). The fully developed turbulent channel flow was achieved before sampling started (see [151]).

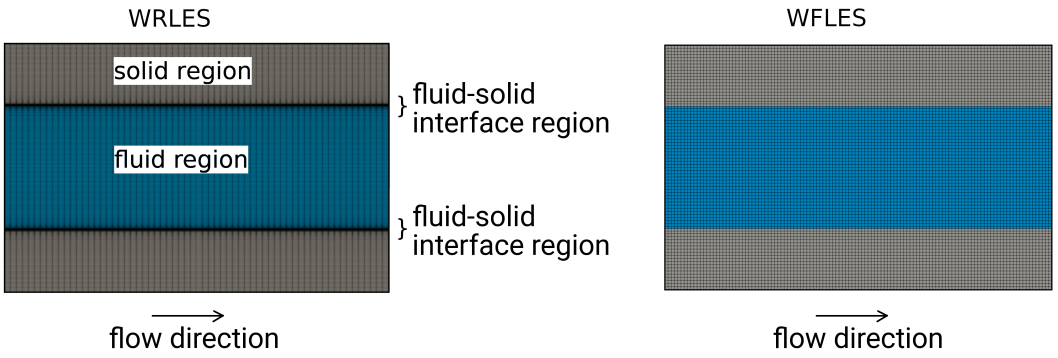

(a) (b)

Figure 5.9: Numerical grids used in the (a) WRLES, (b) WFLES approaches.

Three-dimensional block-structure numerical grids with different spatial resolutions were employed. In the case of WRLES, the numerical grid was refined towards the wall in order to ensure a non-dimensional wall distance y_w^+ smaller than one. A representation of both (coarsest) grids used for the WRLES and WFLES is shown in Fig. 5.9.

The balance equations for turbulent flow with conjugate heat transfer (see Chap. 2) were solved numerically using an incompressible version of *chtMultiRegionFoam* from the open-source software OpenFOAM v1912 [60]. Thereby, the temperature transport equation, the LES near-wall modeling approaches and the source terms that drive the channel flow were added to the source code. The simulations were carried out with second order numerical schemes and with CFL-numbers smaller than one.

Fig. 5.10 presents predictions of instantaneous velocity and temperature fields in the channel flow configuration obtained by using (a) WRLES and (b) WFLES. Note that the temperature color scale is subdivided into a range for the fluid region and the solid region in order to better visualize the wide range of temperature scales. It shows clearly in Fig. 5.10 that the velocity and temperature fields are highly turbulent in the fluid region with steep velocity/temperature gradients close to the wall. Thereby, due to the finer grid resolution, more of the small-scale turbulent structures are resolved in the WRLES than in case of WFLES. In contrast, the temperature field in the solid region is homogeneous distributed with a steep gradient in the wall-normal direction. Moreover, it appears that the predicted temperature fields obtained by the different wall-modeled approach are quite similar and compare well with the WRLES.

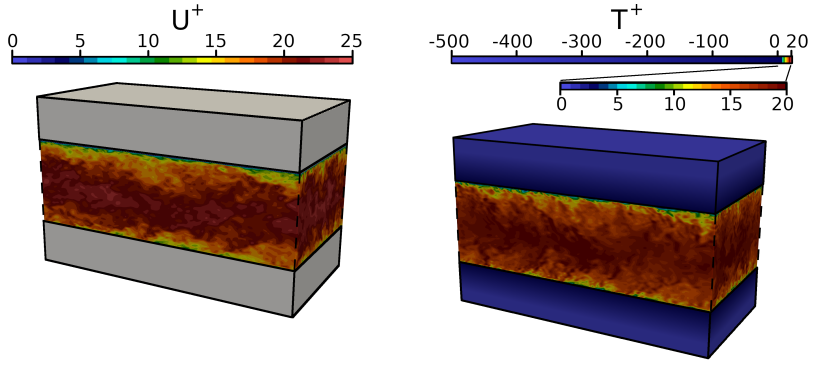

(a) WRLES

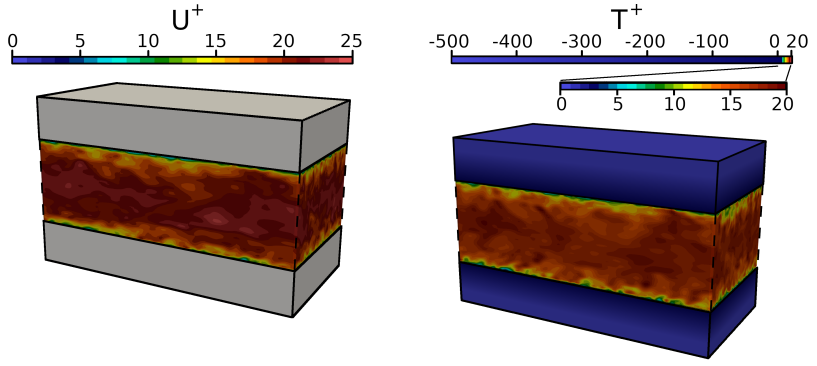

(b) WFLES

Figure 5.10: Snapshots of the instantaneous velocity field (left) and temperature field (right) predicted by means of (a) WRLES and (b) WFLES.

Predicted mean temperature Θ^+ and rms temperature Θ^+_{rms} profiles in the solid and fluid regions are compared with WRLES in Fig. 5.11. As obvious in Fig. 5.11, predictions of Θ^+ obtained by the wall-modeled LES approach agrees very well with the reference WRLES. This holds true for the interface as well as for the rest of the solid region. Similarly, profiles of Θ^+_{rms} is reproduced well by the wall-modeled LES.

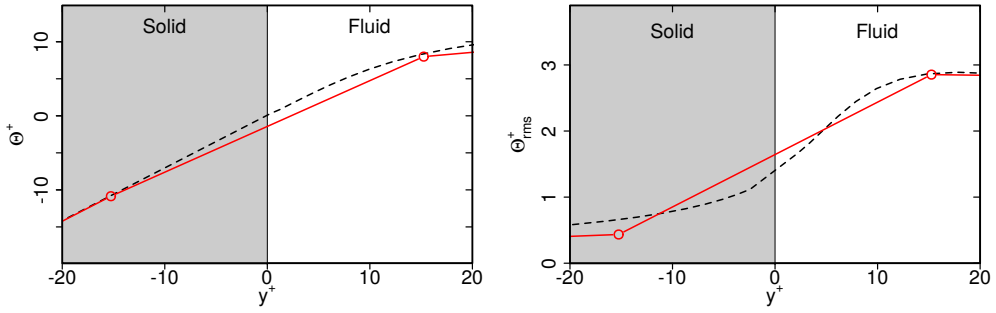

Figure 5.11: Dimensionless mean and rms temperature Θ^+, Θ_{rms} as a function of non-dimensional wall distance y^+ for $\mathrm{Re}_\tau = 1020$. Comparison of wall-modeled LES with WRLES. —: WFLES; - -: WRLES.

Thus, by examining predictions of heat and fluid flow statistics within the turbulent channel flow configuration with conjugate heat transfer, it turned out that WFLES is able to reproduce the physics of such heated flows properly, while requiring rarely around 1% computational cost consumed by WRLES [105].

5.5 Strongly heated wall-bounded flow

In numerous energy systems, like ICE and EGAS, large temperature differences are very common. This leads to strongly varying physical properties of the fluid. In order to analyze the performance of the different wall function formulations under such operating conditions, LES of a strongly heated air flow in a pipe with constant heat flux were carried out. Thereby, results obtained by means of the proposed non-equilibrium wall function, the generalized formulation of Shih et al. [163], the unified wall function of Spalding [172] and the formulation of Kader [77] are compared with measurements of Shehata and McEligot [162], DNS data of Bae et al. [10] and DNS data of Ries [150]. An illustration of the benchmark test case is depicted in Fig. 5.12. This configuration was also investigated by means of WRLES technique in e.g. [68, 198].

In this test case, dry air ($T_0 = 298.15K$, $p = 1atm$) flows through a DN-25 pipe ($D = 0.0272m$, $L = 30D$) and is heated up after an entrance length of $5D$. The heated pipe wall region has a length of $25D$ with a constant wall heat flux of $q_w = 4.11kW/m^2$ and the flow has a bulk Reynolds number of Re=6,000. In line with the reference DNS [10,150], air is treated as an ideal gas in the LES and all thermo-physical properties are obtained by power laws as a function of local temperature. In the present evaluation study, two different operation conditions were analyzed. At first, a forced convection test case without the gravitational force term in the momentum equation was simulated and secondly, a mixed convection test case including the gravitational force was carried out. In the latter test case, buoyancy effects on the turbulence are significant which leads to a laminarization of the turbulent flow.

The numerical grid used for the WFLES consists of 212,800 control volumes and has a non-dimensionless wall distance of $y^+ \approx 10$. Thereby, the numerical grid is evenly

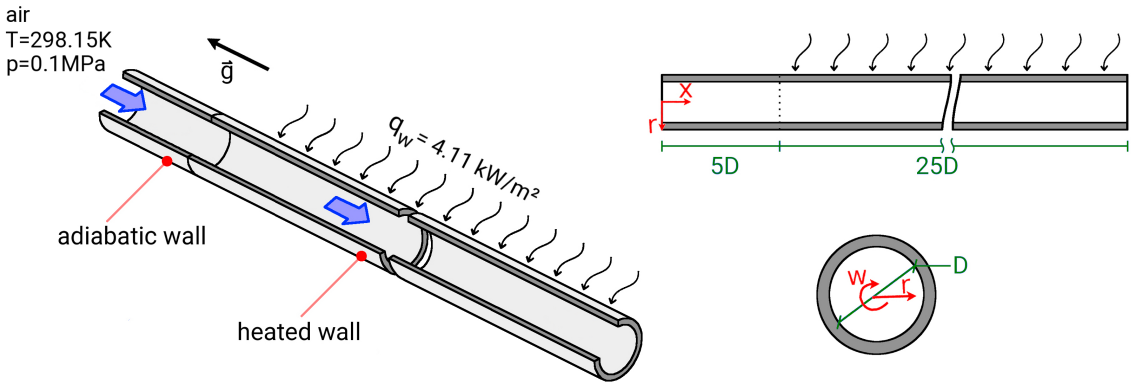

Figure 5.12: Illustration of the heated pipe flow domain. Isometric view (left); view along x-axis (top right); view along r-axis (down right).

distributed along the pipe radius with $\Delta y^+ \sim 20$. Regarding the boundary conditions, a no-slip condition is set for the velocity and a zero Neumann condition for the pressure at the pipe wall. At the heated wall, a constant wall heat flux of $q_w = \frac{\lambda}{c_p}\frac{\delta h}{\delta r}\Big|_{r=R} = 4.11 kW/m^2$ is imposed, while a zero temperature gradient condition is used at the adiabatic wall. In order to obtain a fully developed turbulent flow, the velocity field is extracted for each time step at the $x = 5D$ plane downstream of the inlet and used to prescribe the velocity field at the inflow plane. At the pipe outlet, a convective boundary condition is applied for the velocity in order to maintain the overall mass conservation, while the pressure is fixed to a constant value.

Fig. 5.13 provides predicted local skin friction coefficients C_f (a) and Nusselt numbers Nu (b) as a function of axial distance, where heating begins at an axial position of $x/D = 5$. LES predictions of the proposed non-equilibrium wall function, the generalized formulation of Shih et al. [163], the unified wall function of Spalding [172] and the formulation of Kader [77] are presented for both, the forced convection (top) and mixed convection (bottom) test cases.

By examining Fig. 5.13, it appears that LES results of all wall function approaches are reasonable close to the experimental data [162] and also to the reference DNS [10]. This holds true for both, the forced and mixed convection test cases. However, it is interesting to observe that some discrepancies in C_f and Nu are visible for $x/D > 15$ in case of mixed convection conditions. Thereby, values of C_f and Nu are slightly overestimated by all wall functions under consideration which might be attributed to laminar flow resulting from laminarization process due to strong buoyancy effects.

Next, the performance of the different wall function formulations to predict turbulent quantities under such extreme operating conditions are analyzed. For this purpose, Fig. 5.14 presents profiles of the resolved turbulent kinetic energy (a) and root mean square temperature (b) at different axial positions. For comparison the DNS data-set of [150] is utilized. Here, only results of the mixed convection test case are shown since laminarization effects on the turbulence are more significant under such operating conditions. One can observe in Fig. 5.14 (a) that the turbulent kinetic energy decreases with increasing x/D while the flow is effectively laminarized. Thereby, peak values of turbulent kinetic energy becomes slightly shifted away from the wall. In contrast, temperature fluctuations increase in flow direction and peak values enlarge (see Fig. 5.14 (b)). Both characteristic trends are captured reasonably by means of the WMLES. However, predictions become less accurate with increasing x/D, which might be attributed to laminar flow resulting from

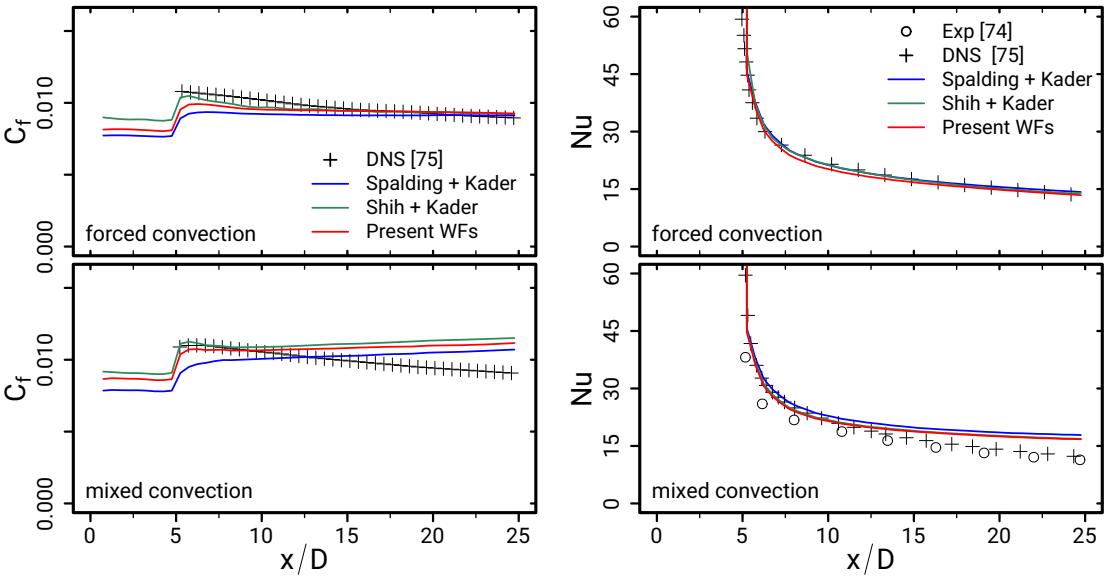

(a) (b)

Figure 5.13: Predicted values of skin friction coefficient (a) and Nusselt number (b) as a function of axial distance. Comparison of LES predictions using different wall functions with DNS [10] and experiment [162] for forced (top) and mixed (bottom) convection conditions.

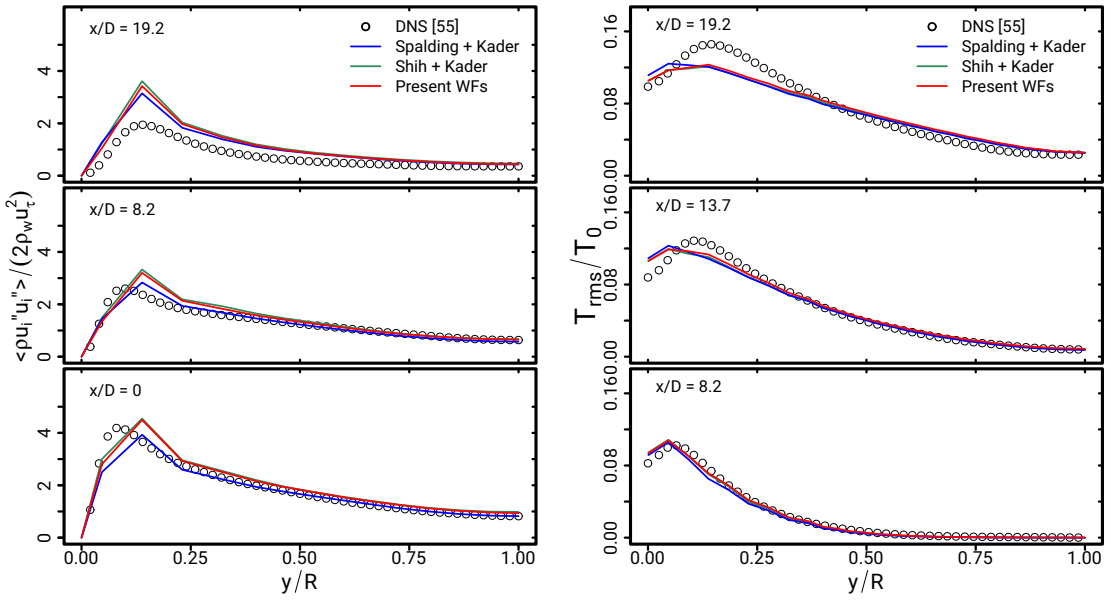

(a) (b)

Figure 5.14: Comparison of resolved turbulent kinetic energy (a) and root mean square temperature (b) profiles with DNS at different axial positions. Symbols denote DNS data of [150].

laminarization processes. Nevertheless, the overall effects of strong heating on turbulence is well reproduced by all wall functions under consideration that confirms the applicability

of the LES wall function approach for such strongly heated transitional air flows.

5.6 Heat and fluid flow processes inside a catalytic converter

In modern automobile with ICE, the EGAS plays a crucial role, in which the necessary chemical reaction occurs to convert or reduce the harmful exhaust gases into less-toxic pollutants, thus helping vehicles meet the prescribed emission norms. A modern catalytic converter consists of ceramic or metal monoliths, which have honeycomb structures with channel densities of 64–124 cells/cm^2, and the catalytic substance is distributed on the channel surface in porous form [41]. In the context of numerical simulation, the honeycomb structures can be either fully-resolved by means of numerical grids with fine resolutions or treated as a porous medium and modeled by a so-called Volume-Averaged Navier-Stokes (VANS) method. The first approach is computationally extremely expensive, while the latter one allows accurate predictions of the main heat and fluid flow features in a reasonable amount of computational time. Despite of the extremely high computational cost, a fully-resolved numerical simulation of the heat and fluid flow inside the monolith was carried out by the author (see [103]), which together with the measured pressure drop over the catalytic converter under different operating conditions provides reliable reference data to evaluate the application of WFLES/VANS on the study of heat and fluid flow in the catalyst.

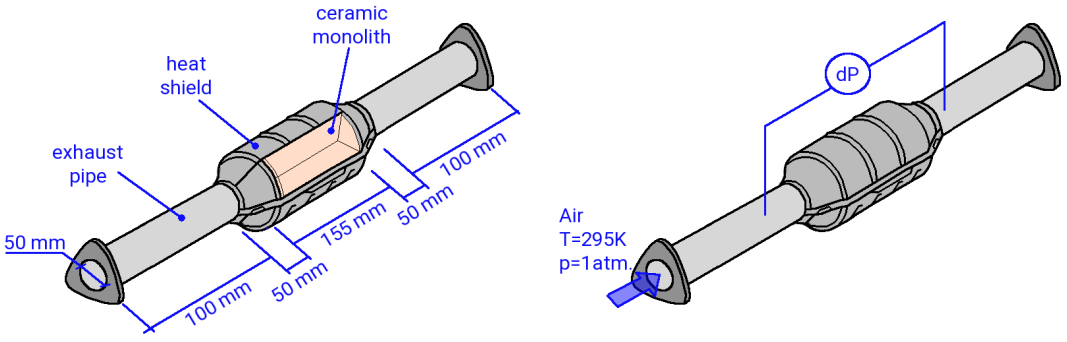

(a) (b)

Figure 5.15: Illustration of the catalytic converter. (a) assembly and dimensions; (b) measurement setup.

In this case, an industrial three way catalyst of a Lada Niva 21214 vehicle is selected as the research objective. The core of the catalytic converter consists of a ceramic monolith, which has a honeycomb structure with 12,468 small ducts. Each duct has a dimension of $0.7mm \times 0.7mm \times 155mm$. Notice that an unwashed catalytic converter was used in the present study. An illustration of the catalytic converter with assembly and dimensions is depicted in Fig. 5.15.

The pressure drop of the catalyst is determined by experiment (test rig see Fig 5.15 (b)) under non-reacting iso-thermal conditions, in which dry air ($T = 295K$, $p = 1atm$) flows through the catalytic converter and the pressure drop over the monolith is measured by using a differential pressure sensor (differential pressure transmitters PD-23 of Keller AG) at constant volumetric flow rates of $10.4m^3/h$ to $139.6m^3/h$. The bulk of the flow is provided separately and measured by a thermal mass flow meter (Bronkhorst IN-FLOW F-116AI). Notice that there is a perforated plate located upstream of the monolith, positioned at a distance of ten pipe diameters from it, which serves as a turbulence-generating grid

and ensures that the turbulent flow is fully developed at the entrance of the catalytic converter (see [150]).

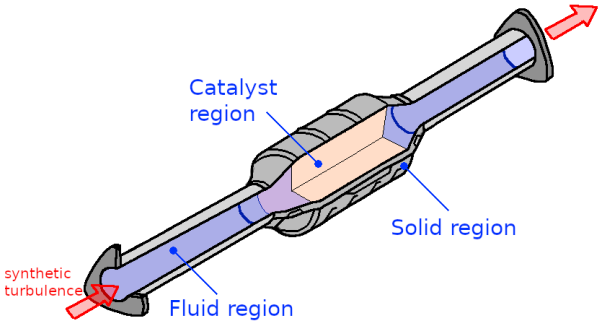

Figure 5.16: Numerical treatment of the catalytic converter configuration. Domain coupling Fluid/Solid/Catalyst regions.

Fig. 5.16 shows the coupled fluid and solid regions that are solved in the numerical studies. The catalytic converter is essentially divided into: (i) two pipe flow regions, (ii) a catalyst region which includes the honeycombs structure, and (iii) the solid region. These regions are coupled via interfaces with each other. The material properties of the solid body are listed in the Table 5.1, while the thermodynamic of the exhaust gas is provided in Appendix A.3.

Table 5.1: Material properties of the solid body of the catalytic converter.

material property	solid region	insulation packing	ceramic
ρ^s (kg/m^3)	7583	1840	1500
κ^s (W/mK)	80.2	0.3	2
C_p^s (J/(kgK)	452	900	1000

In the fully-resolved numerical study, the honeycomb structure of the monolith with 12,468 small ducts is fully resolved by means of the numerical grid with very fine resolution. In order to analyze the grid dependency of the numerical results, three numerical grids with different spatial resolutions are employed (see Table 5.2), denoted here as coarse, medium, and fine. Therefore, each channel in the monolith is discretized in the fluid domain by $(h \times w \times l) = (3 \times 3 \times 16)$ (coarse), $(6 \times 6 \times 20)$ (medium), and $(12 \times 12 \times 24)$ (fine) cells, respectively. This results in a maximum wall distance of $y^+ < 3.2$ at the duct walls of the monolith for the finest spatial resolution, while y^+ is smaller than one in the rest of the computational domain. Thus, the near wall region and the flow in the catalyst region are fully-resolved. In the WFLES/VANS based numerical study, the catalyst region is treated as a porous medium and modeled by VANS method, the computational domain is represented by a single solid region and a single fluid region and discretized by three numerical grids (see Table 5.2) with different spatial resolutions, respectively. The near wall region is modeled by the wall function approach, and the catalyst region by the presented VANS approach. The schematic representation of meshes are depicted in Fig. 5.17, (a) for fully-resolved case and (b) for WFLES/VANS case.

Regarding the boundary conditions, a no-slip velocity boundary condition is applied at the interface between the fluid and solid bodies. For the energy equations, coupled thermal boundary conditions are considered. A uniform heat transfer coefficient ($h_0 =$

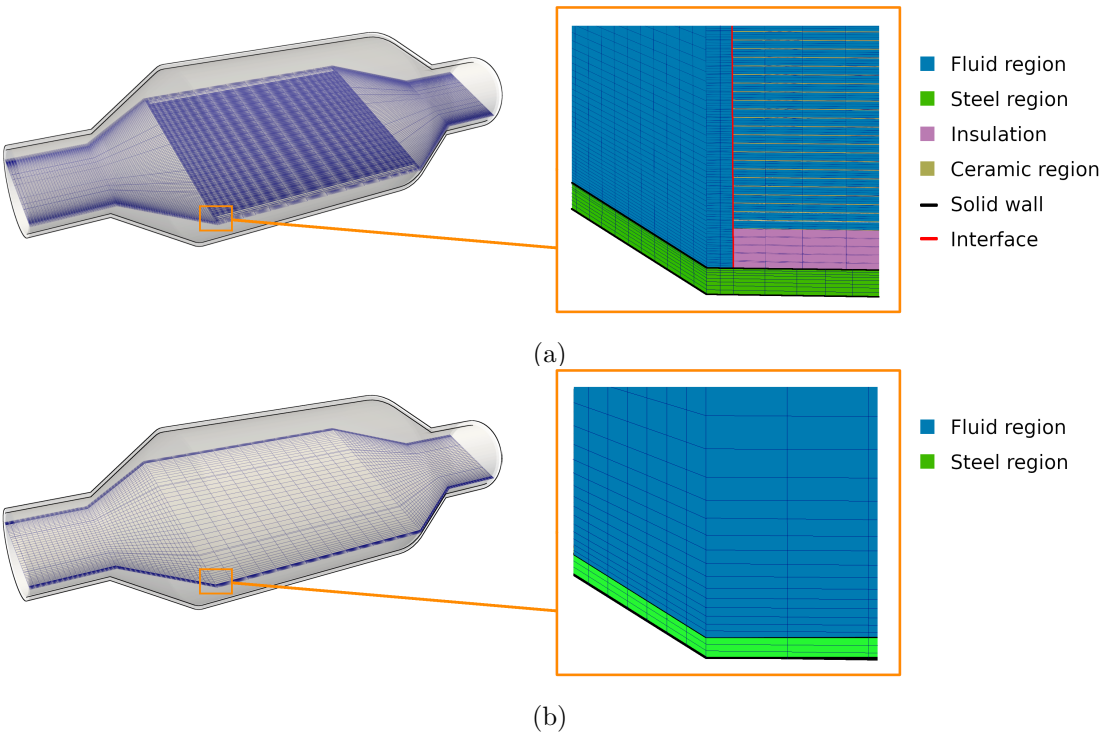

Figure 5.17: Schematic representation of meshes for (a) fully-resolved case and (b) WFLES/VANS case

Table 5.2: Number of grid points used in the fully resolved and modeled numerical studies.

	coarse	medium	fine
resolved: solid part	1,499,560	2,348,408	2,348,408
resolved: fluid part	5,556,400	13,959,292	46,349,536
modeled: solid part	160,320	315,392	516,096
modeled: fluid part	171,008	1,340,416	2,903,040

$152 W/m^2K$) with constant ambient temperature ($T = 298K$) is specified for the outer wall of the solid region, representing the heat transfer to the ambient surrounding. Turbulent inflow conditions are generated using the digital filter approach proposed by Klein in [89]. The sub-grid stress tensor was modeled using the σ-model proposed by Nicoud [124]. As for the unresolved heat transport, a linear diffusivity model with a sub-grid-scale Prandtl number of $Pr_{sgs} = 0.7$ was employed. All simulations are carried out with a low-mach number theory based solver for fluid flow with conjugated heat transfer. Second order numerical schemes in space and time are applied to the simulations, and the maximum CFL number was set to $CFL_{max} < 0.8$. The simulation results are assumed to be converged when the relative residual is smaller than $\varepsilon < 10^{-3}$.

In Figure 5.18, the measured mean pressure drops over the three-way catalytic converter are compared with the simulated values as a function of the volumetric flow rates. A best fit of the measured pressure drop based on the Darcy-Forchheimer law [11] is also provided. This analysis includes two scenarios: one for dry air at a temperature of $298K$ and another for hot exhaust gas at a temperature of $866K$, which represents the bulk temperature in the monolith that is obtained through numerical simulation with fine grid resolution. The pressure drop over the catalytic converter is accurately modeled using the

Darcy-Forchheimer equation, as described in [11]. For the specific catalyst considered in this study, the Darcy-Forchheimer equation is given by:

$$-\frac{\Delta P}{\Delta l} = \frac{\mu}{K}U + \frac{\rho}{k_2}U^2, \tag{5.2}$$

with the fitted coefficients $K = 1.7077 \times 10^{-8} m^2$ and $k_2 = 0.01077 m$. The first term on the r.h.s. describes the pressure drop due to friction, while the second term is related to turbulent dissipation. By means of this equation, the experimental data can be extrapolated to the case with higher volumetric flow rates and non-isothermal conditions.

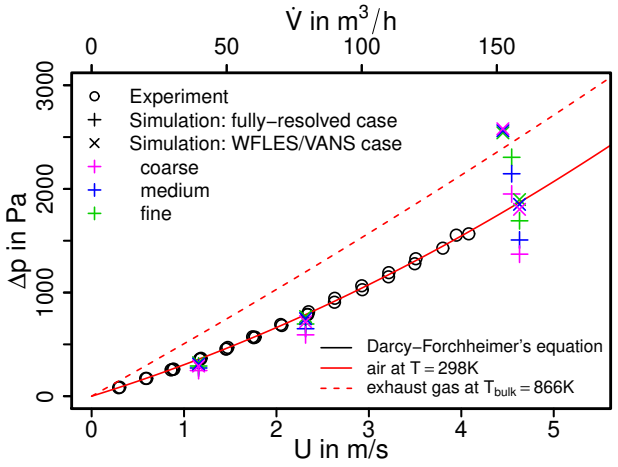

Figure 5.18: Pressure drop characteristic of a three-way catalytic converter of a Lada Niva 21214 vehicle. U denotes the bulk velocity inside the monolith.

As depicted in Figure 5.18, the mean pressure drops obtained from both fully-resolved simulations and WFLES/VANS modeled cases exhibit good agreement with the experimental data and the derived Darcy-Forchheimer relation. This holds true for both dry air flow and hot exhaust gas flow. Therefore, good agreements are achieved for all flow rates under consideration. It is noteworthy that the predicted pressure drops in the fully-resolved simulation case are slightly lower than the measured values, which is mostly visible in the results from the cases with coarse grid and higher flow rates. In contrast, the pressure drops obtained from the WFLES/RANS simulations accurately represent the reference data and exhibit less sensitivity to grid resolution. Even with the coarsest grid, which consists of only 0.68% of the cells used in the fine fully-resolved case, the WFLES/RANS results match well with the experimental data. Furthermore, the computational cost of the fine fully-resolved simulation is approximately 400 times higher compared to the coarse WFLES/VANS simulation.

Along with other factors, the efficiency of a catalytic converter is largely determined by how uniformly the flow and thermal fields are distributed upstream to the monolith. This allows the effective utilization of available surface area in the monolith for the intended purpose of particulate filtration, oxidation, reduction, etc. In this context, Fig. 5.19 shows a snapshot of the instantaneous magnitude velocity field of the isothermal case $\dot{V}$ = 160.0 m^3/h together with the velocity distribution at several cross-sections (S1–S5) and the pressure distribution along the the monolith channel that are obtained by (a) fully-resolved LES, and (b) WFLES/RANS.

A highly turbulent intake jet impinges on the monolith, resulting in recirculation and separation flow in the front of the monolith. As a result, the pressure around the stagnation

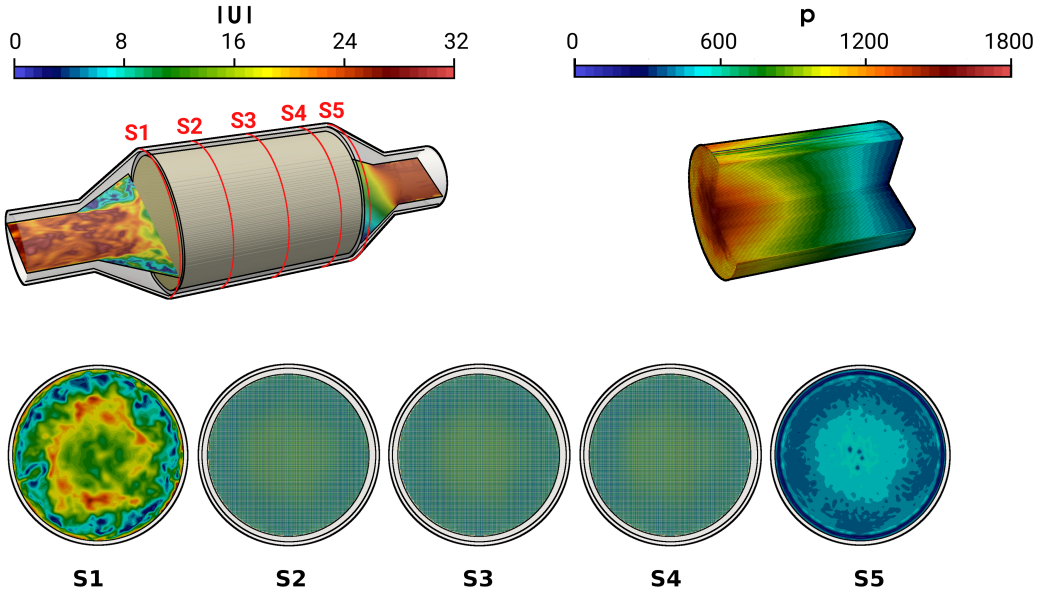

(a)

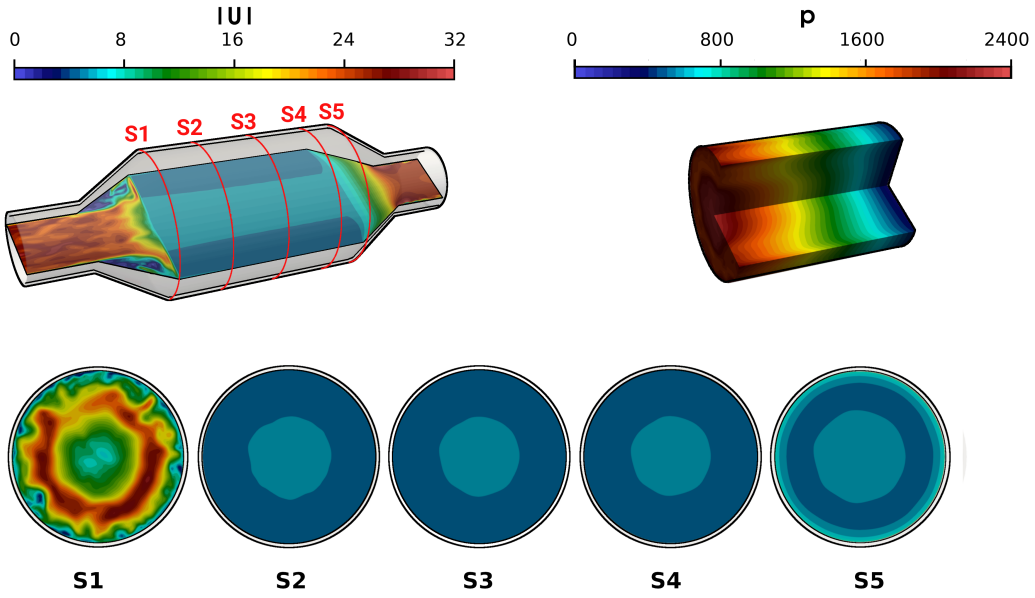

(b)

Figure 5.19: Instantaneous velocity field in the catalytic converter and instantaneous pressure field in the monolith along with velocity profile in various cross sectional planes S1-S5 obtained by (a) fully-resolved LES, and (b) WFLES/RANS.

point is high and decreases rapidly in the flow direction. Traveling further downstream, the flow inside the monolith transitions to a more laminar state, and the pressure distribution becomes more uniform in the radial direction. Both the fully-resolved simulations and the WFLES/VANS modeled cases capture similar fluid flow characteristics, including stagnation, recirculation, separation, and laminarization. In particular, the laminarization of the flow within the monolith is well reproduced in both approaches. Moreover,

the velocity distribution in the catalyst region differs significantly from fully-resolved and WFLES/VANS modeled cases. In the fully-resolved case, even the velocity is small at the stagnation region; the velocity inside the monolith is high around the center line and decreases in radial direction. Whereas, in the case of WFLES/VANS simulation, the velocity distribution is homogeneous though slightly higher value around the centre line in the catalyst region. Furthermore, the velocity profile in the catalyst region remains constant in further downstream (see the velocity profile on sections S2–S4), which holds true for both fully-resolved and WFLES/VANS modeled cases.

This phenomenon is further analyzed quantitatively to gain a deeper understanding of the flow behavior, depicted in Fig. 5.20 (a) and (b) for the predicted mean and root mean square (rms) velocities in longitudinal direction, respectively, at the cross-sections S1–S5. Here, D is the diameter of the inlet pipe and r is the radial coordinate that points to the center ($r/D = 0$ is located at the duct or monolith center line). The quantities of the isothermal case simulated with fully-resolved LES are plotted in black lines, the non-reacting non-isothermal case simulated with fully-resolved LES are plotted in red lines, while these obtained by WFLES/VANS are plotted in blue for isothermal case and in green for non-isothermal case. Notice that dashed lines on S2-S4 represent the velocity profile inside the monolith ducts.

Fig. 5.20 (a) shows that the mean velocity profiles out of the monolith (S1, S5) are not significantly influenced by the heat transfer or applied simulating methods. In contrast, mean velocity profiles differ significantly within the catalyst region. Therefore, the velocity profile in the non-reacting non-isothermal fully-resolved case is of uniform shape along the radial direction, while the velocity magnitude is maximal at center line ($r/D = 0$) and decreases gradually in radial direction in fully-resolved case of isothermal conditions. These observations can be mainly attributed to the change in thermophysical properties, in particular the change in the viscosity of the exhaust gas due to temperature change. Moreover, these properties remained constant under isothermal conditions. In spite of the visible distinction of the velocity distribution in the catalyst region provided by resolved and modeled cases, the dependencies of the velocity distribution on the heat transfer are observed similarly for both fully-resolved cases and modeled cases.

In the case of velocity fluctuations, the analysis in Fig. 5.20 (b) reveals that the rms velocity is initially high at the impinging region (S1), but rapidly decreases within the monolith and remains small throughout the entire monolith. This behavior is observed in both the fully-resolved isothermal and non-isothermal conditions. This indicates that the laminarization of the flow within the monolith is primarily driven by fluid flow effects rather than heat transport phenomena. It is worth noting that the rms velocity for the isothermal conditions is generally higher than that of the non-isothermal conditions, particularly along the impingement section. This can be attributed to the increased viscosity due to the higher temperature in the non-isothermal case. When comparing the rms velocities of the fully-resolved cases to the modeled rms velocities, it is observed that the modeled values are generally smaller.

The temperature distribution inside the catalytic converter predicted by fully-resolved simulation and WFLES/VANS modeling are shown in Fig. 5.22 (a) and (b), respectively, for the fluid regions, the solid parts, and several cross-sections (S1–S5). Similar to the velocity field, the hot turbulent intake jet impinges on the front side of the catalyst. Therefore, the evolution of the thermal field inside the monolith appears to be very similar to that of the velocity field. This holds true for both fully-resolved simulation and WFLES/VANS modeling. However, the fully-resolved temperature gradients are significantly larger at the solid-fluid interface than at the fluid-ceramic interface. This valides for

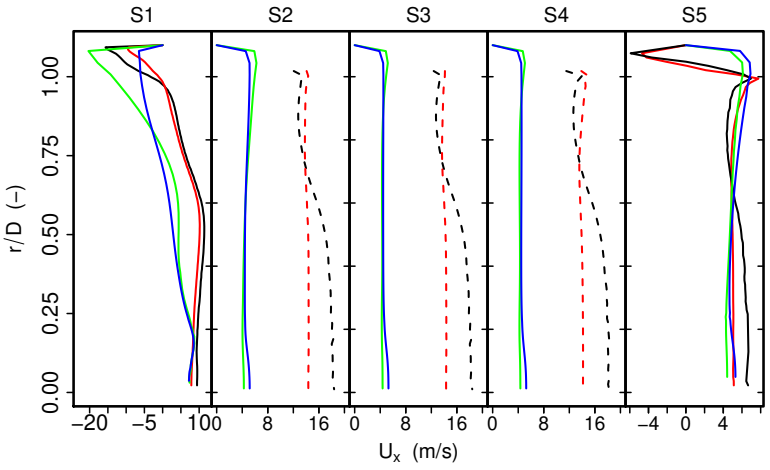

(a)

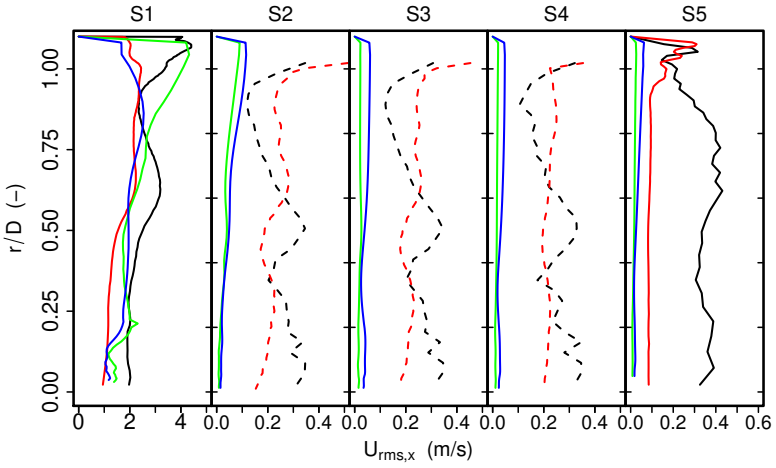

(b)

Figure 5.20: Velocity distributions in the main flow direction at different cross sections for fully-resolved isothermal case (black lines), fully-resolved non-isothermal case (red lines), WFLES/VANS modeled isothermal case (blue lines) and WFLES/VANS modeled non-isothermal case (green lines). The dashed lines represent the velocity profile inside the monolith ducts.

all cross-sections in the monolith (see cross-section S2-S4 in Fig. 5.22). The corresponding mean and rms temperature profiles along the radial direction are plotted in Fig. 5.22 (a) and (b) for the cross-sections (S1–S5), respectively.

The exhaust gas temperature is observed to be relatively low in the front of the monolith, mainly due to intense heat transfer caused by recirculation. Within the monolith, specifically at the cross sections S2-S4, the fully-resolved case shows a rapid heating of the exhaust gas due to heat transfer from the ceramic mass. In contrast, the modeled case without a honeycomb structure exhibits a slower temperature recovery. Both the fully-resolved and modeled cases show homogeneous temperature distributions around the core of the catalyst region. This temperature distribution plays a crucial role in determining the viscosity of the exhaust gas. Specifically, the viscosity is higher around the core region, where the temperature is higher, and lower towards the solid-fluid interface region.

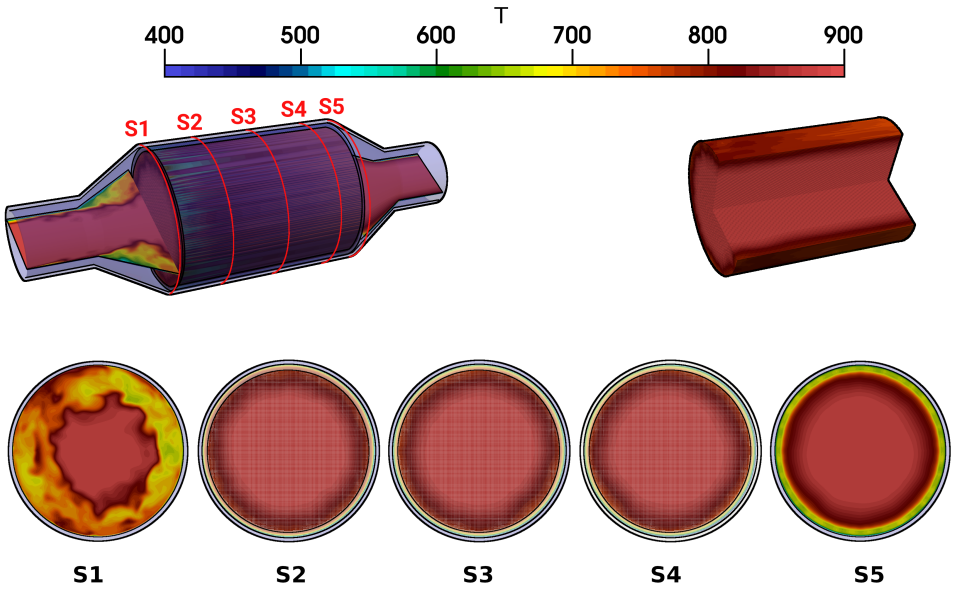

(a)

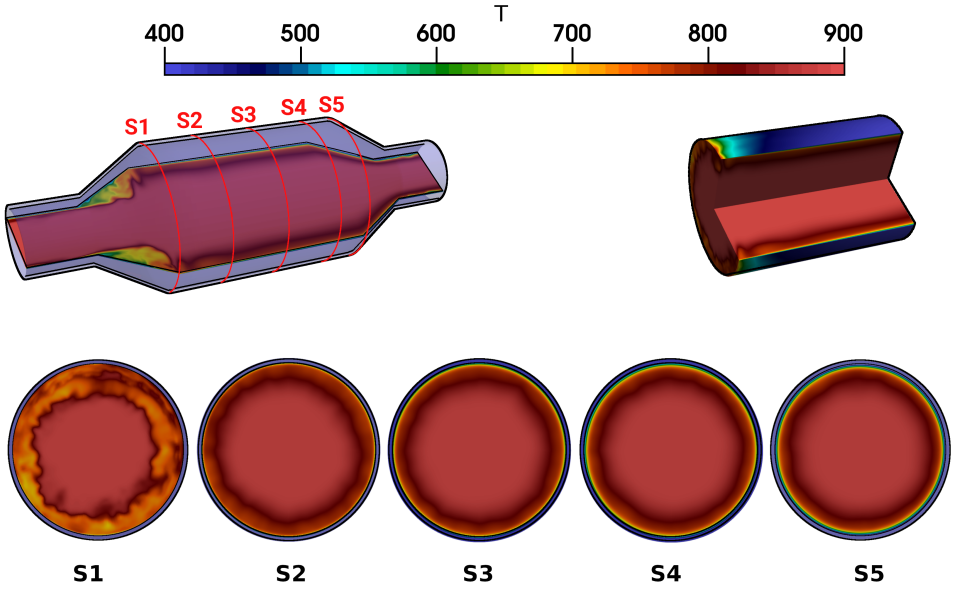

(b)

Figure 5.21: Instantaneous temperature fields in the catalytic converter and in the monolith along with temperature profile in various cross sectional planes $S1 - S5$, results obtained by (a) fully-resolved LES, and (b) WFLES/RANS.

The homogeneous velocity profile observed in the non-reacting non-isothermal case, as shown in Fig. 5.20 (a), can be explained by the presence of homogeneous temperature distributions within the catalytic converter. The temperature fluctuations, as depicted in the rms temperature profile in Fig. 5.22 (b), exhibit significantly higher values at the S1 cross section. However, within the monolith (S2-S4) and to some extent at S5, these fluctuations are more or less negligible in the fully-resolved case. In contrast, the modeled

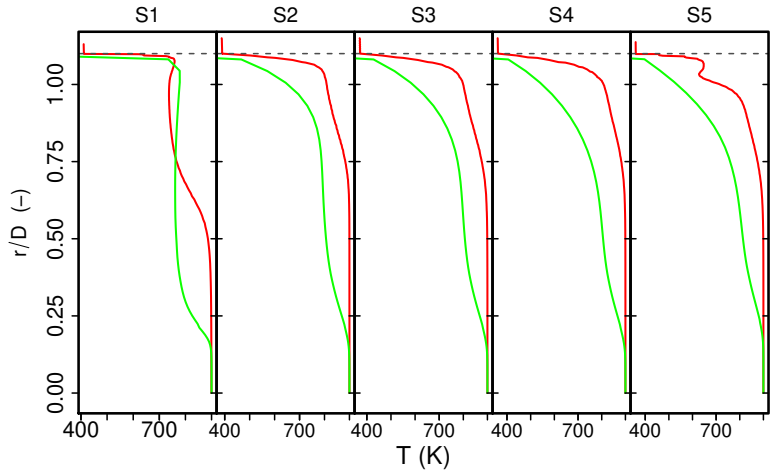

(a)

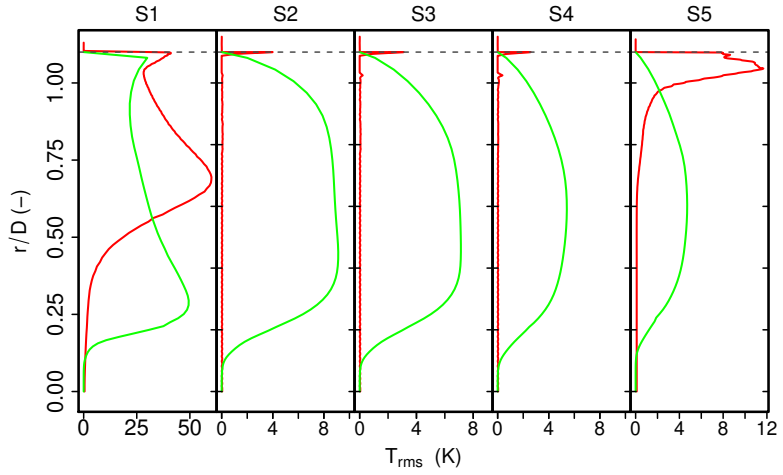

(b)

Figure 5.22: Profiles of mean (a) and rms (b) temperature along the radial direction at various cross sections.

case shows higher rms temperature levels, indicating that an advanced VANS method might be required for a more accurate representation of the temperature distribution inside the catalytic converter.

The relative errors of the heat flux, which is evaluated based on the data of fine fully-resolved case, at solid wall are 0.062%, 0.052% and 0.044% for WFLES/VANS with coarse, medium and fine spatial resolutions, respectively. The modeled results converged to the resolved case with refined spatial resolution, while even with the coarse grid, the WFLES/VANS approach is also able to predict well the heat flux on the solid wall.

To summarize, the following conclusions can be drawn from this study:

- The Darcy-Forchheimer equation is well suited to describe the pressure drop in this specific catalytic converter. Correlation equations based on the experimental data are provided.

- Important characteristic flow features are identified in the catalytic converter, namely the impinging flow with stagnation, recirculation, flow separation, and laminarization

in the catalyst region, which are reproduced by both fully-resolved and WFLES/-VANS modeled simulations.

- The rms velocity decreases rapidly in the monolith, attributing to the flow laminarization process in the narrow monolith channels. This physical process is influenced by the heat transfer dynamics through temperature-dependent thermophysical properties as simulations with and without heat transfer testify.

- The velocity and temperature distribution obtained by fully-resolved simulation and WFLES/VANS modeling differ significantly in the catalyst region. Despite this difference, WFLES/VANS method is able to predict well the pressure drop as well as the heat flux at the solid wall with very low computational expense.

In addition to the present pressure, velocity and temperature distribution in the catalytic converter, the entropy generation due to viscous dissipation and heat transfer of the resolved cases can be also found in the work [103] of the present author.

5.7 Conclusion

In this chapter, the proposed LES near-wall modeling approach is extensively evaluated for various heat and fluid flow scenarios that are commonly encountered in technical applications, particularly in the field of EGAS. The investigated cases include turbulent pulsating heated channel flow, impinging jet on a 45°-inclined heated plate, recirculating flow with heat transfer, turbulent channel flow with conjugated heat transfer, strongly heated pipe flow, and heat and fluid flow inside a catalytic converter. The results show that the proposed LES near-wall modeling approach provides accurate predictions of key parameters in wall-bounded flows, such as skin friction coefficient, Nusselt number, Stanton number, local wall shear stress, mean wall temperature, and pressure drop in a catalytic converter.

The accuracy of the predictions is demonstrated through comprehensive comparisons with DNS and experimental data from the literature. Additionally, in cases where experimental or other DNS references are not available, comparisons are made with near-wall resolved LES and DNS data generated in-house. The proposed LES near-wall modeling approach consistently shows excellent agreement with the reference data, validating its capability to accurately capture the flow and heat transfer characteristics in a wide range of scenarios.

Based on the successful validation and accuracy demonstrated in this chapter, the proposed LES near-wall modeling approach can be confidently employed for further analysis of EGAS under typical driving conditions in the next chapter. Its ability to provide reliable predictions of key parameters will contribute to a better understanding of complex heat and fluid flow phenomena and support the design and optimization of EGAS systems.

Chapter 6

WFLES of an automotive exhaust gas after-treatment system

In this chapter, the focus is on applying the proposed WMLES approach with non-equilibrium wall functions to simulate an automotive EGAS. Specifically, the EGAS of a Lada Niva 21214 vehicle is chosen as the representative case, which is a typical EGAS found downstreams to a four-cylinder gasoline engine. An illustration of the Lada Niva 21214 vehicle with the EGAS (highlighted in red) is depicted in Fig. 6.1.

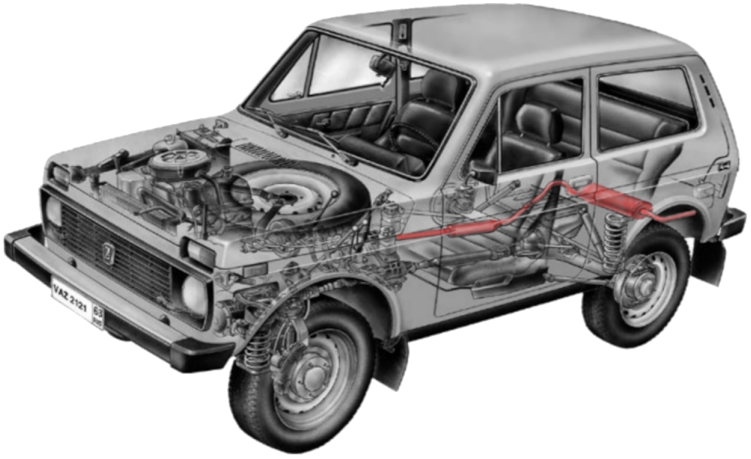

Figure 6.1: Illustration of the Lada Niva 21214 vehicle with the EGAS, highlighted in red color. (modified from [1])

In this work, the focus is on investigating the turbulent heat and fluid flow phenomena occurring within the fluid region, as well as the heat transfer processes in the solid region. The study employs a combination of experimental and numerical methods to gain a comprehensive understanding of these complex phenomena. A detailed description of the test case is given in Sec. 6.1. It is followed by a comparison of the experimental and numerical results, and by further analysis of the distinctive heat and fluid flow characteristics in the EGAS (see Sec 6.2). At the end of this chapter, the main findings of the study are outlined in a conclusion.

6.1 Description of test case

Fig. 6.2 provides a technical drawing of the EGAS of the Lada Niva 21214 vehicle. The EGAS is comprised of various functional components interconnected by metallic tubes. The main circuit of the exhaust gas system can be classified into several parts:

- an exhaust manifold, which connects directly with the engine cylinders, and collects and channels the exhaust gas from individual engine cylinders into the exhaust system,
- a catalytic converter, in which the toxic gases, such as carbon monoxide (CO), nitrogen oxides (NOx), and unburned hydrocarbons (HC), is converted into less harmful substances,
- a front muffler, which is designed by using perforated tubes and baffles, to reduce noise generated by the EGAS,
- a principal muffler, which are designed by using perforated tubes and wave cancellation structures to further reduce sound pollutant.

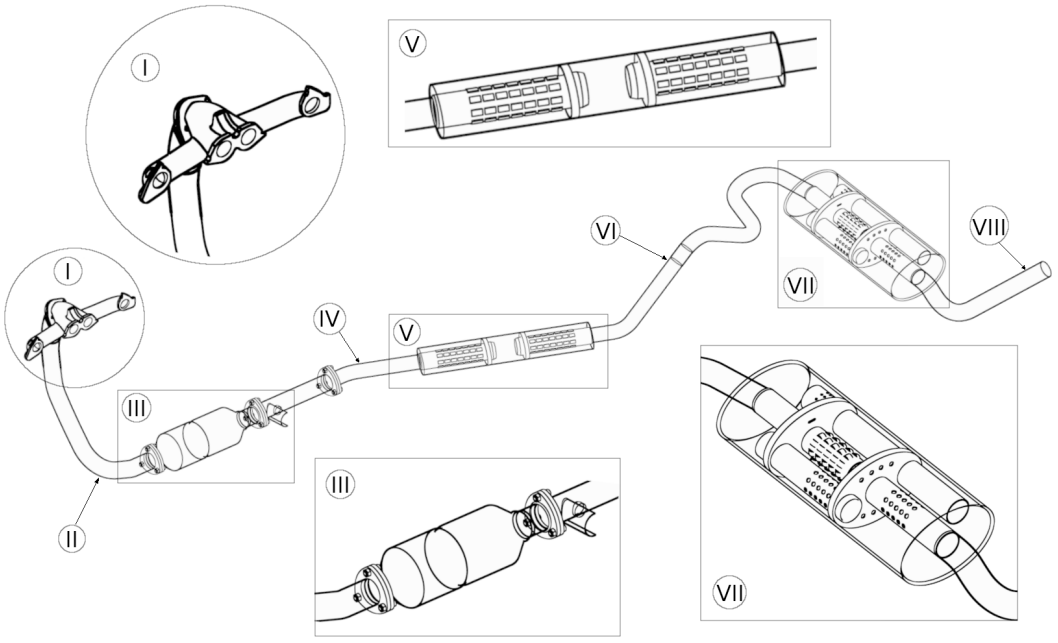

Figure 6.2: Technical drawing of the EGAS of the Lada Niva 21214 vehicle. (I) exhaust manifold; (II) connecting tube 1; (III) catalytic converter; (IV) connecting tube 2; (V) front muffler; (VI) connecting tube 3; (VII) principal muffler; (VIII) tailpipe.

It is worth mentioning that in the present work, some modifications have been made to the exhaust gas system compared to the original system of the Lada Niva 21214 vehicle. These modifications were implemented to facilitate the experimental analysis and measurements of the exhaust gas flow. Specifically: (i) Splitting of Connecting Tubes: The connecting tubes on both sides of the catalytic converter were divided into sections to enable easier assembly and disassembly using flanges. With modification it allows for better accessibility and flexibility during the experimental setup. (ii) Addition of Probe

Locations: Several additional probe locations were introduced in the exhaust system to facilitate temperature and pressure measurements of the hot exhaust gas stream. These probe locations provide valuable data for understanding the thermal and fluid flow characteristics within the system. It is important to note that these modifications do not significantly alter the overall function and operation of the exhaust gas system but rather improve the experimental capabilities for the specific conducted experimental studies.

In the present work, the geometry of the entire exhaust gas system was measured using a GOM ATOS-III 3D-scanner at the Institute for Production Engineering and Forming Machines (PtU) of the Technical University of Darmstadt. Based on the acquired measurement data, a comprehensive CAD model of the entire exhaust gas system was generated. The CAD model incorporates both the fluid flow region and the solid body, providing a detailed representation of the system's geometry. This CAD model serves as a basis for further analysis and simulations.

Four test cases with different operating conditions were investigated in the present study. The operating conditions for each test case are summarized in Table 6.1. Test case 1 was specifically analyzed using numerical simulation, while all operating conditions were investigated experimentally.

Table 6.1: Test operating conditions for the exhaust gas system of the Lada Niva 21214. Vehicle speed is estimated by means of the vehicle's wheel diameter (175/80R16 88Q = 686 mm), the rear differential transmission ratio (3,9:1) and differential case (1,2:1).

case	gear (ratio)	engine velocity	driving speed
1	5th (0.82:1)	2036 rpm	67.4 km/h
2	5th (0.82:1)	2500 rpm	84.4 km/h
3	5th (0.82:1)	3000 rpm	101.1 km/h
4	4th (0.82:1)	3000 rpm	82.9 km/h

6.1.1 Experimental setup

In the experimental studies, various parameters related to the operating conditions of the Lada Niva 21214 vehicle were recorded during the test runs. These parameters include the actual driving speed, engine velocity, intake air mass flow, air inlet temperature, refrigerant temperature, and engine load. The data acquisition was carried out using the OBD-II (On-Board Diagnostics) system of the vehicle. In order to obtain temperature measurements at various points within the exhaust gas system, thermocouples (Type J) were employed. These thermocouples were carefully installed inside the exhaust gas stream at specific locations: including the manifold, the inlet/outlet of the catalyst, the principal muffler inlet and the tailpipe. Additionally, the pressure drop over the catalytic converter was measured by a differential pressure sensor (differential pressure transmitters PD-23 of Keller AG). The specific probe locations for temperature and pressure measurements are depicted in Fig. 6.3, and the measured quantities are summarized in Tab. 6.2.

The experiments were conducted on the Bundesstraße B26 between Darmstadt and Dieburg in Germany on 11-12-2020 during the winter season. Careful attention was given to ensuring stable and steady-state operating conditions during the test runs. This was important to obtain reliable and accurate measurements. During the experiments, all relevant quantities (see Tab. 6.2) were continuously measured and monitored at a frequency of one measurement per second. These measurements were then time-averaged over a sufficient period to obtain representative values.

Table 6.2: Measured quantities during the test runs. Probe locations are shown in Fig. 6.3.

property	probe location	labeling	Units
temperature	manifold outlet	T_1	°C
temperature	catalyst inlet	T_2	°C
temperature	catalyst outlet	T_3	°C
temperature	inlet principal muffler	T_4	°C
temperature	exhaust exit	T_5	°C
pressure difference	between catalyst inlet/outlet	Δ P	mbar
driving speed	OBD-II	km/h	V_S
engine velocity	OBD-II	RPM	ω
intake air mass flow	OBD-II	g/s	M_{air}
inlet air temperature	OBD-II	°C	T_{in}
refrigerant temperature	OBD-II	°C	T_{cool}
engine load	OBD-II	%	L_{eng}

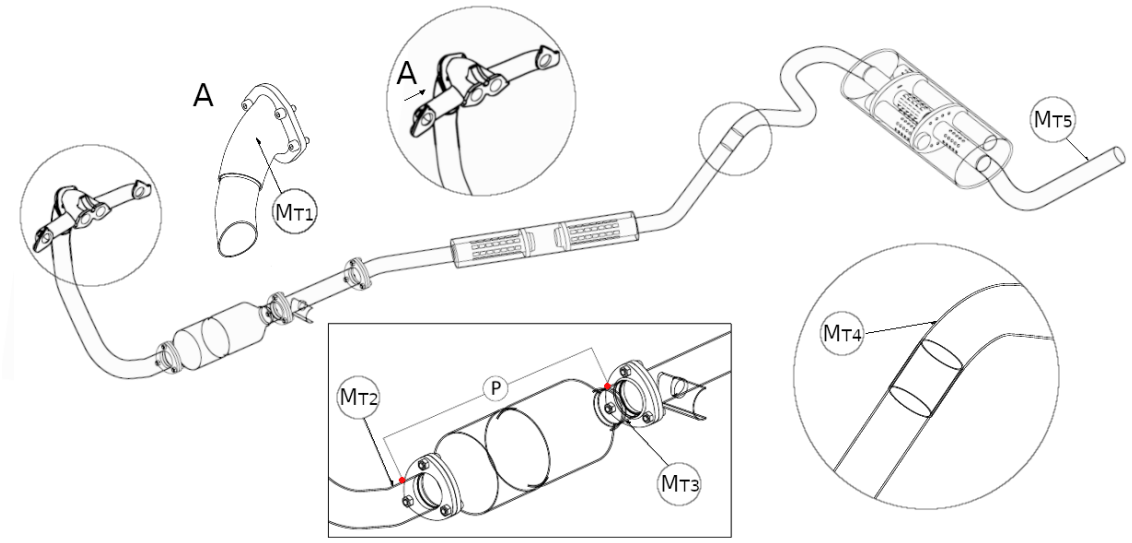

Figure 6.3: Probe locations at the exhaust gas system. (M_{T1}) temperature probe at the manifold outlet, (M_{T2}) temperature probe at catalyst inlet, (M_{T3}) temperature probe at catalyst outlet, (M_{T4}) temperature probe at principal muffler inlet, (M_{T5}) temperature probe at exhaust exit, (P) pressure difference between catalyst inlet/outlet.

6.1.2 Numerical setup

In addition to the experimental study, a numerical investigation of the turbulent fluid flow with conjugate heat transfer in the complete EGAS is carried out using the proposed WFLES approach. However, it is important to note that in the present work, the chemical reactions occurring within the catalytic converter is not explicitly resolved numerically. Instead, an additional heat source term is included in the energy equation to model the heat release due to a complete conversion of CO (0.9% of total volume) into CO_2. This heat source term represents the energy released during the chemical reaction and is essential for capturing the heat generation within the EGAS. Whereas, the impact of chemical reactions on the overall composition and thermodynamic properties of the exhaust gas is considered to be minimal and assumed to be negligible. Therefore, the exhaust gas components and their mass fractions are treated as constant throughout the simulation. By

assuming constant mass fractions, the computational complexity associated with solving the species transport equations and tracking the changes in concentrations is simplified. This allows for a more efficient simulation of the fluid flow and heat transfer processes without sacrificing significant accuracy for the specific objectives of the study.

The fluid flow with conjugate heat transfer inside the monolith is calculated using a VANS model (see Appendix A.2) with the Darcy-Forchheimer coefficients presented in Sec. 5.6. This modeling approach allows for the simulation of the fluid flow and heat transfer in porous media, such as the honeycomb structure of the monolith. Moreover, the exhaust gas is treated as a homogeneous mixture of different gases, and it is considered as a single component Navier-Stokes-Fourier gas. Its thermodynamic properties are calculated by means of seven-coefficient NASA polynomials [19] and transport properties are approximated based on Sutherland's formula [181]. Thereby, the material laws for the properties of the exhaust gas are evaluated using the material laws of the mixture. The thermodynamic properties of the applied exhaust gas is described in Appendix A.3.

A crank angle (CA) dependent mass flow of the exhaust gas is estimated through a zero-dimensional modeling of the in-cylinder process according to [66], and presented in Appendix A.4. For which the driving speed is approximately $67 km/h$ at 5th gear with engine velocity of 2000 rpm, and the estimated exhaust gas mass flow rate is determined to be $64.072 kg/h$. This value represents the average mass flow rate of the exhaust gas during the specified driving condition. The velocity boundary condition at the inlet of this EGAS (manifold) is realized by superimposing the CA dependent mass flux with turbulent fluctuations, which are generated by the digital inflow generator proposed by Klein et al. in [88]. While, the temperature at inlet is set to a constant value with $T_{inlet} = 1100K$. At the outlet (tailpipe) Neuman boundary condition with zero gradient is specified for temperature and velocity, whereas the pressure is set to a constant value of 1atm. Thereby, back flows are allowed from the surrounding to the EGAS. A coupled temperature boundary condition (see Sec. 5.4) and no-slip velocity boundary condition are applied to the fluid-solid interface. At the outer solid wall, interface of ambient air and solid body of the EGAS, the temperature boundary condition is divided into a part relevant to radiation and another part due to forced convection, which are evaluated according to empirical formulations given in Appendix A.1. Notice that the manifold (part I) and the upstream portion of the connecting tube (part II) up to the bending position of the elbow structure are covered by engine compartment. It is therefore reasonable to assume that the heat transfer is governed by free convection and radiation in this section of the EGAS.

In order to analyze the grid dependency of the numerical study, the computational domain is discretized by two numerical grids with different spatial resolutions, denoted here as coarse and fine cases. The cell number of both cases are summarized in Table 6.3 for the solid and fluid regions. Thereby, all connecting tubes and the catalytic converter are discretized using structured numerical grids with an open source software $GMSH$ [57]. In contrast, the numerical grids for the manifold and the perforated tubes in the front and principle mufflers (see Fig. 6.4) are generated using *snappyHexMesh*, a standard utility of OpenFOAM.

Table 6.3: Cell numbers of applied numerical grids.

	coarse	fine
solid region	$1,101,843$	$1,689,799$
fluid region	$1,882,966$	$6,206,238$

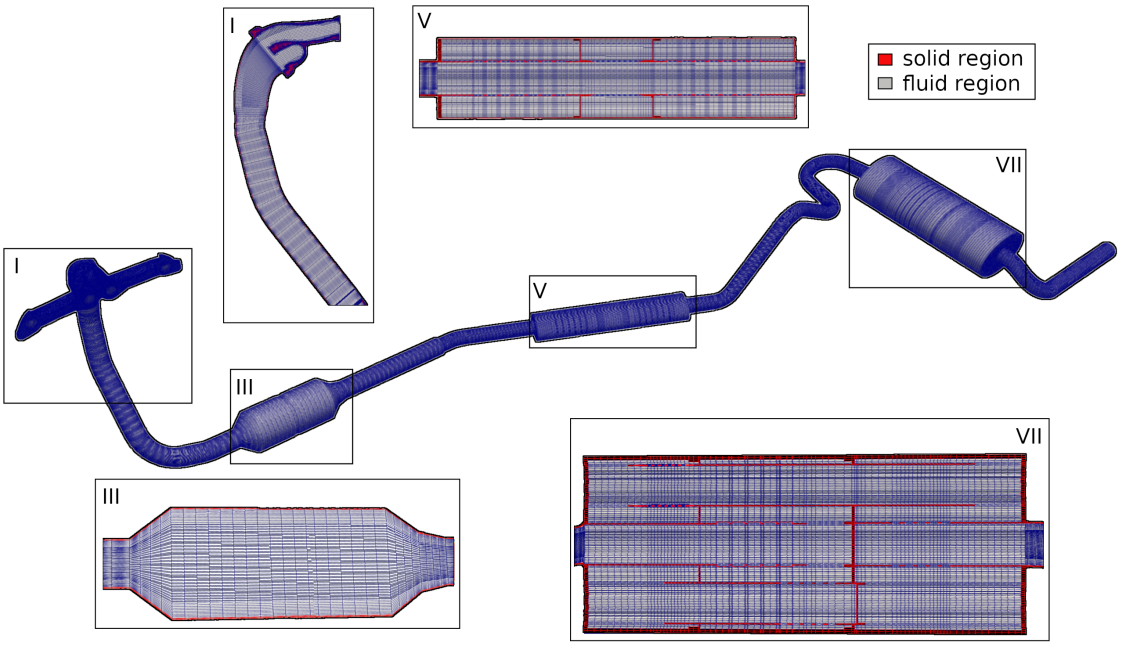

Figure 6.4: Representation of the applied coarse numerical grid for solid (in red) and fluid regions (in gray).

The employed numerical method in this study is the proposed WFLES approach, which is combined with the σ-subgrid scale model (see Chap. 3). Second-order accurate schemes are applied to both spatial and temporal discretization of the transport equations. In line with the experimental conditions, the EGAS is subjected to a heating process until it reaches a quasi-stationary state. During this process, the outer wall temperature of the EGAS gradually increases and eventually stabilizes. This quasi-stationary state refers to a condition where the outer wall temperature remains relatively constant over time. To speed up the initializing procedure, the energy equations are solved under frozen fluid flow conditions, in which the continuity and momentum equations are not solved, i.e. the velocity field and pressure field are not solved or updated. The initializing procedure is then continued with time dependent inflow conditions until accomplishing of quasi-stationary state. After the initializing procedure, the simulation is carried out with a maximum CFL-number equal to one. At every 5e-4s, the results with relevant fields are stored for CA based averaging (120 time steps each period) with the total simulated time of 50 periods. To simulate each period $2,000$ CPUhs and $18,000$ CPUhs are required for the coarse case and fine case (see Tab. 6.4), respectively.

6.2 Result and discussion

In this section, both experimental and numerical results are presented to provide a comprehensive analysis of the studied EGAS. At first, the numerical predictions are compared with the experiment in order to establish the validity of the adopted numerical techniques. Next, the validated numerical model is used to characterize the heat and fluid flow in the EGAS. This includes an analysis of the heat and fluid flow features of the EGAS, a frequency analysis at different probe locations within the EGAS and an analysis of the quantities associated with thermal and fluid dynamic process. Notice that the experimen-

tal data are recorded with a frequency of one Hertz for a total record time of $300s$. Thus, a CA-based analysis of the experimental data is not available. Instead, the experimental data is presented in this section using time-averaged values. For more detailed analysis and reference, the raw experimental data for all test cases can be found in Appendix A.5.

6.2.1 Comparison of numerical and experimental results

In Fig. 6.5, a comparison between the predicted pressure drop over the catalytic converter and the bulk temperature at different probe locations is presented. The numerical results are shown in red, while the measured data is shown in black. The dashed lines represent the averaged values based on the crank angle (CA), and the solid lines represent the time-averaged values. Additionally, Tab. 6.4 provides the time-averaged pressure drop (ΔP) and temperature at different probe locations for both the simulation and the experiment. This table allows for a quantitative comparison of the results obtained from the numerical simulations and the measurements.

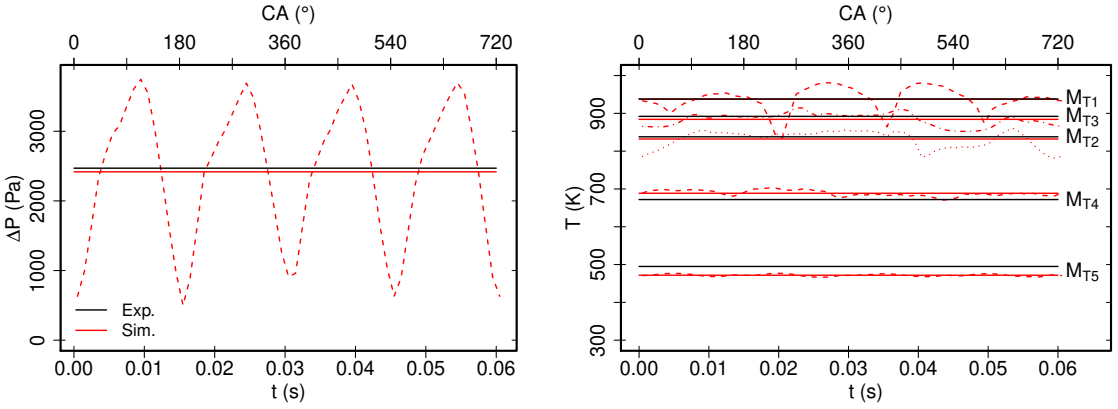

(a) (b)

Figure 6.5: Comparison of pressure drop over catalytic converter (a) and temperature at different positions. - - -: CA based averaged numerical value, —: time-averaged value, experimental data in black, numerical data in red.

The CA-averaged pressure drop, shows in Fig. 6.5, exhibits a characteristic frequency of $66.7Hz$, which is same as the frequency of the incoming mass flow rate from the ICE (see Appendix A.4). It is interesting to observe that the signal of ΔP is slightly delayed in comparison with that of the mass flow. Besides this, the predicted time-averaged pressure drop compares very well with the experimental data with a relative error of 2.12% (see Tab. 6.4). The predicted time-averaged bulk temperature agrees well with the corresponding measurements as shown in Fig. 6.5 (b) and Tab. 6.4. The obtained temperature profiles confirm the expected temperature evolution of the exhaust gas along the EGAS. As the exhaust gas flows through the system, it undergoes cooling due to heat transfer to the surrounding environment. However, in the catalytic converter (part III), a different phenomenon occurs. In this region, the exhaust gas undergoes an exothermic reaction where harmful pollutants are converted into less toxic substances. As a result, the exhaust gas is heated up by the heat released during the reaction. This physical behavior of the temperature evolution is clearly observed in both the experimental data and the simulation results. This excellent agreement between the experimental and simulated temperature profiles indicates that the simulation approach is able to capture the heat transfer and heat release due to chemical reaction occurring in the catalytic converter accurately. Similar

Table 6.4: Time-averaged measured quantities under the operating condition *case 1*.

	ΔP (Pa)	T_1 (K)	T_2 (K)	T_3 (K)	T_4 (K)	T_5 (K)
experiment	2469.87	937.48	836.58	891.77	669.14	497.35
simulation	2417.53	937.22	832.19	884.12	688.58	471.79

results are observed by the simulation with coarse spatial resolution. Thus, these results are not shown here for the sake of clarity. The global excellent agreement between the numerical results and the measured data of the pressure drop and bulk temperature in the EGAS indicates that the proposed WFLES approach is suitable for studying turbulent fluid flow with conjugate heat transfer in the EGAS. Therefore, it allows further studies or analysis of the heat and fluid flow, turbulent properties, and dynamic characteristics, which are provided by the proposed WFLES approach.

6.2.2 Heat and fluid flow characteristics

A snapshot of the instantaneous mechanical pressure distribution along the EGAS and the magnitude velocity field in functional components, namely manifold (I), catalytic converter (III), front muffler (V), and principal muffler (VII), is depicted in Fig. 6.6 for $CA = 240°$. The mechanical pressure P varies within the EGAS in a range of $(-0.05, 0.05)$bar. This confirms that the density variation of exhaust gas inside the EGAS is weakly dependent on the pressure fluctuation and is primarily determined by the temperature. Furthermore, negative pressure is also observed in VII and VIII, which can result in backflow within those components. The velocity distribution snapshot in Fig. 6.6 illustrates that an intake jet emitted from cylinder 2 rapidly disintegrates within the exhaust pipe. As the flow progresses downstream, the exhaust gas impinges on the front of the catalyst monolith (III), resulting in recirculation and separation flow in this region, accompanied by a decrease in mechanical pressure. Moving further downstream, the flow transitions to a laminar state within the monolith (III). The flow characteristics in III closely resemble those observed under stationary operating conditions, as described in Section 5.6. After a certain distance downstream of the catalyst, the flow becomes turbulent again and moves from the front muffler (V) towards the principal muffler (VII). Notably, it can be observed that the gas flow decelerates and loses its turbulent intensity along V and VI. This deceleration is primarily attributed to the cooling process of the exhaust gas. Subsequently, the turbulent exhaust gas impinges on the baffle near the middle cross-section of the principal muffler, leading to a highly turbulent flow with a low velocity magnitude further downstream. This turbulence is mainly caused by the complex geometry with perforated tubes and the intricate design of the principal muffler. Finally, the exhaust gas is emitted into the surrounding air through tailpipe, with the possibility of backflows occurring.

The instantaneous temperature distribution within the EGAS is shown in Fig. 6.7 for $CA = 240°$. At the same cross-section, the temperature of the exhaust gas is significantly higher than it within the metallic solid body. As the exhaust gas progresses from the entrance of I to the tail of VIII, it undergoes significant cooling. The only exception is at section III, where the exhaust gas is heated up due to chemical reactions in the catalytic converter. Therefore, the temperature evolution derived from time-averaged quantities, as described in Sec. 6.2.1, is confirmed by this snapshot of the instantaneous temperature distribution. Additionally, it is interesting to note that in I, the hot jet initially adheres to the wall and then crosses the flow near the interface between I and II.

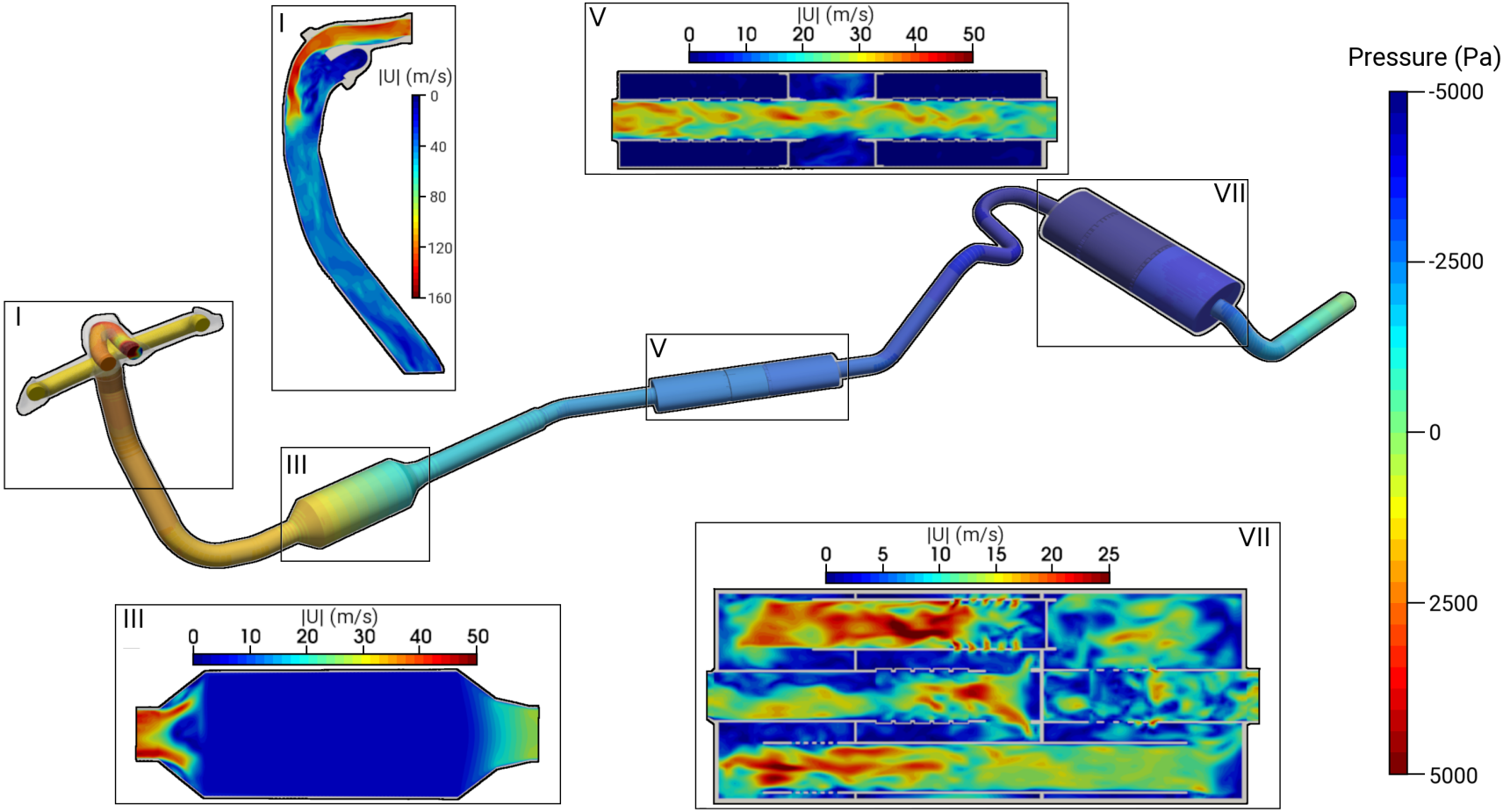

Figure 6.6: Instantaneous mechanical pressure distribution along the EGAS and the magnitude velocity field in the functional components, namely manifold (I), catalytic converter (III), front muffler (V) and principle muffler (VII) for $CA = 240°$.

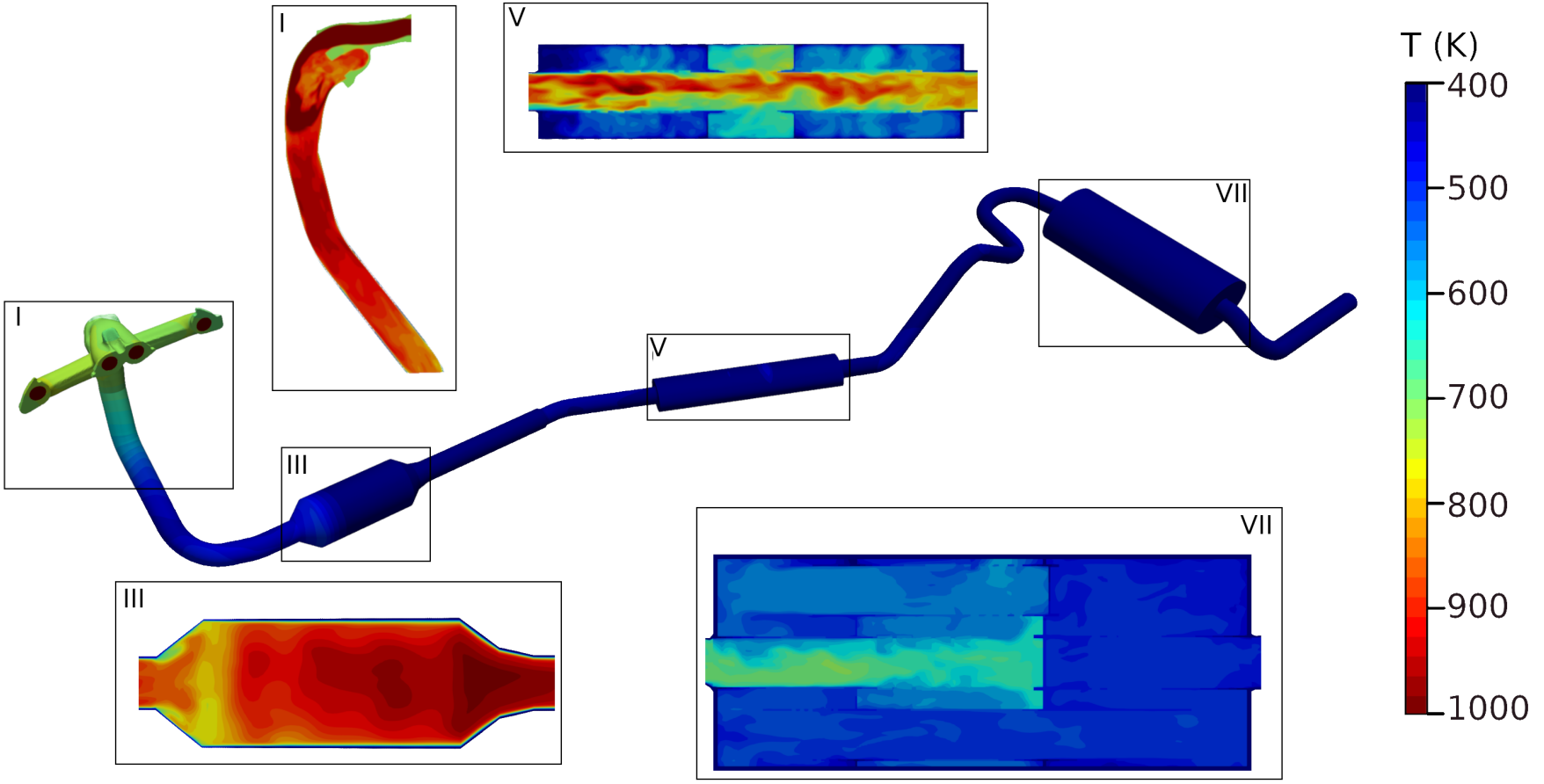

Figure 6.7: Instantaneous temperature distribution along the EGAS for $CA = 240°$

Fig. 6.8 displays the phase-averaged mean temperature $\langle T \rangle$ (represented by the red line) and the mean velocity component normal to the cross-section of the EGAS $\langle U \rangle$ for $CA = 240°$ along the center line l of the EGAS. The position $l = 0$ corresponds to the location directly after the manifold (I). It is worth noting that, contrary to normal pipe flow, the maximum velocity and temperature within the EGAS are not always located at the center of the cross-sections. This is particularly evident in the downstream region of highly shaped tubes. The velocity experiences a rapid increase in section II and remains

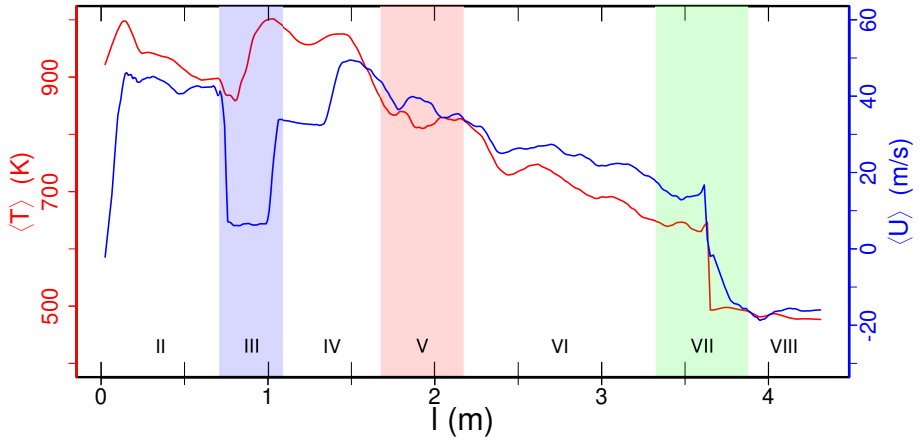

Figure 6.8: Phase-averaged mean temperature $\langle T \rangle$ (red line) and mean velocity component $\langle U \rangle$ normal to the cross-section of the EGAS (blue line) along the centre line l of the EGAS. $l = 0$ is located at the centre of the connecting plane between manifold (I) and connecting tube 1 (II).

relatively constant throughout the rest of the flow path until reaching the catalytic converter. At the entrance cross-section of the catalytic converter (III), the velocity starts to decrease due to the expansion. Subsequently, the contraction at the end of III and in the middle of connecting tube 2 (IV) causes an acceleration of the gas flow. As the exhaust gas passes through the front muffler (V), connecting tube 3 (VI), and the initial portion of the principal muffler (VII), it undergoes cooling, resulting in a significant decrease in velocity. Moving further downstream to the principal muffler, the flow impinges on the muffler baffle, resulting in a very low velocity within this region. Additionally, the baffle in VII serves to block the backflow that occurs downstream of the baffle. It is worth noting that the velocity profiles downstream of bending tubes exhibit significant redistribution.

As depicted in Fig. 6.8, the temperature profile along the EGAS exhibits a similar trend to that of the velocity profile. The temperature decreases rapidly along the EGAS, with the exception of section III. Furthermore, the temperature profile can be divided into two distinct parts. In the first part, $l < 1.5m$, the temperature oscillates around $\sim 950K$, while in the second part ($l > 1.5m$), it decreases significantly faster. This difference in temperature behavior is primarily attributed to the transition from laminar to turbulent flow conditions and the variations in thermal conditions at the exhaust gas pipe wall.

Fig. 6.9 displays the phase-averaged turbulent kinetic energy k (shown in blue) and the rms temperature T_{rms} (represented by the red line) for $CA = 240°$ along the center line l of the EGAS. At the entrance of section II, the turbulent kinetic energy k is notably high, primarily due to the pulsating inflow condition and the complex flow path of the manifold. As the fluid flow progresses into the monolith region, it becomes laminarized, resulting in a rapid decrease in k. However, further downstream ($l > 1.5m$), as the

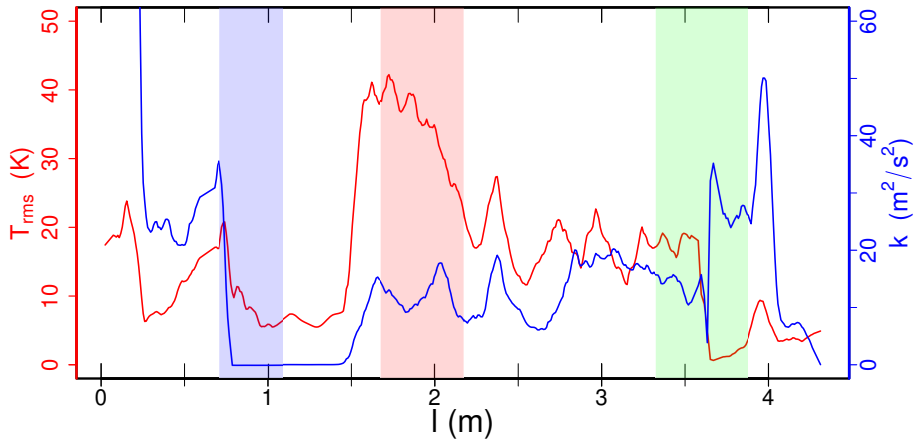

Figure 6.9: Phase averaged rms of temperature T_{rms} (in red) and turbulent kinetic energy k for $CA = 240°$ along the centre line l of EGAS (definition of l see Fig. 6.8).

exhaust gas passes through the elbow tube, k increases once again. Additionally, it is observed that the turbulent intensity is enhanced in the near downstream region of the bending tube with a small bending angle. Furthermore, despite the low mean velocity near the middle section of VII and VIII, the turbulent intensity in this region is extremely high. This is mainly attributed to the backflow from the outlet of the EGAS, leading to significant turbulence. The trend of the phase-averaged rms temperature T_{rms} follows a similar pattern to that of k. Elevated values of T_{rms} are observed near the entrance of section II. As the flow progresses through the (quasi-)straight tube, T_{rms} decreases, whereas it is enhanced in the tube with a small bending angle. However, in contrast to k, high rms temperature values are observed in the monolith region (III) where the flow is predominantly laminar. As pointed out in Sec. 5.6, this non-physical behavior might be minimized by an advanced VANS modeling approach. Moreover, T_{rms} reaches its global peek near the interface between IV and V, and decreases rapidly inside V. Further phase-averaged numerical results of the EGAS are provided in Appendix A.6 for different CA, which are similar to the results presented in this section.

Both the instantaneous and phase-averaged flow fields exhibit highly intricate fluid flow characteristics with heat transfer, as captured by the proposed WFLES method.

6.2.3 Frequency analysis

Fig. 6.10 (a) shows the energy spectrum for the velocity component normal to cross-section, while Fig. 6.10 (b) displays the temperature variance spectrum at different probe positions from M_{T1} to M_{T5} along the centre line of the EGAS (probe locations see Fig. 6.3). The dashed black lines represents the inertial subrange with a theoretical slope of $-5/3$. In Fig. 6.10 (a), it is evident that the turbulent kinetic energy is highest in the exhaust manifold (probe location M_{T1}) and decreases rapidly towards the inflow of the catalytic converter (M_{T2}). Inside the catalytic converter, the flow becomes laminarized, and high-frequency turbulent structures dissipate (M_{T3}). Additionally, all energy spectra exhibit a characteristic peak at a frequency of $f = 66.7n\ Hz$ ($n = 1, 2, 3, ...$). This frequency corresponds to the inflow frequency from the ICE. Notably, at M_{T1}, the dominant frequency is $f = 16.7Hz$, representing the frequency of a single cylinder. This suggests that the flow around probe position M_{T1} is primarily influenced by a single cylinder.

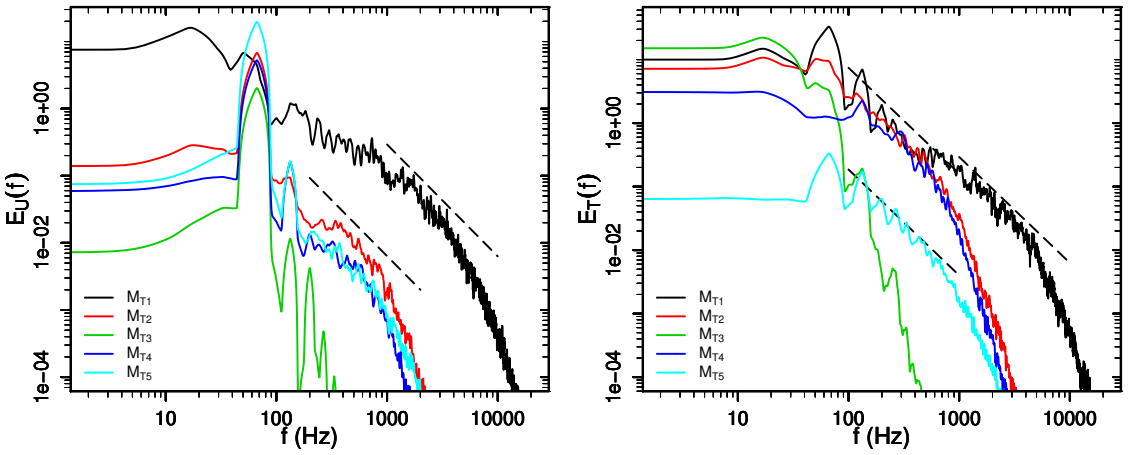

(a) (b)

Figure 6.10: Energy spectrum of the velocity components normal to cross-section (a) and temperature variance spectrum at different probe locations (see Fig. 6.3).

A similar trend can be observed in the temperature variance spectrum depicted in Figure 6.10 (b). Peak values of E_T occur at frequencies of $f = 16.7Hz$ and $f = 66.7nHz$. This indicates that the heat transport in the EGAS is influenced by the fluid flow dynamics, particularly the turbulent inflow from the ICE. However, it is notable that the process of laminarization in the catalytic converter is less prominent in the case of temperature variance compared to turbulent kinetic energy. This suggests that the catalytic converter significantly influences the heat and fluid flow dynamics within the EGAS.

6.2.4 Process analysis

The pressure drop occurs across each functional component (exhaust manifold, exhaust pipe, catalyst, front muffler, principal muffler) as well as across the entire EGAS. It is a crucial parameter in the engineering design of such systems. The pressure drop profile at specific time instances, such as different CAs, depends significantly on the heat and fluid flow dynamics of an EGAS. This behavior is examined in Fig. 6.11, which illustrates the variation of mechanical pressure p_d along the center line l of the EGAS for different CAs.

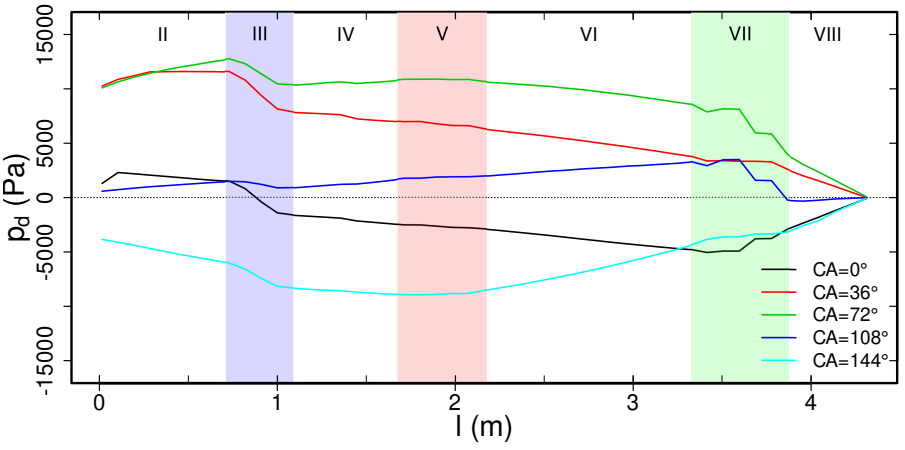

Figure 6.11: Variation of mechanical pressure along EGAS in 1/4 period

Fig. 6.11 illustrates significant variations in the mechanical pressure p_d along both the length l of the EGAS and the engine status represented by CA. The highest pressure drop occurs at $CA = 72°$, while the minimum is observed at $CA = 144°$. Interestingly, for $CA = 144°$, the mechanical pressure becomes negative, accompanied by significant backflow. Analyzing the evolution of p_d along the center line l of the EGAS, it is evident that the pressure drop is particularly prominent across the catalytic converter (III). Specifically, for the current operating conditions, the average pressure drop over the catalytic converter is $\Delta P_{III} = 2418Pa$, accounting for over 50% of the total pressure drop across the EGAS. This emphasizes the importance of the catalytic converter in the fluid dynamic design of an EGAS. In addition, the time-averaged mean and maximum pressure drops across the various components of the EGAS under the given operating conditions are summarized in Tab. 6.5.

Table 6.5: Time-averaged mean and maximum pressure drop ΔP across EGAS components

ΔP (Pa)	I	II	III	IV	V	VI	VII	VIII
mean	131.49	146.67	2417.53	209.94	81.89	200.44	554.89	667.56
max	562.28	2044.58	3771.49	912.86	944.84	4098.92	3365.61	6374.03

The heat balance of the EGAS including the inflow from the ICE, chemical reaction, heat transfer to the surrounding and outflow is summarized in Tab. 6.6. The time-averaged values of the heat power and heat flux transferred from the solid bodies of the various EGAS components to the surrounding air are listed in Tab. 6.7.

Table 6.6: Heat balance of the EGAS

	Inflow	Chemical reaction	Heat transfer	Outflow
Heat source $\dot{Q}(kW)$	25.55	1.58	-17.83	-9.30

Table 6.7: Time-averaged heat power $\dot{Q}$ and heat flux $\dot{q}$ transferred from solid body of different EGAS components to ambient air

	I	II	III	IV	V	VI	VII	VIII
Heat power $\dot{Q}$ (kW)	2.60	4.16	0.77	0.91	2.26	2.87	3.74	0.57
Heat flux $\dot{q}$ $(\frac{kW}{m^2})$	9.35	36.78	6.37	9.95	16.79	18.12	11.83	7.78

In the current EGAS configuration and under the given operating conditions, approximately 6% of the total thermal energy is released through chemical reactions occurring in the catalytic converter. The remaining portion of thermal energy is transferred from the ICE into the EGAS. About two-thirds (65.72%) of the thermal energy is transferred through the solid bodies of the EGAS components to the surrounding environment, while one-third of the heat is emitted along with the exhaust gas into the ambient air. Regarding the time-averaged heat power ($\dot{Q}$) and heat flux ($\dot{q}$), the maximum values are observed at region II, where the temperature of the exhaust gas is relatively high. As region I is covered by the engine compartment, the values of $\dot{Q}$ and $\dot{q}$ are relatively low in this region.

6.3 Conclusion

In this chapter, the proposed WFLES approach in conjunction with a VANS model is applied to simulate an automotive EGAS of a Lada Niva 21214 vehicle, which serves as a representative example of a four-cylinder gasoline engine EGAS. The main focus of this study is to investigate the turbulent heat and fluid flow phenomena occurring within the fluid region of the EGAS, while also considering the heat transfer from the EGAS to the surrounding air through its solid body. To achieve this, a combination of experimental and numerical methods is utilized.

The main findings of this stud are summarized as follows:

- the proposed WFLES approach enables accurate prediction of heat and fluid flow processes within the EGAS under typical driving conditions. This assertion is validated through comparisons with experimental data, demonstrating the reliability and effectiveness of the WFLES approach in capturing the heat and fluid flow dynamics of the EGAS;
- heat and fluid flow within the EGAS are indeed highly complex, involving various fluid flow phenomena, such as laminarization in the catalytic converter, recirculation and separation in the exhaust manifold, and impinging flows at the front of the monolith;
- large-scale motions within the EGAS are primarily influenced by the inflow from the ICE, which exhibits a characteristic frequency of 66.7 Hz. On the other hand, the smaller turbulent motions in the EGAS display a more universal behavior, and their energy spectra conform to the inertial subrange theory for these scales;
- the pressure drop in the EGAS is particularly significant over the catalytic converter. For the current operating conditions, the mean pressure drop across the catalytic converter constitutes more than 50% of the total pressure drop experienced by the EGAS;
- two-thirds (65.72%) of the thermal energy is transferred through the solid body to the surrounding air, while one-third of the heat is emitted together with the exhaust gas to the ambient air.

Chapter 7

Summary and Outlook

With the growing computational power, particularly in recent decades, the utilization of LES techniques for predicting unsteady turbulent heat and fluid flow phenomena has expanded from academic research to industrial applications. LES is considered to be accurate and reliable for capturing these fluid and thermal dynamics within complex industrial configurations. However, the accurate simulation of near-wall dominant flows in LES requires numerical grids scaled by the viscous length scale. This necessity significantly increases the computational expense and time requirements for LES of wall-bounded flows. Consequently, this limitation has restricted the widespread application of LES to realistic industrial flows that involve solid walls.

To overcome this challenge, a commonly employed approach is to model the flow in the near-wall region, which aims to accurately capture essential quantities such as turbulent characteristics in the outer layer, frictional velocity, and heat flux in an energy system. By adopting this approach, computational costs can be significantly reduced while still obtaining reasonably accurate results. Numerous near-wall modeling approaches have been reported in the literature, in which turbulent quantities in the inner layer is either resolved by means of RANS methods or modeled using a wall-stress model. In comparison with the former one, the latter one was reported to be flexible and low time-consuming, which is therefore more applicable for industrial applications. Whereas, it was also established that the latter one has some drawbacks in dealing with unsteady non-equilibrium wall bounded flows. This motivates the present work, which aims to develop a reliable and flexible wall-stress model for LES that allows to predict unsteady non-equilibrium wall bounded turbulent flows with heat transfer in industrial flow applications, e.g. EGAS. To showcase the applicability and reliability of the proposed WFLES approach, the EGAS of a Lada Niva 21214 vehicle is chosen as a benchmark test case in this thesis. The present study is structured into four main steps to accomplish this objective.

In the first step, several well-known wall functions were reviewed and analyzed. During this analysis, certain limitations of these wall functions were identified, such as discontinuities in the buffer layer or their inability to handle non-equilibrium or unsteady turbulent flow, among others. To address the limitations of existing wall functions, novel non-equilibrium wall functions are, therefore, proposed in this study. These wall functions are based on the assumption of a non-equilibrium correction function that considers local non-equilibrium effects in heat and fluid flow. The proposed wall functions are formulated as single analytic expressions for momentum transport and scalar transport, ensuring their continuous validity across the entire range of y^+ (the dimensionless wall distance). They account for transient and local non-equilibrium effects and can be easily extended to incorporate additional source term contributions. Furthermore, these wall functions are

suitable for a wide range of molecular Prandtl numbers. The interpolation formula used for μ_t (turbulent viscosity) and α_t (turbulent thermal diffusivity) in these formulations ensures consistency with the second law of thermodynamics. The accuracy and reliability of the proposed wall functions are validated by comparing them with existing reference data.

Secondly, the novel wall functions are implemented into the framework of OpenFOAM to address conjugate heat transfer problems in the context of incompressible heat and fluid flow, considering both constant and variable physical properties for LES. Thereby, the wall functions are utilized to evaluate the wall shear stress or heat flux, which in turn determine the boundary values for turbulent viscosity or diffusivity. With this it avoids explicitly correcting the velocity or temperature at the wall, resulting in slightly less accurate velocity or temperature values in that region. However, the quantities modeled by the wall functions, such as wall shear stress or heat flux, demonstrate good agreement with reference values.

In the next step, the implemented WFLES approach is verified or validated through various generic configurations related to EGAS. These configurations include pulsating heated boundary layer flow, impingement cooling/heating, recirculation/reattachment flow, turbulent conjugate heat transfer, strongly heated boundary layer flow, and heat and fluid flow in a monolithic catalytic converter. The turbulent quantities predicted by the proposed WFLES approach are compared well with DNS and experimental data from the literature, as well as with internally generated by near-wall resolved LES, DNS and experimental measurements. These good agreements demonstrate that the proposed WFLES approach allows for an economical yet accurate prediction of crucial turbulent quantities in wall-bounded flows, such as the skin friction coefficient, Nusselt number, Stanton number, local wall shear stress, and mean wall temperature. Furthermore, the combination of WFLES/VANS with the Darcy-Forchheimer correlation has been established. This combination utilizes measured pressure drop over the catalytic converter under different operating conditions for isothermal air and extrapolates it for hot exhaust gas. It accurately models the pressure drop over the catalytic converter, heat flux at the outer solid wall, and heat and fluid flow out of the catalyst region with significantly reduced computational effort and simulation time. It should be noted that the heat and fluid flow inside the catalyst region, as modeled by VANS, may exhibit significant differences from the fully-resolved case. Nevertheless, the proposed WFLES approach remains suitable for the analysis of engineering applications under industrial operating conditions, such as EGAS.

Finally, the proposed WFLES approach is applied to investigate the heat and fluid flow processes in the EGAS of a LADA Niva 21214 vehicle under typical driving condition. For the purpose of validation, the pressure drop across the catalytic converter and temperature at several probe positions are measured and recorded under different driving conditions. The predicted temperatures and pressure drop obtained from the proposed WFLES approach show good agreement with the measured reference data. It turns out the proposed WFLES approach is appropriate to describe the turbulent fluid flow with conjugate heat transfer in the EGAS under typical driving conditions.

All the evidence confirms a conclusion that the proposed WFLES approach is capable to represent the fluid and thermal dynamics in engineering applications under realistic operating conditions. However, as an engineering numerical tool the proposed methodology can be surely improved in different areas, the most important among them are suggested as follows:

- The WFLES approach can be further extended to appraise the entropy generation in energy systems, which enables an entropy-generation-based irreversibility analysis of technical energy systems and can be a useful tool for both detailed understanding of the underlying physical phenomena and in identifying the key parameters for efficient operation. Thereby, it is required to establish a correlation between entropy production and the wall function modeled together with near-wall turbulent quantities.

- The applied VANS model is able to predict well the pressure drop as well as the heat flux at the solid wall with very low computational expense. However, the temperature or velocity profiles along certain cross sections predicted by VANS model differ significantly from the resolved ones. Therefore, an advanced VANS model might be developed to provide thermal behaviours inside the catalytic converter more accurately.

- Another very promising way to speed-up such type of simulations is to apply the Lattice Boltzmann Methods (LBM) to solve the heat and fluid flow inside complex energy systems, such as EGAS. As it has already been demonstrated by the author, this can reduce the computational cost by a factor of $\sim 30 - 50$ (see [63]).

Appendix

A.1 Empirical correlations for heat transfer in EGAS

The heat transfer from an energy system to the surrounding can be evaluated according to some empirical correlations. It is divided into four different types, namely free convection, forced convection and mixed convection and radiation. The empirical correlation for each form are given in [17], and summarized in this section.

Free convection

In the case of free convection, or pure natural heat exchange, i.e. the flow motions in surrounding are not driven by external force, the Nusselt number is expressed as

$$Nu_{free} = \left(0.752 + 0.387(Raf_3)^{1/6}\right)^2, \tag{A.1}$$

with $f_3 = (1 + (0.559/Pr)^{9/16})^{-16/9}$, and the Rayleigh number $Ra = |Gr|Pr$. The dimensionless Grashof number Gr for ideal gas reads

$$Gr = -\frac{\rho g L^3 (T_w - T_\infty)}{T_\infty \mu^2}, \tag{A.2}$$

where T_w is the wall temperature of the heat source, while T_∞ the surrounding temperature. $g = 9.8m/s^2$ is the acceleration of gravity and $L = \pi d_{outer}/2$ the characteristic length of the pipe calculated with the outer diameter d_{outer}.

Forced convection

Regarding forced convection the heat transport is determined by the fluid motion, which is generated by external sources. The Nusselt number is formulated as a summation of a laminar part Nu_{lam} and a turbulent part Nu_{tur}:

$$Nu_{forced} = 0.3 + \left(Nu_{lam}^2 + Nu_{tur}^2\right)^{1/2}, \tag{A.3}$$

with

$$Nu_{lam} = 0.664 Re^{1/2} Pr^{1/3}, \tag{A.4}$$

$$Nu_{tur} = \frac{0.034 Re^{0.8} Pr}{1 + 2.43 Re^{-0.1}(Pr^{2/3} - 1))} \tag{A.5}$$

Mixed convection

By accounting the combined influence of both free convection and forced convection is termed as mixed convection, which is approximated by

$$Nu_{mixed} = (Nu_{free}^3 + Nu_{forced}^3)^{1/3} \tag{A.6}$$

Radiation

Heat flux due to radiation is expressed as

$$q_{rad} = \varepsilon_{rad}\sigma_{rad}(T_w^4 - T_\infty^4), \tag{A.7}$$

with the emissivity of the pipe material $\varepsilon_{rad} = 0.17 + (T_w - 273)/6950$ and the Stefan-Boltzmann-constant $\sigma_{rad} = 5.67e - 8$.

The total heat flux is evaluated by

$$q = \alpha_{sur}(T_w - T_\infty) + q_{rad}, \tag{A.8}$$

where the first part in the r.h.s. represents the heat flux due to free convection, forced convection or mixed convection and the heat transfer coefficient is evaluated using $\alpha_{sur} = Nu\lambda_{sur}/L$, where λ_{sur} ist the thermal conductivity of the surrounding material (i.e. air in this case) and L the characteristic length (e.g. length of EGAS). The heat flux of radiation is calculated directly from Eq. A.7. A standard OpenFOAM boundary condition, named *externalWallHeatFluxTemperature*, is applied with specified heat transfer coefficient and emissivity to update the boundary condition for temperature field.

A.2 Volume-Averaged Navier-Stokes modeling approach

Regarding the turbulent fluid flow inside the catalytic converter, a general quantity ψ can be expressed as:

$$\psi^* = \psi H(\mathbf{x}), \tag{A.9}$$

where ψ^* is defined in the entire catalytic converter, $H(\mathbf{x})$ is a Heaviside-function. The volume averaging operation can be basically treated as a spatial filtering procedure, similar as described in Chapter 3. Therefore, by applying top-hat filter the superficial averaged variable is expressed as:

$$\langle\psi\rangle^s = \frac{1}{V_\Delta}\int_{V_F}\psi \mathrm{d}V, \tag{A.10}$$

where $V_\Delta = \Delta_l^3$ represents the averaging window with length of Δ_l and V_F the fluid volume inside the averaging window. The intrinsic volume averaged quantity is given as:

$$\langle\psi\rangle = \frac{1}{V_F}\int_{V_F}\psi \mathrm{d}V. \tag{A.11}$$

Favre volume averaged quantity reads

$$[\psi] = \frac{\langle\rho\psi\rangle}{\langle\rho\rangle}. \tag{A.12}$$

The volume averaged quantity of the spatial derivatives yields:

$$\left\langle\frac{\partial\psi}{\partial x_i}\right\rangle^s = \frac{\partial\langle\psi\rangle^s}{\partial x_i} - \frac{1}{V_\Delta}\int_S G\psi n_i \mathrm{d}S. \tag{A.13}$$

The volume averaged continuity equation, similar with Eq. 3.3, reads

$$\frac{\partial\langle\rho\rangle^s}{\partial t} + \frac{\partial\langle\rho\rangle^s[U_i]}{\partial x_i} \tag{A.14}$$

and the momentum equation, like Eq. 3.4, is formulated as

$$\frac{\partial\langle\rho\rangle^s[U_i]}{\partial t}+\frac{\partial\langle\rho\rangle^s[U_i][U_j]}{\partial x_j}+\frac{\partial\langle p\rangle^s}{\partial x_i}-\frac{\partial\langle\tau_{ij}\rangle^s}{\partial x_j}+F_i=0, \tag{A.15}$$

where F_i represents the summary of the sub-filter stresses, which is similar to the sub-grid stresses in LES, and the integral term (see Eq A.13) due to spatial derivatives, can be treated as an additional pressure gradient, and evaluated by Darcy–Forchheimer equation:

$$F_i=\frac{\langle\eta\rangle^s]}{K}[U_i]+\frac{\langle\rho\rangle^s}{k_2}([U_k][U_k])^{1/2}[U_i], \tag{A.16}$$

in which the coefficients K and k_2 can be provided by an experimental study. For a detailed derivation refers to [50]. It worth mentioning that in this work the Volume-Averaged Navier-Stokes (VANS) model is not applied to the heat transfer in the monolith.

A.3 Thermodynamic properties of applied exhaust gas

The species composition of the exhaust gas has a constant value according to [41] and summarized in Tab. A.1. Instead of treating the exhaust gas as a mixture of different gases, it is considered as an homogeneous single component Navier-Fourier gas, whereby thermodynamic properties are calculated by means of seven-coefficient NASA polynomials [19] and transport properties are approximated based on Sutherland's formula [181]. Thereby, the material laws for the properties of the exhaust gas are evaluated using the material laws of the mixture. The molar mass M of the presented exhaust gas is equal to $0.02863 kg/mol$, and the density is calculated for a reference pressure at $1 atm$. Using NASA coefficients, which is obtained by a least square fit and listed in Tab. A.2, the heat capacity C_p (associated with $a_1 - a_5$), the sensible enthalpy h (a_6) and the entropy s (a_7) are expressed as polynomial. The dynamic viscosity μ and the thermal conductivity λ are evaluated by the model of Sutherland with two coefficients $A_{Suth} = 1.5335\text{e-}6$ and $T_{Suth} = 195.6627$, respectively. A comparison of the fitted values and the theoretical values are depicted in Fig. A.1. An excellent agreement is observed, the presented coefficients are therefore applied in the simulation.

Table A.1: Species composition of exhaust gas

species [-]	CO_2	H_2O	O_2	N_2	CO
fraction [%]	12.3	13.8	0.7	72.3	0.9

Table A.2: NASA coefficients of exhaust gas. Generated by a least square fit.

NASA coefficient	a_1	a_2	a_3	a_4	a_5	a_6	a_7
$T \leq 1000K$	3.48	7.08e-4	-2.61e-7	1.24e-9	-7.77e-13	-1.10e4	4.15
$T > 1000K$	3.13	1.77e-3	-5.91e-7	9.04e-11	-5.10e-15	-1.10e4	5.88

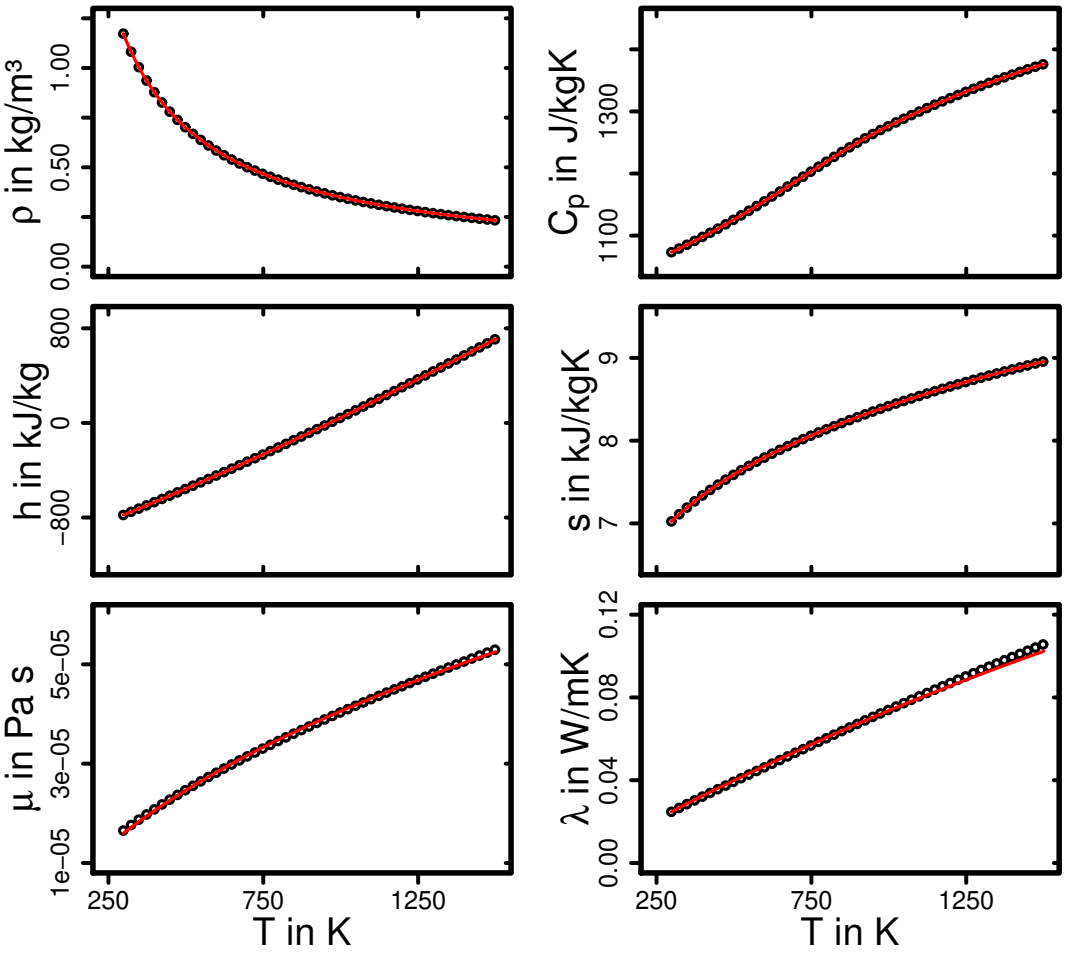

Figure A.1: Comparison of the thermodynamic and transport properties calculated by the existing material laws and its coefficients (in circles) and calculated by the new material laws of exhaust gas, in which the coefficients are generated by least square fits (in lines)

A.4 Operating conditions of a LADA Niva 21214 vehicle at 2000 rpm and 5th Gear

The engine's technical characteristics of the tested LADA Niva 21214 are summarized in the Tab. A.3.

Table A.3: Engine specifications of LADA Niva 21214

Engine's technical characteristics	Value
Bore diameter	8.2cm
Stroke	8cm
Compression Ratio	9.3
Maximum cylinder volume	473.38cc
Engine size	1690cc

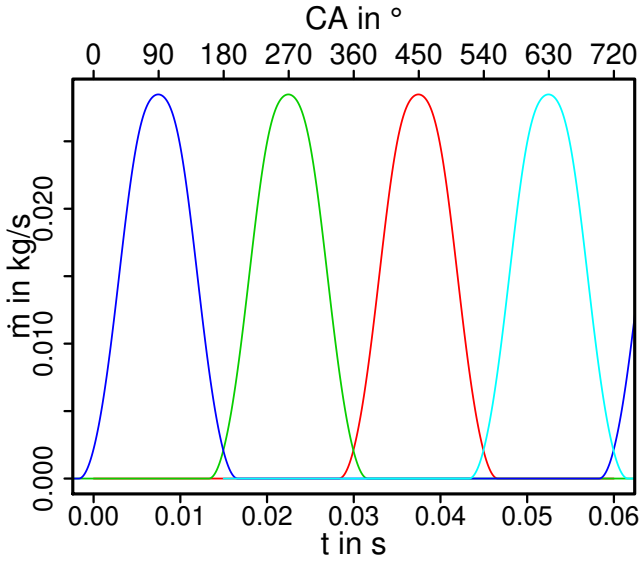

Figure A.2: Mass flow of exhaust gas at exhaust valve. red, green, cyan and blue represent cylinder 1, cylinder 2 , cylinder 3 and cylinder 4, respectively.

The time-mass flow ratio of the exhaust gas is estimated through a zero-dimensional modeling of the in-cylinder process according to [66]:

$$\dot{m} = C_e \frac{A_r p_e}{(T_e)^{1/2}}, \tag{A.17}$$

where the valve curtain area is approximated by $A_r = \pi D_v l_v$ with D_v the valve head diameter and l_v the valve lift, which is modeled by a sinus function. The C_e is modified according to the operating condition (e.g. 2000RPM at 5th-Gear for $\dot{m} = 64.072 kg/h$). The exhaust gas pressure p_e and temperature T_e around the exhaust valve are evaluated from the preliminary simulation and experiment, and set as $p_e = 1.015e5Pa$ and $T_e = 1100K$. The mass flow of exhaust gas at exhaust vavle is depicted in Fig. A.2.

A.5 Measured pressure drop and temperature

The pressure drop across the catalytic converter and the temperature at five probe locations (see Fig. 6.3) were recorded under four operating conditions, which are summarized in Tab. 6.1, and shown in Fig. A.3. Time-averaged measured quantities of the test conditions read in Tab. A.4.

Table A.4: Time-averaged measured quantities for the test operating conditions.

case	RPM	$\dot{m}$ (kg/h)	ΔP (Pa)	T_1 (K)	T_2 (K)	T_3 (K)	T_4 (K)	T_5 (K)
1	2036	64.07	2469.87	937.48	836.58	891.77	669.14	497.35
2	2502	82.73	3222.77	972.89	879.80	926.71	708.34	523.68
3	3032	103.70	5106.35	1017.10	937.53	990.39	774.82	564.46
4	3026	87.56	3973.88	997.40	909.46	963.32	751.55	556.84

Quasi-stationary state is presented in all test cases. Thereby, the pressure drop fluctuates temporally loosely around the mean value. Whereas, the temperature varies in a limited interval, which narrows along the EGAS. These features hold true for all test cases.

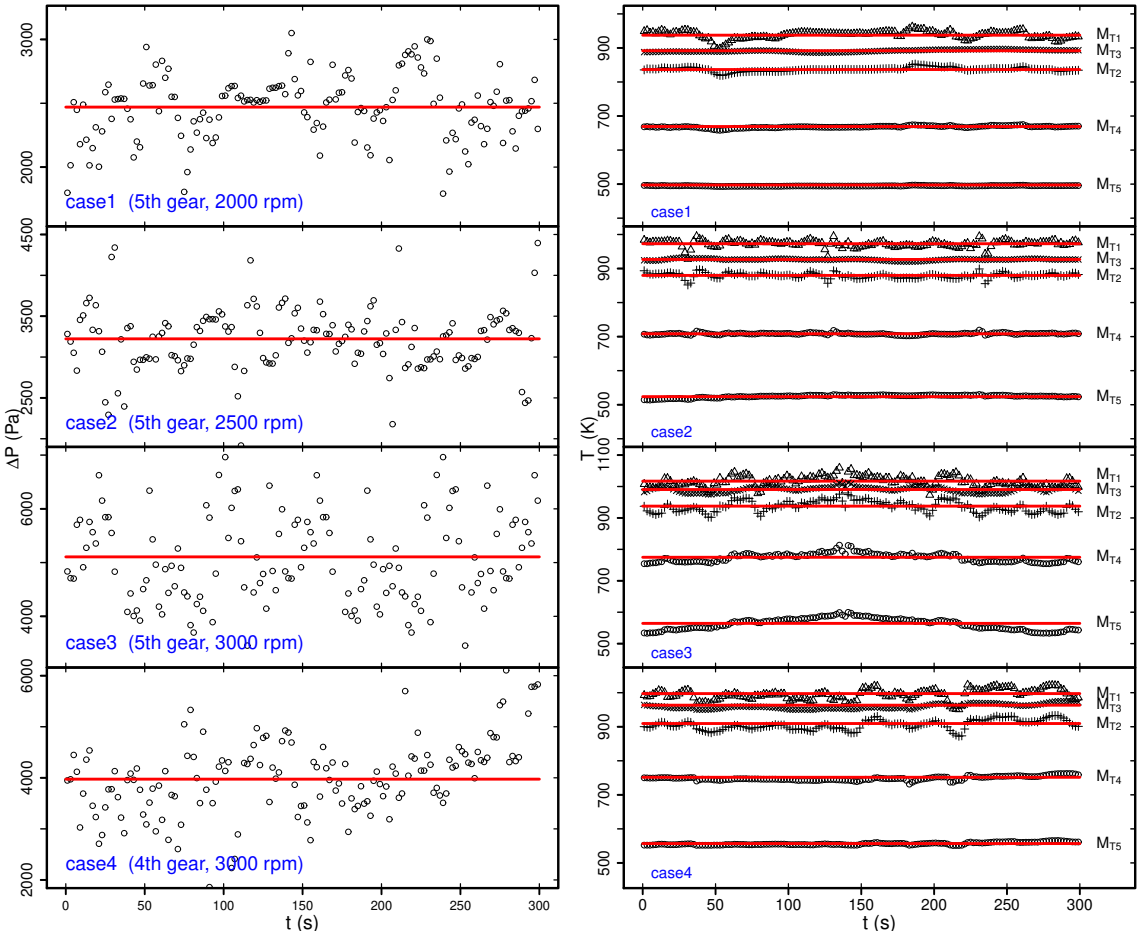

(a) (b)

Figure A.3: Measured pressure drop (a) over catalytic converter and temperature (b) at different probe locations (probe locations see Fig. 6.3) under different operating conditions. ○: instantaneous value, —: time-averaged value.

It is also observed, that the increasing engine speed at same gear enhances the mass flow rate of exhaust gas $\dot{m}$, pressure drop over catalytic converter ΔP and the temperature T_i in the EGAS. While a downshift from 5th gear to 4th gear results in reducing of the above mentioned quantities. Moreover, the exhaust gas is heated up in the catalytic converter, in which more thermal energy is released by the chemical reaction than it transfers to the ambient surrounding. Whereas significant cooling of exhaust gas is observed elsewhere in the EGAS.

A.6 Numerical results of the EGAS at different CAs

Detailed results obtained by the WFLES study of the EGAS of an Lada Niva 21214 (see Chapter 6) are presented in the following figures, including mean velocity and temperature (Fig. A.4), rms velocity and temperature (Fig. A.5), thermal/kinetic energy densities and mechanical pressure (Fig. A.6) as a function of crank angle $CA°$. Additionally, time series of thermal and total kinetic energy are provided in Fig. A.7.

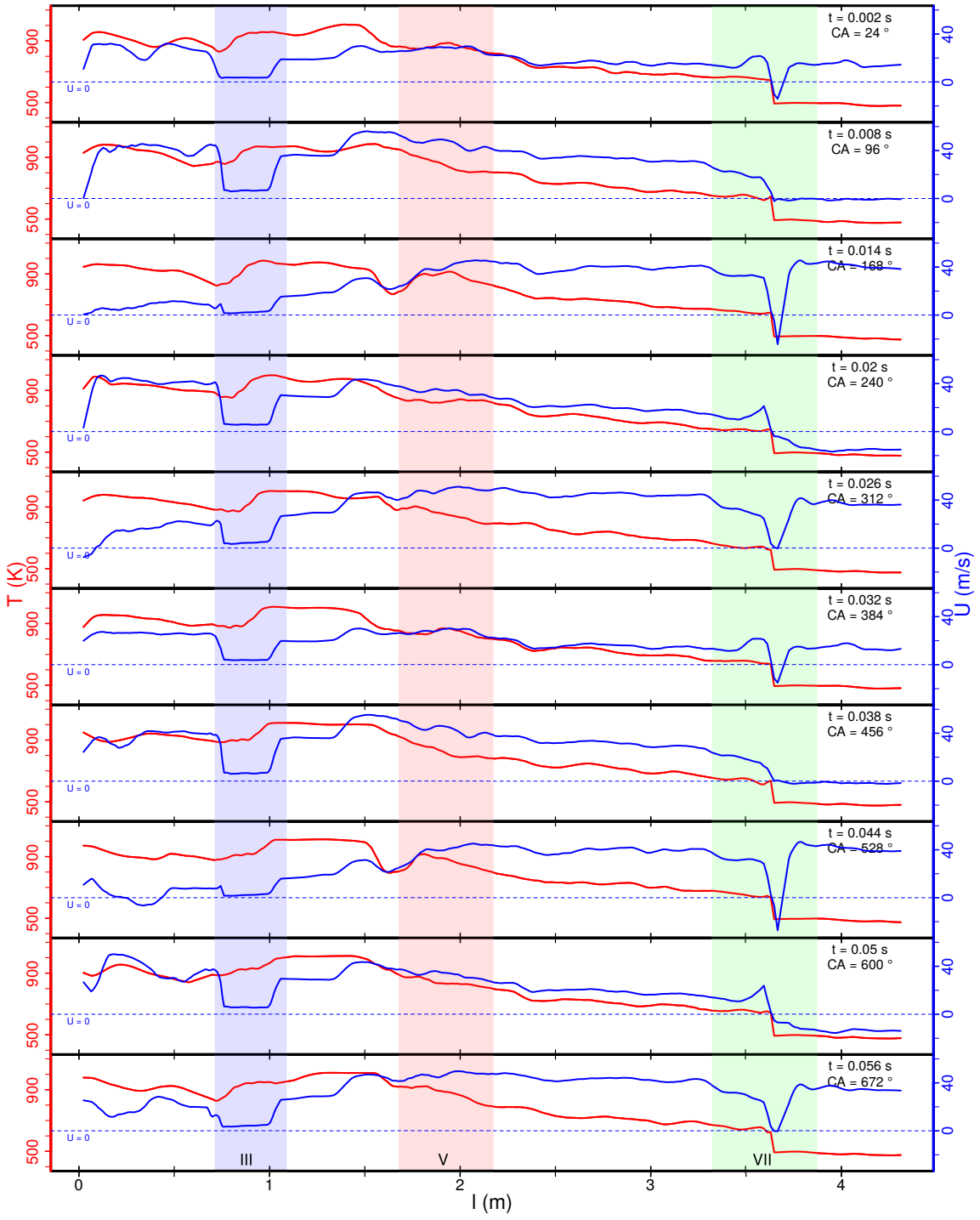

Figure A.4: Phase-averaged mean velocity U and mean temperature T along centre line of the EGAS of a Lada Niva 21214. Blue shaded area (III) represents the section of the catalytic converter, red shaded area (V) the section of the front muffler and green shaded area (VII) principal muffler.

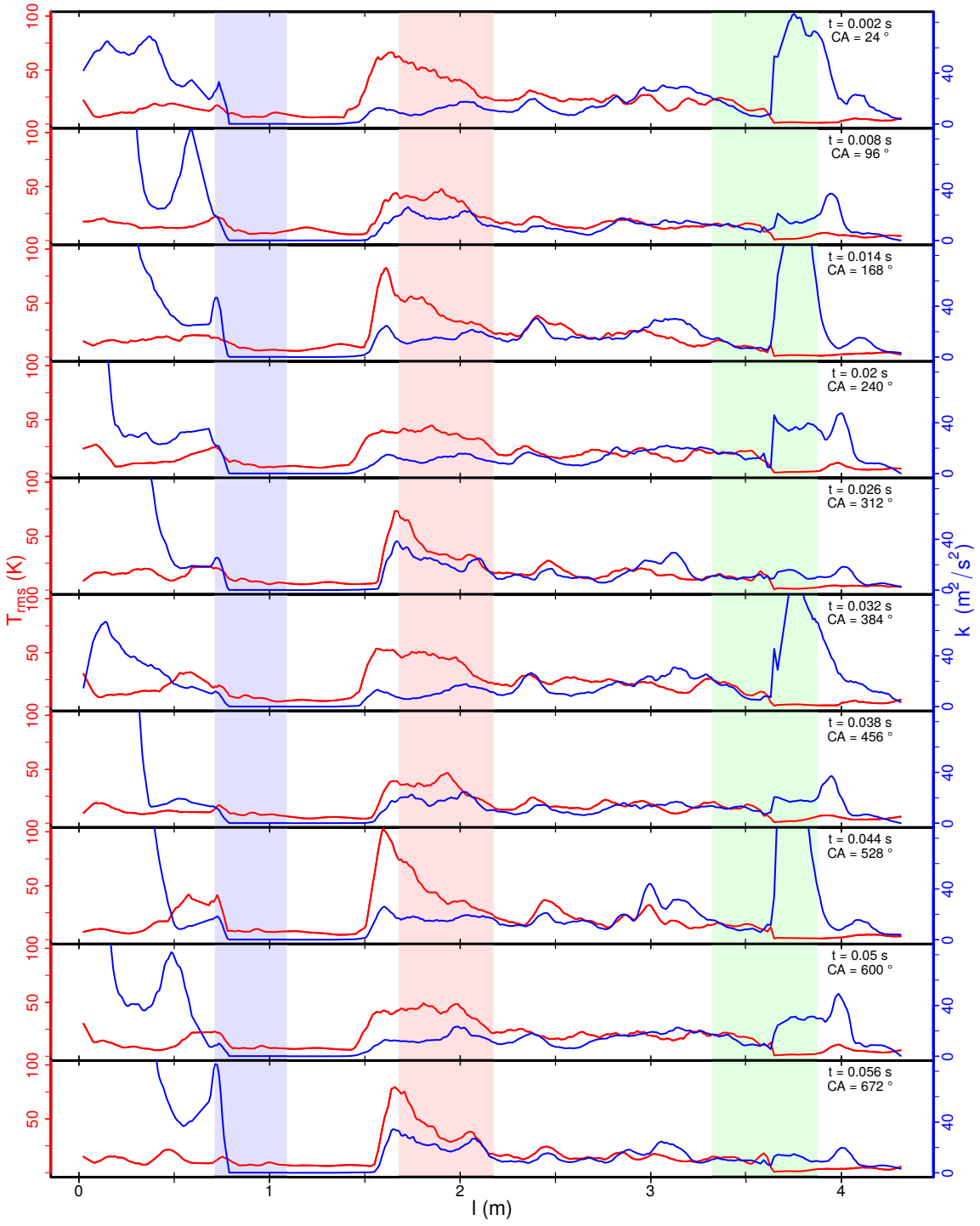

Figure A.5: Phase-averaged turbulent kinetic energy and rms temperature T along the centre line of the EGAS of a Lada Niva 21214. Shaded areas (III), (V), (VII) as described in Fig. A.4.

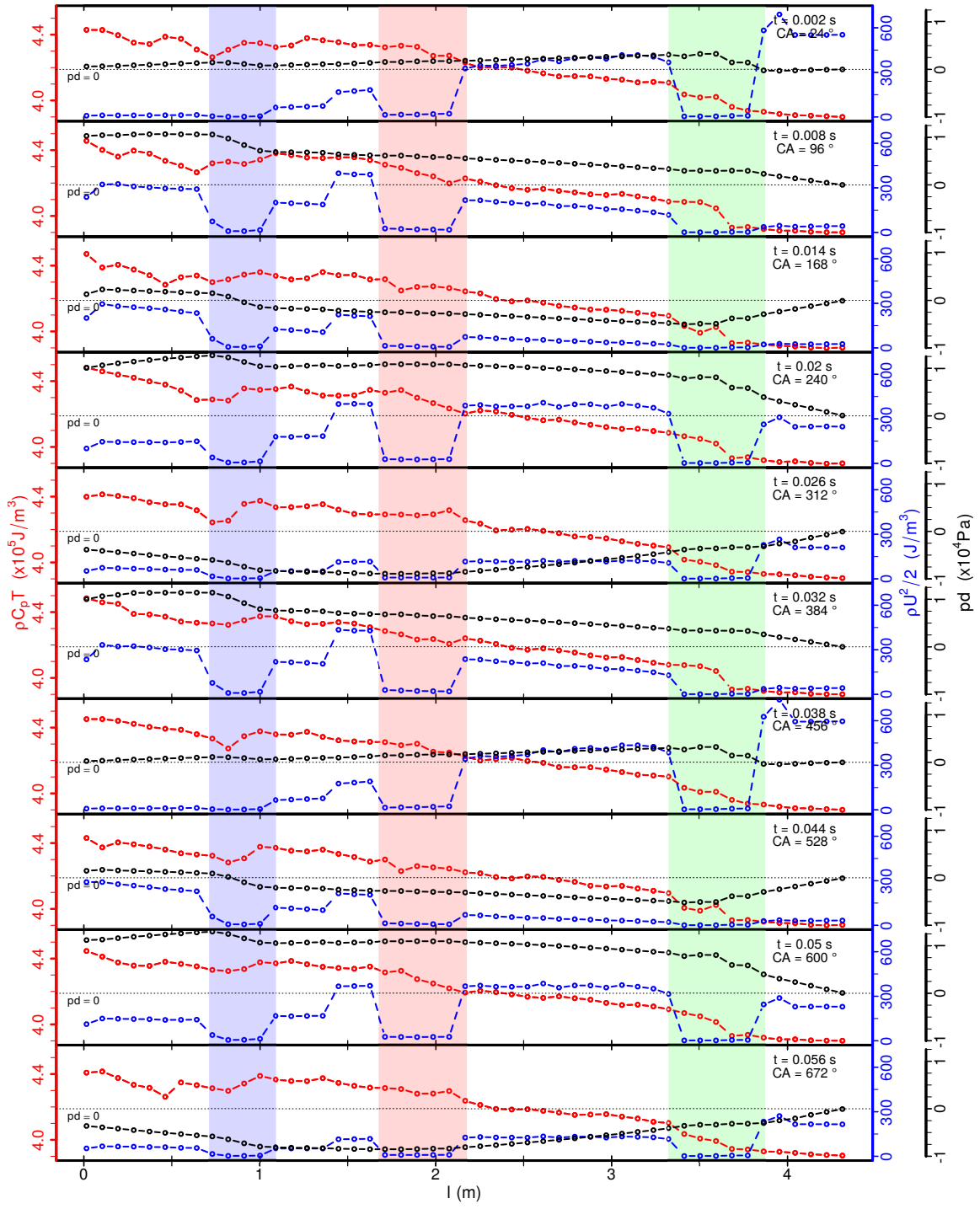

Figure A.6: Phase-averaged bulk thermal energy, kinetic energy and mechanical pressure along of the EGAS of a Lada Niva 21214. Shaded areas (III), (V), (VII) as described in Fig. A.4.

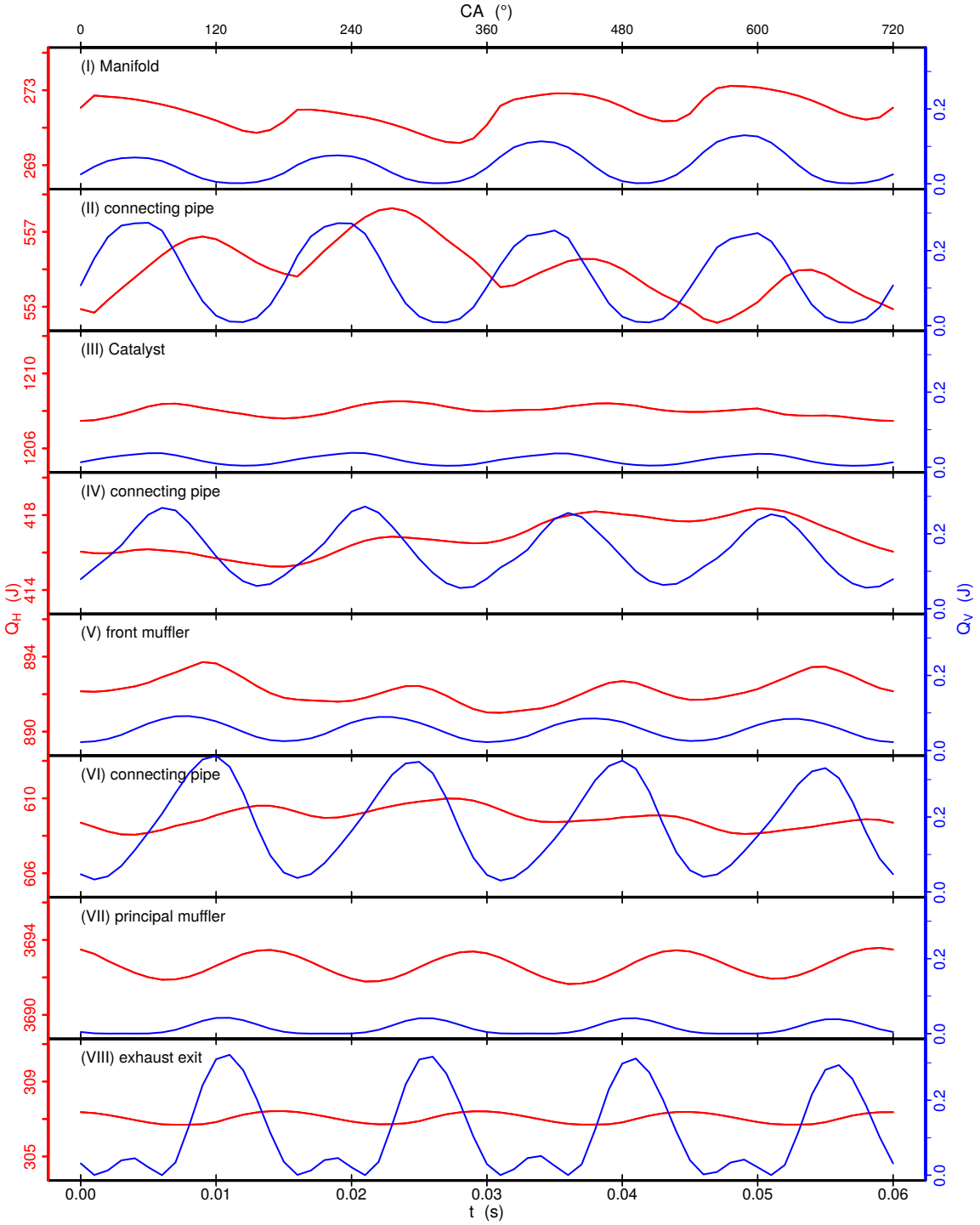

Figure A.7: Time series of thermal and total kinetic energy within a EGAS of a Lada Niva 21214.

Bibliography

[1] *VAZ Lada Niva Werkstatthandbuch (in German, information of copyrights in Russian).*

[2] H. Abe and H. Kawamura. A study of turbulence thermal structure in a channel flow through DNS up to Re_τ=640 with Pr=0.025 and 0.71. In *Proc. 9th Eur. Turbul. Conf.*, pages 399–402, 2002.

[3] H. Abe, H. Kawamura, and Y. Matsuo. Surface heat-flux fluctuations in a turbulent channel flow up to $Re_\tau = 1020$ with $Pr = 0.025$ and 0.71. *Int. J. Heat Fluid Fl.*, 25(3):404–419, 2004.

[4] A. K. Alekseev and I. M. Navon. On estimation of temperature uncertainty using the second order adjoint problem. In *Int. J. Comut. Fluid Dyn.*, volume 16, pages 113–117, jan 2002.

[5] D. E. Aljure, J. Calafell, A. Baez, and A. Oliva. Flow over a realistic car model: Wall modeled large eddy simulations assessment and unsteady effects. *J. Wind Eng. Ind. Aerod.*, 174:225–240, 2018.

[6] J. Altenbach and H. Altenbach. *Einführung in die Kontinuumsmechanik*. Teubner, 1994.

[7] J. S. an A. Nuri. *Strömungslehre: Einfürung in die Theorie der Strömungen*. Springer-Verlag Berlin Heidelberg New York, 2010.

[8] F. Avallone, D. Casalino, and D. Ragni. On the Effect of the Tip Clearance on the Aerodynamic and Aeroacoustics of a Diffuser-Augmented Wind Turbine. *AIAA Scitech*, pages AIAA 2019–1294, 2019.

[9] C. Bae and J. Kim. Alternative fuels for internal combustion engines. *Proceedings of the Combustion Institute*, 36(3):3389–3413, 2017.

[10] J. H. Bae, J. Y. Yoo, H. Choi, and D. M. McEligot. Effects of large density variation on strongly heated internal air flows. *Phys. Fluids*, 18:75102, 2006.

[11] H. D. Baehr and K. Stephan. *W arme- und Stoff ubertragung*. Springer Vieweg, Berlin, Heidelberg, 2013.

[12] J. S. Baggett. On the feasibility of merging les with rans for the near-wall region of attached turbulent flows. *Annual Research Briefs*, 1999.

[13] J. S. Baggett, J. Jimenez, and A. G. Kravchenko. Resolution requirements in large-eddy simulations of shear flows. *Annu. Res. briefs*, pages 51–66, 1997.

[14] E. Balaras, C. Benocci, and U. Piomelli. Two-layer approximate boundary conditions for large-eddy simulations. *AIAA J.*, 34(6):1111–1119, 1996.

[15] G. Batchelor. *An Introduction to Fluid Mechanics*. Camebridge University Press, 1967.

[16] G. K. Batchelor. Small-scale variation of convected quantities like temperature in turbulent fluid. Part 1. General discussion and the case of small conductivity. *J. Fluid Mech.*, 5:113–133, 1959.

[17] P. Böckh and T. Wetzel. *Wärmeübertragung: Grundlagen und Praxis*. Springer-Verlag, 2018.

[18] S. T. Bose and G. I. Park. Wall-Modeled Large-Eddy Simulation for Complex Turbulent Flows. *Annu. Rev. Fluid Mech.*, 50(1):535–561, jan 2018.

[19] A. Burcat and B. Ruscic. Third millennium ideal gas and condensed phase thermochemical database for combustion with updates from active thermochemical tables. Technical report, Report No. TAE 960, 2005.

[20] C. Y. Chang, S. Jakirlić, K. Dietrich, B. Basara, and C. Tropea. Swirling flow in a tube with variably-shaped outlet orifices: An LES and VLES study. *Int. J. Heat Fluid Flow*, 49(C):28–42, oct 2014.

[21] B. Chaouat. The State of the Art of Hybrid RANS/LES Modeling for the Simulation of Turbulent Flows, sep 2017.

[22] D. Chatterjee, O. Deutschmann, and J. Warnatz. Detailed surface reaction mechanism in a three-way catalyst. *Faraday Discuss.*, 119(1):371–384, nov 2001.

[23] K. A. Chauhan, P. A. Monkewitz, and H. M. Nagib. Criteria for assessing experiments in zero pressure gradient boundary layers. *Fluid Dyn. Res.*, 41:21404, 2009.

[24] K. Chida and K. Yoshiro. Conjugate heat transfer of continuously moving surfaces. *Int. J. Heat Mass Transf.*, 19(5):461–470, may 1976.

[25] W. K. Chiu, C. J. Richards, and Y. Jaluria. Experimental and numerical study of conjugate heat transfer in a horizontal channel heated from below. *J. Heat Transfer*, 123(4):688–697, aug 2001.

[26] I. Chorkendorff and J. W. Niemantsverdriet. *Concepts of Modern Catalysis and Kinetics*. Wiley, oct 2003.

[27] C. Cintolesi, A. Petronio, and V. Armenio. Large eddy simulation of turbulent buoyant flow in a confined cavity with conjugate heat transfer. *Phys. Fluids*, 27(9):095109, sep 2015.

[28] I. Cornejo. A model for correcting the pressure drop between two monoliths. *Catalysts*, 11(11), 2021.

[29] I. Cornejo, P. Nikrityuk, and R. E. Hayes. The influence of channel geometry on the pressure drop in automotive catalytic converters: Model development and validation. *Chem. Eng. Sci.*, 212:115317, feb 2020.

[30] S. Corrsin. On the Spectrum of Isotropic Temperature Fluctuations in an Isotropic Turbulence. *J. Appl. Phys.*, 22:469–473, 1951.

[31] R. Courant, K. Friedrichs, and H. Lewy. Über die partiellen Differenzengleichungen der mathematischen Physik. *Math. Ann.*, 100(1):32–74, 1928.

[32] T. J. Craft, S. E. Gant, A. V. Gerasimov, H. Iacovides, and B. E. Launder. Development and application of wall-function treatments for turbulent forced and mixed convection flows. *Fluid Dyn. Res.*, 38:127–144, 2006.

[33] T. J. Craft, A. V. Gerasimov, H. Iacovides, and B. E. Launder. Progress in the generalization of wall-function treatments. *Int. J. Heat Fluid Fl.*, 23:148–160, 2002.

[34] G. Croce. A Conjugate Heat Transfer Procedure for Gas Turbine Blades. *Ann. N. Y. Acad. Sci.*, 934(1):273–280, 2006.

[35] B. J. Daly and F. H. Harlow. Transport equations in turbulence. *Phys. Fluids*, 13:2634–2649, 1970.

[36] J. W. Deardorff. A numerical study of three-dimensional turbulent channel flow at large Reynolds numbers. *J. Fluid Mech.*, 41:453–480, 1970.

[37] R. G. Deissler. Investigation of turbulent flow and heat transfer in smooth tube, including the effects of variable fluid properties. *Trans. ASME*, 73(2):101–107, 1951.

[38] R. G. Deissler. Analysis of turbulent heat transfer, mass transfer, and friction in smooth tubes at high Prandtl and Schmidt numbers. Technical Report NASA-10-005594, NASA Lewis Flight Propulsion Lab., Cleveland, USA, 1955.

[39] A. Demirbas. Future fuels for internal combustion engines. *Energy Sources, Part A: Recovery, Utilization, and Environmental Effects*, 32(14):1273–1281, 2010.

[40] I. Demirdžić and S. Muzaferija. Numerical method for coupled fluid flow, heat transfer and stress analysis using unstructured moving meshes with cells of arbitrary topology. *Comput. Methods Appl. Mech. Eng.*, 125(1-4):235–255, 1995.

[41] O. Deutschmann and J. D. Grunwaldt. Abgasnachbehandlung in mobilen Systemen: Stand der Technik, Herausforderungen und Perspektiven. *Chemie-Ingenieur-Technik*, 85(5):595–617, 2013.

[42] A. Dorfman and Z. Renner. Conjugate problems in convective heat transfer: Review, 2009.

[43] A. S. Dorfman. Heat transfer from liquid to liquid in a flow past two sides of a plate. *High Temp.*, 8:515–520, 1970.

[44] A. S. Dorfman. Heat Transfer in Flow around Nonisothermal Bodies. *Mashinostroenie, Moscow, Russ.*, 1982.

[45] A. S. Dorfman and B. V. Davydenko. Conjugate heat transfer in flow over elliptical cylinders. *High Temp.*, 10(2):334–340, 1980.

[46] H. L. Dryden. Recent Advances in the Mechanics of Boundary Layer Flow. *Adv. Appl. Mech.*, 1:1–40, 1948.

[47] F. Duchaine, N. Maheu, V. Moureau, G. Balarac, and S. Moreau. Large-Eddy Simulation and Conjugate Heat Transfer Around a Low-Mach Turbine Blade. *J. Turbomach.*, 136(5), 2014.

[48] M. Durat, Z. Parlak, M. Kapsiz, A. Parlak, and ve Ferit FIÇICI. CFD AND EXPERIMENTAL ANALYSIS ON THERMAL PERFORMANCE OF EXHAUST SYSTEM OF A SPARK IGNITION ENGINE. *J. Therm. Sci. Technol.*, 33:89–99, 2013.

[49] T. Dzanic and J. C. Oefelein. Non-equilibrium wall modeling for large eddy simulation of stalled iced airfoils. In *AIAA Scitech 2020 Forum, 6-10 Jan. 2020, Orlando, FL, USA*, pages AIAA 2020–1076, 2020.

[50] B. W. Faßmann, J. W. Delfs, and R. Ewert. Derivation of volume averaged perturbation equations for aeroacoustics in porous materials. *SFB 880-Fundamentals of high-lift for future commercial aircraft, Biennial Report*, 2015.

[51] P. Fernández-Yáñez, O. Armas, A. Gómez, and A. Gil. Developing computational fluid dynamics (CFD) models to evaluate available energy in exhaust systems of diesel light-duty vehicles. *Appl. Sci.*, 7(6), 2017.

[52] C. Flageul, S. Benhamadouche, É. Lamballais, and D. Laurence. DNS of turbulent channel flow with conjugate heat transfer: Effect of thermal boundary conditions on the second moments and budgets. *Int. J. Heat Fluid Flow*, 55:34–44, 2015.

[53] C. Flageul, I. Tiselj, S. Benhamadouche, and M. Ferrand. A Correlation for the Discontinuity of the Temperature Variance Dissipation Rate at the Fluid-Solid Interface in Turbulent Channel Flows. *Flow, Turbul. Combust.*, 103(1):175–201, 2019.

[54] F. Fortunato, M. Caprio, P. D. Oliva Elasis SCpA Giovanni, P. Pantaleone, A. Andreozzi, O. Manca, P. Oliva, G. D'Aniello, P. Pantaleone, A. Andreozzi, and O. Manca. Numerical and Experimental Investigation of the Thermal Behavior of a Complete Exhaust System, apr 2007.

[55] H. Fu, X. Chen, I. Shilling, and S. Richardson. A one-dimensional model for heat transfer in engine exhaust systems. In *SAE Tech. Pap.*, apr 2005.

[56] M. Germano. A dynamic subgrid-scale eddy viscosity model. *Phys. Fluids*, 3(7):1760–1765, 1991.

[57] C. Geuzaine and J.-F. Remacle. Gmsh: A 3-d finite element mesh generator with built-in pre- and post-processing facilities. *International Journal for Numerical Methods in Engineering*, 79:1309–1331, 9 2009.

[58] E. Goncalves and R. Houdeville. Reassessment of the wall functions approach for RANS computations. *Aerosp. Sci. Technol.*, 5:1–14, 2001.

[59] O. A. Grechannyy, A. S. Dorfman, and V. G. Gorobets. Efficiency and conjugate heat transfer of finned flat surfaces. *High Temp.*, 11(5):900–906, 1986.

[60] C. J. Greenshields. OpenFOAM Programmer's Guide Version 3.0.1.

[61] M. S. Gritskevich, A. V. Garbaruk, J. Schütze, and F. R. Menter. Development of DDES and IDDES formulations for the k-ω shear stress transport model. *Flow, Turbul. Combust.*, 88(3):431–449, apr 2012.

[62] C. Hasse. Scale-resolving simulations in engine combustion process design based on a systematic approach for model development. *Int. J. Engine Res.*, 17(1):44–62, jan 2016.

[63] M. Haussmann, F. Ries, J. B. Jeppener-Haltenhoff, Y. Li, M. Schmidt, C. Welch, L. Illmann, B. Böhm, H. Nirschl, M. J. Krause, and A. Sadiki. Evaluation of a Near-Wall-Modeled Large Eddy Lattice Boltzmann Method for the Analysis of Complex Flows Relevant to IC Engines. *Computation*, 8(2):43, 2020.

[64] R. E. Hayes, A. Fadic, J. Mmbaga, and A. Najafi. Cfd modelling of the automotive catalytic converter. *Catal. Today*, 188(1):94–105, jul 2012.

[65] M. He, A. J. Kassab, P. J. Bishop, and A. Minardi. An iterative FDM/BEM method for the conjugate heat transfer problem - parallel plate channel with constant outside temperature. *Eng. Anal. Bound. Elem.*, 15(1):43–50, jan 1995.

[66] J. B. Heywood. Internal combustion engine fundamentals, second edition. *Internal Combustion Engine Fundamentals Second Edition*, 2018.

[67] C. Hirsch. *Numerical Computation of Internal & External Flows: Fundamentals of Computational Fluid Dynamics*. John Wiley & Sons, 2 edition, 2007.

[68] M. Hradisky and T. Hauser. Evaluating LES subgrid-scale models for high flux flows. In *Proc. ASME-JSME Therm. Eng. Summer Heat Transf. Conf. 6-13 July 2007, Vancouver, Canada*, 2007.

[69] Y. Huai. *Large eddy simulation in the scalar field*. PhD thesis, Technische Universität Darmstadt, 2006.

[70] K. Hutter. *Fluid- und Thermodynamik*. Springer-Verlag Berlin Heidelberg New York, 2 edition, 2003.

[71] R. I. Issa. Solution of the implicitly discretised fluid flow equations by operator-splitting. *J. Comput. Phys.*, 62:40–65, 1985.

[72] S. Jahangeer, M. K. Ramis, and G. Jilani. Conjugate heat transfer analysis of a heat generating vertical plate. *Int. J. Heat Mass Tran.*, 50(1):85–93, 2007.

[73] H. Jasak. *Error Analysis and Estimation for the Finite Volume Method with Applications to Fluid Flows*. PhD thesis, Imperial College of Science, Technology and Medicine, University of London, 1996.

[74] C. Jayatilleke. *The influence of Prandtl number and surface roughness on the resistance of the laminar sub-layer to momentum and heat transfer*. PhD thesis, Imperial College of Science, Technology and Medicine, London, UK, 1969.

[75] M. Jischa and H. B. Rieke. About the prediction of turbulent Prandtl and Schmidt numbers from modeled transport equations. *Int. J. Heat Mass Transf.*, 22:1547–1555, 1979.

[76] D. Jou, J. Casas-Vázquez, and G. Lebon. *Extended irreversible thermodynamics*. Springer-Verlag Berlin Heidelberg New York, 2 edition, 1996.

[77] B. A. Kader. Temperature and concentration profiles in fully turbulent boundary layers. *Int. J. Heat Mass Tran.*, 24(9):1541–1544, 1981.

[78] K. Kanai and H. Katsuyama. The Predictive Simulation of Exhaust Pipe Narrow-band Noise. *SAE Int. J. Passeng. Cars - Mech. Syst.*, 8(1):82–91, 2015.

[79] I. P. Kandylas and A. M. Stamatelos. Engine exhaust system design based on heat transfer computation. *Energy Convers. Manag.*, 40(10):1057–1072, jul 1999.

[80] D. J. Kapparos, D. E. Foster, and C. J. Rutland. Sensitivity analysis of a diesel exhaust system thermal model. In *SAE Tech. Pap.*, mar 2004.

[81] R. Karvinen. Transient conjugated heat transfer to laminar flow in a tube or channel. *Int. J. Heat Mass Transf.*, 31(6):1326–1328, jun 1988.

[82] A. Kassab, E. Divo, J. Heidmann, E. Steinthorsson, and F. Rodriguez. BEM/FVM conjugate heat transfer analysis of a three-dimensional film cooled turbine blade. *Int. J. Numer. Methods Heat Fluid Flow*, 13(5-6):581–610, 2003.

[83] S. Kawai. Direct numerical simulation of transcritical turbulent boundary layers at supercritical pressures with strong real fluid effects. In *Proc. 54^{t}h AIAA Aerosp. Sci. Meet. San Diego (CA), USA; 4-8 January 2016, Am. Inst. Aeronaut. Astronaut.*, 2016.

[84] S. Kawai and J. Larsson. Dynamic non-equilibrium wall-modeling for large eddy simulation at high Reynolds numbers. *Phys. Fluids*, 25(1):015105, jan 2013.

[85] H. Kawamura, H. Abe, and Y. Matsuo. DNS of turbulent heat transfer in channel flow with respect to Reynolds and Prandtl number effects. *Int. J. Heat Fluid Fl.*, 20(3):196–207, 1999.

[86] A. Keating and U. Piomelli. A dynamic stochastic forcing method as a wall-layer model for large-eddy simulation. *J. Turbul.*, 7:1–24, jan 2006.

[87] A. Keating, U. Piomelli, K. Bremhorst, and S. Nesic. Large-eddy simulation of heat transfer downstream of a backward-facing step. *J. Turbul.*, pages 1468–5248, 2004.

[88] M. Klein. *Towards LES as an engineering tool.* habilitation, Technische Universität Darmstadt, 2008.

[89] M. Klein, A. Sadiki, and J. Janicka. A digital filter based generation of inflow data for spatially developing direct numerical or large eddy simulations. *J. Comput. Phys.*, 186:652–665, 2003.

[90] W. Kollmann. *Fluid Mechanics in Spatial and Material Description.* University Readers, 1 edition, 2010.

[91] A. Kolmogorov. Dissipation of energy in locally isotropic turbulence. *Dokl. Akad. Nauk SSSR*, 32:16, 1941.

[92] A. Kolmogorov. The local structure of turbulence in incompressible viscous fluid for very large Reynolds' numbers. *Dokl. Akad. Nauk SSSR*, 30:301–305, 1941.

[93] P. A. Konstantinidis, G. C. Koltsakis, and A. M. Stamatelos. Transient heat transfer modelling in automotive exhaust systems. *Proceedings of the Institution of Mechanical Engineers, Part C: Journal of Mechanical Engineering Science*, 211:1–15, 1 1997.

[94] T. Krüger, H. Kusumaatmaja, A. Kuzmin, O. Shardt, G. Silva, and E. M. Viggen. *The Lattice Boltzmann Method.* Springer, Cham, 2017.

[95] B. Krumbein, S. Jakirlić, and C. Tropea. VLES study of a jet impinging onto a heated wall. *Int. J. Heat Fluid Flow*, 68:290–297, dec 2017.

[96] C. R. KUMAR, A. Sonthalia, and R. Goel. Experimental study on waste heat recovery from an internal combustion engine using thermoelectric technology. *Therm. Sci.*, 15(4):1011–1022, 2011.

[97] O. Labbé, P. Sagaut, and E. Montreuil. Large-eddy simulation of heat transfer over a backward-facing step. *Numer. Heat Transf. Part A*, 42:73–90, 2002.

[98] S. N. Lane, K. F. Bradbrook, K. S. Richards, P. A. Biron, and A. G. Roy. The application of computational fluid dynamics to natural river channels: three-dimensional versus two-dimensional approaches. *Geomorphology*, 29:1–20, 1999.

[99] J. Larsson, S. Kawai, J. Bodart, and I. Bermejo-Moreno. Large eddy simulation with modeled wall-stress: recent progress and future directions. *Mech. Eng. Rev.*, 3(1):15–418, 2016.

[100] J. Laufer. The structure of turbulence in fully developed pipe flow. Technical Report NACA Report TN 2954, National Advisory Committee for Aeronautics., Washington, USA, 1953.

[101] B. E. Launder and B. I. Sharma. Application of the energy-dissipation model of turbulence to the calculation of Flow near a spinning disc. *Lett. Heat Mass Trans.*, 1(2):131–138, 1974.

[102] K. T. Lee and W. M. Yan. Transient conjugated forced convection heat transfer with fully developed laminar flow in pipes. *Numer. Heat Transf. Part A Appl.*, 23(3):341–359, apr 1993.

[103] Y. Li, L. F. R. Cortes, H. Hamel, K. Nishad, L. Biondo, and F. Ries. Prediction of heat transfer and fluid flow effects on entropy generation in a monolithic catalytic converter using large-eddy simulation. *Entropy*, 24(5), 2022.

[104] Y. Li, F. Ries, W. Leudesdorff, K. Nishad, A. Pati, C. Hasse, J. Janicka, S. Jakirlic, and A. Sadiki. Non-equilibrium wall functions for large eddy simulations of complex turbulent flows and heat transfer. *Int. J. Heat Fluid Fl.*, 88:108758, 2021.

[105] Y. Li, F. Ries, K. Nishad, and A. Sadiki. Predictions of conjugate heat transfer in turbulent channel flow using advanced wall-modeled large eddy simulation techniques. *Entropy*, 23(6), 2021.

[106] F. N. K. Li Y.; Ries and A. Sadiki. Near-wall modeling of LES for non-equilibrium turbulent flows in an inclined impinging jet with moderate Re-number. In *Proc. 6th Eur. Conf. Comput. Mech. (ECCM 6), 11-15 June 2018, Glas. UK*, 2018.

[107] A. Liakopoulos. Explicit representation of the complete velocity profile in a turbulent boundary layer. *AIAA J.*, 22:844–846, 1983.

[108] D. K. Lilly. A proposed modification of the Germano subgrid-scale closure method. *Phys. Fluids*, 4(3):633–635, 1992.

[109] T. F. Lin and J. C. Kuo. Transient conjugated heat transfer in fully developed laminar pipe flows. *Int. J. Heat Mass Transf.*, 31(5):1093–1102, may 1988.

[110] M. S. Lota, V. Ravindran, P. Rao V., and R. Verma. FEA approach for calculating back pressure in automotive muffler. *SAE Tech. Pap.*, 5:1–8, 2013.

[111] M. R. Malin. On the calculation of heat transfer rates in fully turbulent wall flows. *Appl. Math. Model*, 11(4):281–284, 1987.

[112] J. Martins and F. P. Brito. Alternative fuels for internal combustion engines. *Energies*, 13(16):4086, 2020.

[113] G. T. Mase and G. E. Mase. *Continuum mechanics for engineers*. CRC Press LLC, 2 edition, 1999.

[114] L. Meda, Y. Shu, and M. Romzek. Exhaust system manifold development. *SAE Tech. Pap.*, 2012.

[115] S. Menon, P.-K. Yeung, and W.-W. Kim. Effect of subgrid models on the computed interscale energy transfer in isotropic turbulence. *Comput. Fluids*, 25:165–180, 1996.

[116] F. R. Menter, M. Kuntz, and R. Bender. A scale-adaptive simulation model for turbulent flow predictions. In *41st Aerosp. Sci. Meet. Exhib.*, Reston, Virigina, jan 2003. American Institute of Aeronautics and Astronautics.

[117] M. Mittal, R. Donahue, and P. Winnie. Evaluating the Influence of Exhaust Back Pressure on Performance and Exhaust Emissions Characteristics of a Multicylinder, Turbocharged, and Aftercooled Diesel Engine. *J. Energy Resour. Technol.*, 137(3), may 2015.

[118] A. K. M. Mohiuddin, M. R. Ideres, and S. M. Hashim. Experimental Study of Noise and Back Pressure for Silencer Design Characteristics. *J. Appl. Sci.*, 5(7):1292–1298, 2005.

[119] P. Moin, K. Squires, W. Cabot, and S. Lee. A dynamic subgrid-scale model for compressible turbulence and scalar transport. *Phys. Fluids*, 3:2746–2757, 1991.

[120] I. Müller. *Thermodynamik: Die Grundlagen der Materialtheorie.* Bertelsmann Universitätsverlag, 1 edition, 1972.

[121] A. J. Musker. Explicit expression for the smooth wall velocity distribution in a turbulent boundary layer. *AIAA J.*, 17(6):655–657, 1979.

[122] F. Nasuti, A. Torricelli, and S. Pirozzoli. Conjugate heat transfer analysis of rectangular cooling channels using modeled and direct numerical simulation of turbulence. *Int. J. Heat Mass Transf.*, 181:121849, dec 2021.

[123] F. Nicoud and F. Ducros. Subgrid-scale stress modelling based on the square of the velocity gradient tensor. *Flow Turbul. Combust.*, 62:183–200, 1999.

[124] F. Nicoud, H. B. Toda, O. Cabrit, S. Bose, and J. Lee. Using singular values to build a subrid-scale model for large eddy simulations. *Phys. Fluids*, 23:85106, 2011.

[125] B. E. Nieuwenhuys. The surface science approach toward understanding automotive exhaust conversion catalysis at the atomic level. In W. O. Haag, B. C. Gates, and H. Knözinger, editors, *Advances in Catalysis*, volume 44, pages 259–328. Elsevier, 1999.

[126] N. V. Nikitin, F. Nicoud, B. Wasistho, K. D. Squires, and P. R. Spalart. An approach to wall modeling in large-eddy simulations. *Phys. Fluids*, 12(7):1629–1632, jul 2000.

[127] K. Nishad, F. Ries, J. Janicka, and A. Sadiki. Analysis of spray dynamics of urea–water-solution jets in a SCR-DeNOx system: An LES based study. *Int. J. Heat Fluid Flow*, 70:247–258, apr 2018.

[128] K. Nishad, F. Ries, Y. Li, and A. Sadiki. Numerical investigation of flow through a valve during charge intake in a DISI -engine using large eddy simulation. *Energies*, 12(13):2620, jul 2019.

[129] A. M. Obukhov. Structure of the temperature field in turbulent flow. Technical report, DTIC Document, 1968.

[130] S. H. Oh and J. C. Cavendish. Transients of Monolithic Catalytic Converters: Response to Step Changes in Feedstream Temperature as Related to Controlling Automobile Emissions. *Ind. Eng. Chem. Prod. Res. Dev.*, 21(1):29–37, mar 1982.

[131] K. C. Ong and A. Chan. A unified wall function for compressible turbulence modelling. *J. Turbul.*, 19:414–430, 2018.

[132] G. I. Park and P. Moin. An improved dynamic non-equilibrium wall-model for large eddy simulation. *Phys. Fluids*, 26(1):015108, jan 2014.

[133] S. Patankar and D. Spalding. A calculation procedure for heat, mass and momentum transfer in three-dimensional parabolic flows. *Int. J. Heat Mass Tran.*, 15:1787–1806, 1972.

[134] S. V. Patankar. *Numerical heat transfer and fluid flow.* Hemisphere Publishing Corporation, 1 edition, 1980.

[135] S. H. Peng and L. Davidson. On a subgrid-scale heat flux model for large eddy simulation of turbulent thermal flow. *Int. J. Heat Mass Tran.*, 45:1393–1405, 2002.

[136] U. Piomelli. High Reynolds number calculations using the dynamic subgrid-scale stress model. *Phys. Fluids A Fluid Dyn.*, 5(6):1484–1490, 1993.

[137] U. Piomelli. Wall-layer models for large-eddy simulations. *Prog. Aerosp. Sci.*, 44:437–446, 2008.

[138] U. Piomelli, E. Balaras, H. Pasinato, K. D. Squires, and P. R. Spalart. The inner–outer layer interface in large-eddy simulations with wall-layer models. *Int. J. Heat Fluid Flow*, 24(4):538–550, 2003.

[139] U. Piomelli, T. A. Zang, C. G. Speziale, and M. Y. Hussaini. On the large-eddy simulation of transitional wall-bounded flows. *Phys. Fluids A*, 2(2):257–265, feb 1990.

[140] H. Pong, J. Wallace, and P. E. Sullivan. Modeling of exhaust gas treatment for stationary applications. In *SAE Tech. Pap.* SAE International, 2012.

[141] S. B. Pope. Ten questions concerning the large-eddy simulation of turbulent flows. *New J. Phys.*, 6(35), 2004.

[142] S. B. Pope. *Turbulent Flows*. Cambridge University Press, 2009.

[143] M. Popovac and K. Hanjalić. Large-eddy simulations of flow over a jet-impinged wall-mounted cube in cross stream. *Int. J. Heat Fluid Flow*, 28:1360–1378, 2007.

[144] S. Radhakrishnan, A. Keating, U. Piomelli, and A. S. Lopes. Large-eddy simulations of high Reynolds-number flow over a contoured ramp. In *Collect. Tech. Pap. - 44th AIAA Aerosp. Sci. Meet.*, volume 14, pages 10743–10755. American Institute of Aeronautics and Astronautics Inc., 2006.

[145] C. P. Rahaim, A. J. Kassab, and R. J. Cavalleri. Coupled dual reciprocity boundary element/finite volume method for transient conjugate heat transfer. *J. Thermophys. heat Transf.*, 14(1):27–38, jan 2000.

[146] C. D. Rakopoulos, G. M. Kosmadakis, and E. G. Pariotis. Critical evaluation of current heat transfer models used in CFD in-cylinder engine simulations and establishment of a comprehensive wall-function formulation. *Appl. Energ.*, 87(5):1612–1630, 2010.

[147] H. Reichardt. Die Grundlagen des turbulent Wärmeüberganges. *Arch. Ges. Wärmetech*, 2:129–142, 1951.

[148] H. Reichardt. Vollständige Darstellung der turbulenten Geschwindigkeitsverteilung in glatten Leitungen. *IZ. angew. Math. Mech.*, 31(7):208–219, 1951.

[149] L. F. Richardson. *Weather Predictions by Numerical Process*. Cambridge University Press, 2 edition, 1922.

[150] F. Ries. *Numerical Modeling and Prediction of Irreversibilities in Sub- and Supercritical Near-Wall Flows*. PhD thesis, Institute of Energy and Power Plant Technology, Technische Universität Darmstadt, Darmstadt, Germany, 2018.

[151] F. Ries, Y. Li, D. Klingenberg, K. Nishad, J. Janicka, and A. Sadiki. Near-wall thermal processes in an inclined impinging jet: Analysis of heat transport and entropy generation mechanisms. *energies*, 11(6):1354, 2018.

[152] F. Ries, Y. Li, K. Nishad, L. Dressler, M. Ziefuss, A. Mehdizadeh, C. Hasse, and A. Sadiki. A Wall-Adapted Anisotropic Heat Flux Model for Large Eddy Simulations of Complex Turbulent Thermal Flows. *Flow, Turbul. Combust.*, 106(2):733–752, feb 2021.

[153] F. Ries, Y. Li, K. Nishad, J. Janicka, and A. Sadiki. Entropy Generation Analysis and Thermodynamic Optimization of Jet Impingement Cooling Using Large Eddy Simulations. *Entropy*, 21:129, 2019.

[154] F. Ries, Y. Li, M. Rißmann, D. Klingenberg, K. Nishad, B. Böhm, A. Dreizler, J. Janicka, and A. Sadiki. Database of near-wall turbulent flow properties of a jet impinging on a solid surface under different inclination angles. *fluids*, 3(1):5, 2018.

[155] P. L. Roe. Characteristic-Based Schemes for the Euler Equations. *Annu. Rev. Fluid Mech.*, 18:337–365, 1987.

[156] P. Sagaut. *Large Eddy Simulation for incompressible Flows: An Introduction*. Springer-Verlag Berlin Heidelberg New York, 2006.

[157] M. Schäfer. *Computational Engineering - Introduction to Numerical Methods*. Springer-Verlag Berlin Heidelberg, 1 edition, 2006.

[158] H. Schlichting and K. Gersten. *Boundary-layer theory*. Springer, Berlin, Heidelberg, 2017.

[159] H. Schmidt and U. Schumann. Coherent structure of the convective boundary layer derived from large-eddy simulations. *J. Fluid Mech.*, 200:511–562, 1989.

[160] A. Scotti and U. Piomelli. Numerical simulation of pulsating turbulent channel flow. *Phys. Fluids*, 13:1367–1384, 2001.

[161] P. J. Shayler, D. J. Hayden, and T. Ma. Exhaust system heat transfer and catalytic converter performance. In *SAE Technical Paper 1999-01-0453*, 3 1999.

[162] A. M. Shehata and D. M. McEligot. Mean strucure in viscous layer of strongly-heated internal gas flows. Measurements. *Int. J. Heat Mass Tran.*, 41:4297–4313, 1998.

[163] T.-H. Shih, L. A. Povinelli, N.-S. Liu, M. G. Potapczuk, and J. L. Lumley. A generalized wall function. Technical Report NASA/TM-1999-209398, NASA Center for Aerospace Information, Hanover, MD, USA, 1999.

[164] M. L. Shur, P. R. Spalart, M. K. Strelets, and A. K. Travin. A hybrid RANS-LES approach with delayed-DES and wall-modelled LES capabilities. *Int. J. Heat Fluid Flow*, 29(6):1638–1649, dec 2008.

[165] J. Smagorinsky. General circulation experiments with primitive equations. *Mon. Weather Rev.*, 91(35):99–164, 1963.

[166] A. L. Snijders, A. M. Koppius, and C. Nieuwvelt. An experimental determination of the turbulent Prandtl number in the inner boundary layer for air flow over a flat plate. *Int. J. Heat Mass Transf.*, 26(3):425–431, 1983.

[167] M. Soliman and H. A. Johnson. Transient heat transfer for turbulent flow over a flat plate of appreciable thermal capacity and containing time-dependent heat source. *J. Heat Transfer*, 89(4):362–370, nov 1967.

[168] D. L. Sondak and D. J. Dorney. Simulation of coupled unsteady flow and heat conduction in turbine stage. *J. Propuls. Power*, 16(6):1141–1148, 2000.

[169] P. Spalart and S. Allmaras. A one-equation turbulence model for aerodynamic flows. In *30th Aerosp. Sci. Meet. Exhib.*, 1992.

[170] P. R. Spalart, S. Deck, M. L. Shur, K. D. Squires, M. K. Strelets, and A. Travin. A new version of detached-eddy simulation, resistant to ambiguous grid densities. *Theor. Comput. Fluid Dyn.*, 20(3):181–195, jul 2006.

[171] W. S. M. Spalart P.; Jou and S. Allmaras. Comments on the feasibility of LES for Wings, and on a hybrid RANS/LES approach. In *Proc. first AFOSR Int. Conf. DNS/LES. August 4–8, 1997, Ruston, Louisiana, USA*, 1997.

[172] D. B. Spalding. A Single Formula for the "Law of the Wall". *J. Appl. Mech.*, 28:455–458, 1961.

[173] C. G. Speziale. Turbulence modeling for time-dependent RANS and VLES: A review, feb 1998.

[174] J. H. Spurk and N. Aksel. *Fluid Mechanics*. Springer International Publishing, 2020.

[175] C. Srinivasan and D. V. Papavassiliou. Prediction of the Turbulent Prandtl Number in Wall Flows with Lagrangian Simulations. *Ind. Eng. Chem. Res.*, 50:8881–8891, 2011.

[176] H. Steiner, C. Irrenfried, and G. Brenn. Near-Wall Determination of the Turbulent Prandtl Number Based on Experiments, Numerical Simulation and Analytical Models. *Heat Transf. Eng.*, 41(15-16):1341–1353, 2020.

[177] J. Sucec. Unsteady conjugated forced convective heat transfer in a duct with convection from the ambient. *Int. J. Heat Mass Transf.*, 30(9):1963–1970, sep 1987.

[178] J. Sucec. Unsteady forced convection with sinusoidal duct wall generation: the conjugate heat transfer problem. *Int. J. Heat Mass Transf.*, 45(8):1631–1642, 2002.

[179] J. Sucec and A. M. Sawant. Unsteady, conjugated, forced convection heat transfer in a parallel plate duct. *Int. J. Heat Mass Transf.*, 27(1):95–101, jan 1984.

[180] K. Suga, T. Sakamoto, and Y. Kuwata. Algebraic non-equilibrium wall-stress modeling for large eddy simulation based on analytical integration of the thin boundary-layer equation. *Phys. Fluids*, 31:75109, 2019.

[181] W. Sutherland. The viscosity of gases and molecular force. *The London, Edinburgh, ans Dublin Philosophical Magazine and Journal of Science*, 36:507–531, 1893.

[182] L. Tan, P. Feng, S. Yang, Y. Guo, S. Liu, and Z. Li. CFD studies on effects of SCR mixers on the performance of urea conversion and mixing of the reducing agent. *Chem. Eng. Process. Process Intensif.*, 123:82–88, jan 2018.

[183] L. Temmerman, M. Hadziabdić, M. A. Leschziner, and K. Hanjalić. A hybrid two-layer URANS–LES approach for large eddy simulation at high Reynolds numbers. *Int. J. Heat Fluid Flow*, 26(2):173–190, 2005.

[184] F. Tessicini, L. Temmerman, and M. A. Leschziner. Approximate near-wall treatments based on zonal and hybrid RANS–LES methods for LES at high Reynolds numbers. *Int. J. Heat Fluid Flow*, 27(5):789–799, 2006.

[185] I. Tiselj and L. Cizelj. DNS of turbulent channel flow with conjugate heat transfer at Prandtl number 0.01. *Nucl. Eng. Des.*, 253:153–160, 2012.

[186] I. Tiselj, J. Oder, and L. Cizelj. Double-sided cooling of heated slab: Conjugate heat transfer DNS. *Int. J. Heat Mass Transf.*, 66:781–790, 2013.

[187] J. S. Travelho and W. F. Santos. Unsteady conjugate heat transfer in a circular duct with convection from the ambient and periodically varying inlet temperature. *J. Heat Transfer*, 120(2):506–510, may 1998.

[188] A. K. Travin, M. L. Shur, P. R. Spalart, and M. K. Strelets. IMPROVEMENT OF DELAYED DETACHED-EDDY SIMULATION FOR LES WITH WALL MODELLING. In *Eur. Conf. Comput. Fluid Dyn. ECCOMAS CFD*, 2006.

[189] J. C. Vogel and J. K. Eaton. Combined heat transfer and fluid dynamic measurements downstream of a backward-facing step. *J. Heat Trans.*, 107:922–929, 1985.

[190] S. E. Voltz, C. R. Morgan, D. Liederman, and S. M. Jacob. Kinetic Study of Carbon Monoxide and Propylene Oxidation on Platinum Catalysts. *Ind. Eng. Chem. Prod. Res. Dev.*, 12(4):294–301, dec 1973.

[191] T. von Kármán. The Analogy between Fluid Friction and Heat Transfer. *Trans. ASME*, 61:705–710, 1939.

[192] S. Wagh, S. Sen, G. Iyer, and S. Shukla. Development of exhaust silencer for improved sound quality and optimum back pressure. *SAE Tech. Pap.*, 2010.

[193] T. Wallner and S. A. Miers. Internal combustion engines, alternative fuels for. In R. A. Meyers, editor, *Encyclopedia of Sustainability Science and Technology*, pages 5461–5499. Springer New York, 2012.

[194] V. C. Wong and D. K. Lilly. A comparison of two dynamic subgrid closure methods for turbulent thermal convection. *Phys. Fluids*, 6:1016–1023, 1995.

[195] Z. Wu, D. Laurence, H. Iacovides, and I. Afgan. Direct simulation of conjugate heat transfer of jet in channel crossflow. *Int. J. Heat Mass Transf.*, 110:193–208, 2017.

[196] G. Xiao. Transient Simulation of Heat Transfers for Vehicle Exhaust System. In *Procedia Eng.*, volume 126, pages 410–415. Elsevier Ltd, 2015.

[197] G. Xiao, H. Wang, L. Chen, and X. Hong. Predicting unsteady heat transfer effect of vehicle thermal management system using steady velocity equivalent method. *Sci. Prog.*, 104(2):003685042110259, apr 2021.

[198] X. Xu, J. S. Lee, R. H. Pletcher, A. M. Shehata, and D. M. McEligot. Large eddy simulation of turbulent forced gas flows in vertical pipes with high heat transfer rates. *Int. J. Heat Mass Transf.*, 47:4113–4123, 2004.

[199] P. Yadav and P. Kothmire. Exhaust system of commercial vehicle: a review. *IOP Conf. Ser. Mater. Sci. Eng.*, 1116(1):012109, 2021.

[200] W. M. Yan. Transient conjugated heat transfer in channel flows with convection from the ambient. *Int. J. Heat Mass Transf.*, 36(5):1295–1301, jan 1993.

[201] W. M. Yan, Y. L. Tsay, and T. F. Lin. Transient conjugated heat transfer in laminar pipe flows. *Int. J. Heat Mass Transf.*, 32(4):775–777, apr 1989.

[202] Z.-F. Yao, Z.-J. Yang, and F.-J. Wang. Evaluation of near-wall solution approaches for large-eddy simulations of flow in a centrifugal pump impeller. *Eng. Appl. Comp. Fluid*, 10(1):452–465, 2016.

[203] A. Yoshizawa and K. Horiuti. A Statistically-Derived Subgrid-Scale Kinetic Energy Model for the Large-Eddy Simulation of Turbulent Flows. *J. Phys. Soc. Jpn.*, 54(8):2834–2839, 1985.

[204] D. You and P. Moin. A dynamic global-coefficient subgrid-scale model for large-eddy simulation of turbulent scalar transport in complex geometries. *Phys. Fluids*, 21:45109, 2009.

[205] B. A. Younis, C. G. Speziale, and T. T. Clark. A rational model for the turbulent scalar fluxes. *P. Roy. Soc. A-Math. Phy.*, 461:575–594, 2005.

[206] S. ZAHRAI, F. BARK, and R. KARLSSON. On anisotropic subgrid modeling. *Eur. J. Mech. B. Fluids*, 14(4):459–486, 1995.

[207] T. Zang. Numerical simulation of the dynamics of turbulent boundary layers: perspectives of a transition simulator. *Philos. Trans. R. Soc. London. Ser. A Phys. Eng. Sci.*, 336(1641):95–102, aug 1991.

[208] T. Zhang, H. Zhou, and S. Wang. An adjustment to the standard temperature wall function for CFD modeling of indoor convective heat transfer. *Build. Environ.*, 68:159–169, 2013.

[209] F. Zhao, K. Chen, H. Hao, and Z. Liu. Challenges, Potential and Opportunities for Internal Combustion Engines in China. *Sustainability*, 12(12):4955, jun 2020.

[210] C. Zheng, L. Xiao, R. Qu, S. Liu, Q. Xin, P. Ji, H. Song, W. Wu, and X. Gao. Numerical simulation of selective catalytic reduction of NO and SO2 oxidation in monolith catalyst. *Chem. Eng. J.*, 361:874–884, apr 2019.

[211] B. Zhong and P. G. Tucker. LES and hybrid LES/RANS simulations for conjugate heat transfer over a matrix of cubes. In *43rd AIAA Aerosp. Sci. Meet. Exhib. - Meet. Pap.*, pages 7207–7220, Reston, Virigina, jan 2005. American Institute of Aeronautics and Astronautics.

[212] M. Zöchbauer, H. Smith, and T. Lauer. Advanced SCR Flow Modeling with a Validated Large Eddy Simulation. *SAE Tech. Pap.*, 2015-April(April), 2015.